University of Naples Federico II


School of Polytechnic and Basic Sciences

PhD Thesis in “Industrial Product and Process Engineering”

Department of Chemical, Material and Industrial Production Engineering (DICMAPI)

# A Multi-Functional Strategy Based on Curcumin-Loaded Oil and Core-Starch Shell Tested in an Inflamed Gut-on-Chip with Microbiota

**Supervisor:** Prof. Paolo Antonio Netti **Coordinator:** Prof. Andrea D’anna

**Correlator:** Eng. Raffaele Vecchione

**PhD Candidate**

Raffaele Crispino

XXXVI PhD Cycle

Academic Year 2023/2024

# Index

# Abstract

The aim of this work is to find a suitable carrier treatment for the reduction of body weight and to treat obesity by developing at the same time a multifunctional carrier and a simple but effective gut on chip platform able to mimic healthy and inflamed tissue. To do so, we established which are the relevant causes that lead to obesity, starting from gut flora composition, and how it is currently treated, in terms of surgical operations and currently used carriers. We focused our attention on oil-in-water emulsions as oil has been shown to increase the feel of satiety. Moreover, oil allows the encapsulation of lipophilic molecules which usually have a poor bioavailability. Among them there are anti-inflammatory agents, like curcumin, which can reduce the inflammation state typical of obese subjects intestine. The proposed carrier is based on oil droplets coated with starch. The choice of the starch coating arises from its indigestibility in human gastrointestinal tract and it is only degraded by bacteria from gut flora. In this way, the carrier can reach the colon allowing a localized release. Indeed, among bacteria present in the colon, *Ruminococcus Bromii* is a keystone specie in degrading starch and it happens to be more present in obese subjects flora, playing a major role in energy homeostasis. Thus, by acting on their metabolism we can reduce energy harvesting and, in turn, reduce the intake of calories.

In summary, our carrier, due to starch indigestibility, will pass intact through the gastrointestinal tract till the colon, where *Ruminococcus Bromii* will degrade it, allowing the inner oil core to spread out and go towards the intestinal barrier, where the bacteria is attached to. Doing so a triple action can be achieved, briefly: 1) the bacteria, being entrapped in the oil, will be quenched but not killed preventing their metabolism and the calories intake associated with an overproduction of short chain fatty acids; 2) oil, going towards the intestinal barrier, will thicken it reducing the passage of nutrients and inducing a sense of satiety in the patient; 3) curcumin, loaded in the oil core, will be released exploiting its anti-inflammatory properties.

All the experiments are performed in an organ-on-chip platform which allows the growth of an intestinal layer which resembles the *in-vivo* one due to the presence of mucus and villi structures and which allows the growth of *Ruminococcus Bromii*, an anaerobic bacteria. The platform consists in two layers made of PDMS separated by a polycarbonate membrane. On top of the layer where cells and bacteria are cultured, an additional layer of glass is added to diminish the oxygen passage through the PDMS, allowing the co-culture of *Ruminococcus Bromii* and cells as demonstrated by simulations and viability assays.

# Abbreviations

| | |
|---|---|
| SCFAs | Short Chain Fatty Acids |
| GLP-1 | Glucagon-Like Peptide- 1 |
| CCK | Cholecystokinin |
| 16s rRNA | 16s ribosomal RNA |
| PCR | Polymerase Chain Reaction |
| FISH | Fluorescence In-Situ Hybridization |
| LPS | Lipopolysaccharides |
| FMT | Fecal Microbiota Transplantation |
| BMI | Body Mass Index |
| RS | Resistant Starch |
| *R. Bromii* | *Ruminococcus Bromii* |
| GIT | Gastrointestinal Tract |
| CIP | Ciprofloxacin hydrochloride |
| *S. Aureus* | *Staphylococcus Aureus* |
| MIC | Minimal Inhibitory Concentration |
| O/W | Oil-in-Water |
| Cur | Curcumin |
| TNF-α | Tumor Necrosis Factor-α |
| TEER | Transepithelial Electrical Resistance |
| *L. Rhamnosus* | *Lactobacillus Rhamnosus* |

| | |
|---|---|
| LVE | Linear Viscoelastic |
| SGF | Simulated Gastric Fluids |
| SIF | Simulated Intestinal Fluid |
| PBS | Phosphate Buffer Solution |
| SEM | Scanning Electron Microscopy |
| PMMA | Poly-(methyl methacrylate) |
| PDMS | Polydimethylsiloxane |
| ROS | Reactive Oxygen Species |
| MPs | Microparticles |
| Ct | Chitosan |
| NEs | Nanoemulsions |
| W/O | Water-in-Oil |
| SNEs | Secondary Nanoemulsions |
| PDI | Polydispersivity Index |
| SSF | Simulated Saliva Fluid |
| CoQ10 | Coenzyme Q10 |

# 1. State of art

## 1.1. Anatomy of the large intestine

### 1.1.1. Healthy

To understand how to mimic the intestinal environment *in-vitro* and how to analyze our outcomes, firstly, we have to take a look at what happens *in-vivo*.

The intestine is divided into two major regions: the small intestine and the large intestine. The small intestine starts with the duodenum. Duodenum is the shortest part of the small intestine and connects stomach to the intestine. Here, the breakdown of metabolites is still undergoing as there is the mix of the food digesta from the stomach with the enzymes from bile and pancreas. In this part, the pH is still low and bicarbonate is secreted as to increase it before entering in the next section. The next two sections, jejunum and ileum, have the function to absorb nutrients and here are present the first bacteria colonies. The small intestine is 5 meters long, on average, and has a transit time around 2 to 6 hours[1].

The large intestine is the zone in which the vast majority of gut bacteria harbors. It goes from the end of the small intestine till the anus. After ileum, the intestine continues with the cecum, then proceeds with the colon, which is divided in ascending, transverse, descending and sigmoid, and ends with the rectum and the anal canal. In our case scenario, the most interesting part is the colon, being the region where most of the overall gut bacteria resides and where low-degradable carbohydrates are fermented. The colon is ca. 150 cm long in adults and its functions range from electrolytes and water absorption to degradation of low digestible foods by commensal bacteria. Differently from small intestine, the time retention of food in the colon is much higher, being it between 30 and 40 hours, allowing a prolonged interaction between bacteria and food and an enhanced metabolites and nutrient absorption. It is formed by four layers: *mucosa, submucosa, muscularis externa* and *serosa*. The *mucosa,* which is our zone of interest, comprises the epithelium, the crypts and the *lamina propria,* which is the part between the crypts containing blood vessels and nerves. The *submucosa* is made of connective tissue and it allows the passage of nerves and blood vessels. The *muscularis externa* is composed of circular fibers and it functions as a muscular coat. The *serosa* is composed of areolar tissues and squamous mesothelial cells and is the external coat of the colon (**Fig. 1.1**)[2,3].

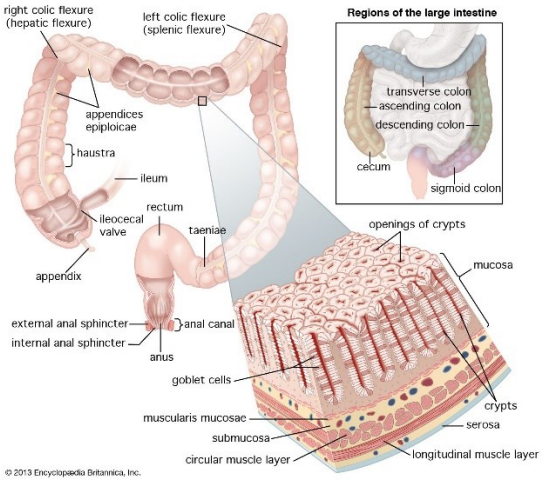


**Figure 1.1.** Large intestine structure[3].

The mucus in the colon, which serves to protect the epithelium from bacteria and shear stresses originated from food passage, is organized in two layers. The layer close to epithelial cells is about 50 μm thick and it is strongly adherent, the outer layer, about 150 μm thick, is loose and it is the part in which commensal bacteria are attached to, thanks to mucin-binding proteins. Both layers are principally composed of MUC-2 secreted by goblet cells, which is also the main component of the mucus produced by the cells we used in this thesis, Caco-2 cells, in dynamic conditions[4,5]. Nutrient absorption, especially in terms of electrolytes and SCFAs, which are the main metabolites obtained from bacteria fermentation, occurs mostly via paracellular routes. When this process does not work as it should, diarrhea or constipation may occur in case of a large fluid loss or fluid retention, respectively[6].

The intestine is also the principal organ involved in satiety feeling and nutrient sensing. This sensing is achieved through enteroendocrine cells able to secret hormones in response to environmental changes such as nutrient passage. The two main hormones involved in this process are GLP-1 and CCK. The release of these peptides activates a feedback mechanism that reduces food intake increasing satiety levels by regulating also glucose homeostasis. These hormones are taken up by the enteric nervous system giving information to the vagal afferents. In details, GLP-1 is mainly involved in gastric emptying, where greater GLP-1 levels are associated with a delay in gastric emptying. CCK is involved both in gastric motility reduction and in the activation of the secretion of duodenal enzymes[7].

### 1.1.2. Obesity

The intestine is a very delicate ecosystem, in which cells, nutrients and bacteria have to be perfectly balanced. When this balance is disrupted, inflammation may occur and this can lead to several diseases, starting from diabetes and obesity up to ulcerative colitis and colonic cancer. In this thesis, the main focus is obesity, as it is nowadays so world-wide spread that it is considered a pandemic[8]. Obesity develops from a prolonged imbalance of energy intake and energy uptake. Furthermore, it is considered one of the most common cause

of death, even more deadly than smoking, reaching over 500000 deaths per year in USA, due to its comorbidities[9]. Usually, obese subjects have a low-grade inflamed intestine, which is linked to the higher colon cancer rate with respect to lean subjects, with more than 30% increased risk of developing such cancer[10,11]. In fact, there is a strong connection between obesity and inflammation and between weight loss and inflammation reduction[12,13]. Among other differences from healthy subjects, intestinal nutrient absorption and permeability should also be addressed. In effect, it is common for obese people to have higher nutrient absorption associated to an increased intestinal membrane permeability[14]. This is mainly due to intestinal villi rearrangement, led by a different rate of stem epithelial cell differentiation and proliferation[15]. The release of hormones is also affected by obesity. In details, GLP-1 and CCK release is strongly decreased, leading to a loss of the satiety feeling, with a feedback mechanism that renders these peptides some of the major players in the obesity maintenance[7]. Another difference that should be noted is the gut microbiome composition, which will be addressed in the next paragraph.

### 1.1.3. Principal surgical treatments for obesity treatment

Currently, the most widely used approach to treat obesity is given by surgical treatments, from which Roux-en-Y gastric bypass and biliopancreatic diversion with duodenal switch are the gold standards, especially for rapid weight loss. In synthesis, both techniques are based on a double action. On the one hand, there is a reduction of the stomach, decreasing its volume and increasing the feeling of satiety; on the other hand, a portion of the intestine is cut and by-passed, allowing a reduction of the exchange surface area between cells and nutrients diminishing not only the passage of molecules but also the reactions occurring in the intestine while increasing the levels of peptides associated with appetite[16,17]. However, it is not sporadic the inconvenience of complications after such surgical interventions that can either occur right after the intervention or later in time. Among such complications, the most common ones are small-bowel obstructions, internal hernias and leaks, associated with early issues, and anastomotic strictures, among typical late complications[18]. Mortality rate after surgery should also be noted. It was found to be around 0.55% in a 30-day period, while 3.34% in a 10-year period. The principal cause of death was sepsis, with 42.7% of deaths caused by it, with cardiovascular diseases being the second cause, accounting for the 24.3% of all deaths. As for gender and age, male over 50 years were the most affected by complications and death when surgery deaths were not taken into account[19]. After such a delicate intervention, dietary habits change accordingly. For example, meat intolerance is common even years after the surgery. This leads in cascade to a decrease in the level of iron and vitamin B12 even though weight loss and arterial hypertension were consistently improved. So, protein supplements should be taken after the intervention for the whole lifetime[20].

Taken together, these results show that surgery may be implemented for obesity treatment, but we are far from finding a solution as mortality rates are still high and complications, sometimes even severe ones, are still common.

The idea which is at the basis of the surgical treatments is not dissimilar from what we want to achieve, which is the reduction of the intestinal surface available to nutrients degradation and passage across the membrane along with an increase in satiety levels. To do so, our strategy involves an oil film on the epithelium membrane which provides obstruction to molecules passage and at the same time inhibits bacterial enzymes, which are typically hydrophilic and cannot work properly in a lipophilic environment.

## 1.2. Gut microflora: eubiosis, dysbiosis and how to restore the balance

### 1.2.1. Gut microflora eubiosis

As previously stated, the human gut is an ecosystem comprising trillions of microbes interacting with the host[21]. The composition of the microbiota and their interactions play roles in different biological processes, such as insulin resistance, immunology and metabolism, and in the development of human diseases, such as Chron's disease, inflammatory bowel disease and cardiovascular diseases, being able even to influence the brain through the brain-gut axis[22]. Previously, it was thought that microflora was acquired after birth, but differences in gut microflora composition depending on the time and type of birth suggested the opposite and that placenta has already a microflora that inhabits the child before birth[23]. This is further validated by the fact that as the fetuses grow, they swallow a part of the amniotic fluid, resulting in a passage of the microbiota from the mother to the child[24]. Then, the microbiota changes during our whole life, depending on dietary habits, sport activity, age, diseases, use of antibiotics, environment and many other factors that put together shape our microbiota day after day[25].

Among the over 50 different phyla that inhabit our intestine, the vast majority of species belong to either *Firmicutes* or *Bacteroidetes* phyla, which together comprise almost 90% of the total bacteria mass. Whereas, on the genera level, *Bacteroides* account for almost 30% of the total bacteria[26]. As the factors influencing microbiota composition are various, it is not easy to determine a standard healthy microbiota. A healthy microbiota can only be defined as the microbiota that an healthy person possesses. Usually there is a lot of variety even in a lifetime for the same person. As this should always be kept in mind, it is also true that there are variations between healthy and non-healthy individuals, depending on the type of disease[27]. Differences between microflora of lean and obese subjects will be treated further in this thesis.

The analysis of the microbiome is something that has gained a lot of attention in recent years due to a novel sequencing technique focused on the 16s rRNA. This technique consists in targeting a small fraction of a bacteria ribosomal RNA, which is the 16s gene. 16s gene is present in each bacteria and has some highly conserved regions and other hypervariable regions that are unique at the species level. In details, after bacterial DNA extraction, PCR is performed and data are analyzed by comparing the results with libraries containing the information on the specific hypervariable regions[28].

Intestinal microflora is able to degrade foods not degradable by human enzymes or by stomach fluids and bile acids. Mostly, intestinal bacteria ferment food producing as metabolites gases and SCFAs, from which butyrate, acetate, propionate and hydrogen are the most common. Some of these SCFAs are then used by intestinal cells, transferred to other parts of the body or used by other commensal bacteria as energy sources[29].

Bacteria in the intestine occupy different locations. Some of them are in the lumen while others prefer to stay attached to the mucus layer. Localization of gut microflora is as important as difficult to understand. Usually, gnotobiotic mice, which are mice without gut flora, are fed with some bacteria typical of the human intestine and then sacrificed to observe their colonic bacteria[30]. Typically, a difference can be seen between two regions: interfold, the region near epithelia cells, and digesta, the inner part of the colon, as showed by Nava *et al* (**Fig. 1.2**). They found a significant difference in localization between *Bacteroidetes* and *Firmicutes* bacteria, where the first prefer to stay in the digesta region, while the second in the interfold region. In more details, *Ruminococcaceae* and *Lachnospiraceae* families were the species closest to the interfold region, meaning that they prefer to stay attached to mucus layer, whereas *Prevotellaceae* and *Lactobacillaceae* are the predominant families in the digesta region[31]. Welch *et al.* cultured 15 different species of human bacteria in gnotobiotic mice to observe their localization using FISH technique. First of all, they confirmed a higher presence of bacteria colonizing the colon with respect to distal small intestine. Additionally, they found that a bacteria belonging to the *Ruminocaccaceae* family, namely, the *Ruminococcus Torques*, was prevalently present in the section closest to epithelia cells[32].

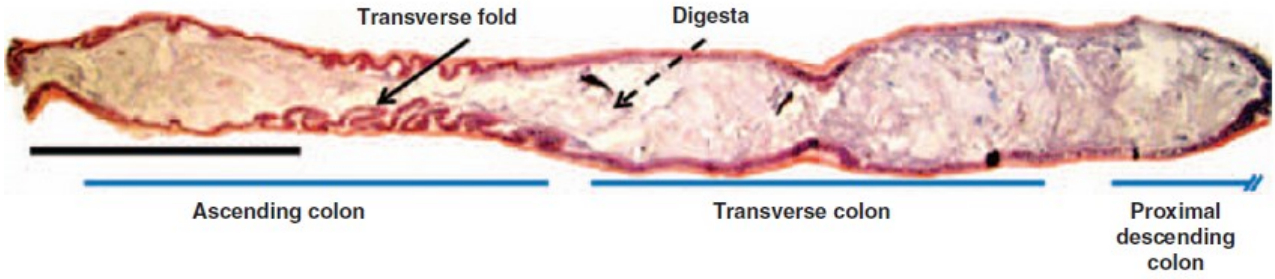


**Figure 1.2.** Colon regions. Significantly different bacteria population can be appreciated in transverse fold, the part near epithelia cells, and digesta, the inner part of the colon[31].

Together, these works, evaluating the position of commensal bacteria, open up a potential way in targeting bacteria resident near the mucus layer to act also at the cellular level.

Close relationships between dietary modifications, microbiota composition and healthy status have been established in the last years, but targeting and acting on a specific commensal gut flora bacteria is still a difficult task to be performed.

### 1.2.2. Gut microflora dysbiosis: obesity

Dysbiosis arises from a prolonged imbalance status, given by bad dietary habits or by diseases. Scientists are currently trying to understand the relationship between a particular disease and the respective microbiota composition. Many studies have been carried out analyzing the gut flora of obese patients finding that there is an overexpression of bacteria belonging to the family of *Firmicutes* with respect to *Bacteroidetes* family. This is the main difference between a lean and an obese subject gut flora composition[33,34].

These studies have been performed using metagenomics, i.e. the analysis of the genetic material recovered from fecal microbiota, comparing lean and obese subjects' microflora[35]. It has been observed a great difference in energy harvesting with an enhanced ability to ferment and degrade carbohydrates which in turn raises the amount of SCFAs produced. In effect, an increase in species that typically degrade carbohydrates was observed, especially *Ruminococcus*[26]. Moreover, obesity can lead to some comorbidities from which the most severe one is type-2 diabetes. This is due to the presence of high amounts of LPS. On the one hand, LPS is the principal element which induces inflammation, while on the other hand, it produces an immune response that increases insulin resistance[27]. It should also be noted that the vast production of SCFAs by *Firmicutes* bacteria can favor obesity by increasing the energy harvesting, calories intake and adipose tissue formation[36,37].

To better understand the impact of the gut flora on the overall health of a patient, a lot of effort has been made studying gnotobiotic or germ-free mice, mice with the gut flora of human subjects or mice with no gut flora at all, respectively[38]. In one of these studies, a microbiota from conventionally raised mice was transplanted to germ-free mice leading to a weight gain despite reduction in the food intake, this was associated, among all, to a major fermentation of carbohydrates[39]. The same research group demonstrated that germ-free mice are less prone to gain weight, being protected against diet-induced obesity[40]. Germ-free mice colonized with obesity-associated microbiota have been found to have increased body fat and energy harvest compared to mice colonized with lean donor microbiota[41].

A way in which obesity is currently treated is with FMT, that is the transfer of stool from a healthy donor to a patient with dysbiosis. After the transplantation, which usually occurs orally using a capsule, the receiver microflora appears similar to the donor one. Nonetheless, this improvement is only temporary if the patient does not change its dietary habits and life style[42]. To better observe the capacities of FMT on obesity, the group of Turnbaugh colonized germ-free mice with a microbiota taken from obese or lean subjects. After few weeks from the transplantation, they saw a significant increase in body weight of the obese microflora–colonized mice with respect to lean obese microflora-colonized ones. Once again, this suggests the importance of microbiota on harvesting energy and satiety level[43]. A similar work has showed how FMT from mice that has been fed with a normal-fat diet and undergoing exercise to sedentary and high-fat diet mice provoked a reduction in body and fat weight[44]. Regarding trials on humans, an interesting work has been published by Allegretti *et al.* They studied, in a double-blind test which lasted for 12 weeks the efficacy of FMT from a lean donor to obese subjects administered orally via capsules. After the trial, they found that safety was ensured

and microbiota and bile acids profile were closer to the donor ones. However, no significant changes in BMI were observed[45]. Similarly enough, Yu *et al.* administered FMT capsules from lean to obese subjects in a double-blind trial with a duration of 12 weeks. Also in this case, there was a reshaping of the microbiota but no significant improvement in weight loss or in insulin sensitivity were observed[46]. Together these studies showed the difficulties of FMT, especially when orally delivered, and how it is not sufficient alone to treat all the important factors that contribute to obesity that have been discussed in this paragraph.

### 1.2.3. Restoring the balance: prebiotics, probiotics and synbiotics

The use of prebiotics and probiotics is a possible strategy to treat obesity in a non-invasive manner. Prebiotics are defined as foods that are able to promote the growth of beneficial bacteria, while probiotics are live micro-organisms which try to restore the healthy microflora balance.

Regarding probiotics, the most commonly used ones are *Lactobacilli*, because they help to restore the *Firmicutes* to *Bacteroidetes* ratio and are highly associated with a healthy microflora. As an example, Jung *et al.* gave *Lactobacillus gasseri BNR17,* a strain isolated from human breast milk, to obese patients during a randomized, double-blind trial. Without drastically changing their usual behavior, the patients showed a reduction in weight and in hip circumference after 12 weeks. However, this change was not statistically different from the placebo group[47]. Similarly, Yang *et al.* administered a mixture of *Clostridium cochlearium* and *Lactobacillus acidophilus* to obese-induced mice for 17 weeks. Significant weight loss was observed together with glucose tolerance and insulin resistance. Moreover, 16s rRNA analysis demonstrated a reduced *Firmicutes* to *Bacteroidetes* ratio, indicating a reshaping of the microflora towards a healthy condition[48].

Trying to observe a change in microflora composition, Nagata *et al.* gave a solution of *Lactobacillus casei*, a strain present in human microflora, to obese children. After 6 months of exercise, a beverage containing the probiotic or a placebo was given to the children. They observed a significant weight loss and an increase in *Bifidobacterium* fecal concentration together with acetate production. Altogether, these results show the benefits of *Lactobacilli* as probiotics and their possible use in treating obesity[49]. A mixture of lactic acid bacteria was administered to obese patients for two weeks. Here, a deep bacteria genomic analysis was performed. It showed an increase in typical commensal bacteria while bacteria that are usually associated with metabolic disorders decreased significantly with respect to placebo-fed patients[50]. A group of mice who were treated in order with *Escherichia coli* and antibiotics to express the same microflora, were fed with two *Lactobacilli* strains for 7 weeks. The results showed a decrease in inflammatory levels and in the viable count of *Enterobacteriaceae,* which are associated with infections and inflammation, found by 16s rRNA analysis[51].

Regarding prebiotics, low degradable saccharides are the most implemented material, from which starch and its derivates are the most widely used. Nicolucci *et al.* gave to obese or overweight children a oligofructose solution enriched with inulin or a placebo in a double-blind test for 16 weeks. After 16 weeks, the blood tests showed a reduction in interleukin and in *Bacteroides vulgatus,* in the levels of triglycerides and a significant

weight loss in patients who consumed inulin. Those results were accompanied with an increase in *Bifidobacterium* species, trying to restore the healthy microflora balance[52]. Another work was made by adding inulin fructans, whey protein or a mixture of them in snack bars with a double-blind test on obese and overweight adult patients. Body weight and appetite loss were present in all the three configurations. However, inulin administration was essential for a significant increase in *Bifidobacterium* species[53]. This shows again how inulin can be effective in reshaping the gut microbiome.

Similar effects have been achieved with acacia gum polysaccharide, as shown by Rawi *et al.* which simulated colon microflora composition and microenvironment in an *in-vitro* situation. They observed an increase in SCFAs production, mainly acetate and butyrate, and a proliferation of *Bifidobacterium* with respect to *Clostridium*[54]. Naturally, this is only a first step experiment, as the interaction with cells were not taken into account, giving just a glimpse of the real *in-vivo* situation. The synergic effect given by the co-administration of agavins and banana flour was evaluated by Alvarado-Jasso *et al.* in obesity-induced mice models. The mixture, with respect to control and to single elements, effectively reduced energy intake and body weight, while ensuring a higher production of SCFAs. This may be due to the intestine zone where the two compounds act as agavin is principally degraded in the proximal colon, while banana flour in the distal colon. However, the gut microflora composition, a crucial aspect when dealing with diet and prebiotics, was not evaluated[55].

Another type of prebiotic, as previously stated, is starch, especially when administered in its resistant form, which is called RS. RS is usually divided in four categories, from which the first three are naturally occurring, while the last one consists in a chemically-modified starch. In details, RS1 is a coarse type of starch which is still protected by cell walls. RS2 has a high amount of amylose and it has a compact crystalline structure, those properties make difficult to gelatinize it. However, even being a RS2 type, potato starch can be easily gelatinized starting from a temperature above 60°C. RS3 arises when starch is gelatinized and then cooled down, with 4°C being the ideal cooling temperature[56]. A study was performed in order to assess the difference in prebiotics efficacy among the different RS types by Liang *et al.* by studying their effects in an *in-vitro* simulated gut fermenter. On the overall, all types of RS were associated with a lessening of *Firmicutes* to *Bacteroidetes* ratio and an increase in SCFAs. In details, RS2 was the one which showed the most interesting prebiotic capabilities because after its addition, the bacteria present in the fermenter produced the highest amount of propionate and butyrate and promoted *Prevotella* species growth[57]. Tests have been performed to evaluate its performances in microflora shaping and on insulin resistance, two fundamental aspects involved in obesity. A first work, made on more than 400 overweight or obese people, was performed in 2019 analyzing fasting of insulin and glucose as well as insulin sensitivity. A dose of RS ranging from 10 to 45 g per day was administered. The outcomes of the study showed a reduction in insulin and glucose fasting along with an improvement in insulin resistance[58]. Nonetheless, as interesting this may seem, data on initial and final microbiome composition of the patients is a crucial aspect that should always be considered when performing such experiments and that is absent in this case. Going in this direction, Thompson *et al.* gave RS obtained from sago palm tree to fat-induced rats and analyzed their microbiome by collecting fecal samples every two

weeks together with SCFAs production. They found a not significant increase in butyrate and acetate concentration as well as a significant increase in typical healthy commensal species such as *Bifidobacterium* and *Lactobacillus*¸ demonstrating how RS acts especially on microflora composition[59]. RS can be obtained from different sources. As an example, Fu *et al.* administered banana RS to obesity-induced mice for 6 weeks and analyzed the outcomes in terms of plasma glucose and insulin concentration and gut flora composition. They found a significant reduction of glucose and insulin levels. Furthermore, banana RS was able to shape the gut microflora in a way which is closer to the healthy situation, favoring *Bacteroidetes* species in contrast to *Oligella* and *Tenericutes* species[60].

Synbiotics are a mixture of prebiotics and probiotics and are used for obese treatment as well, because they can take advantage of both probiotics and prebiotics properties and gut flora re-balance. Thiennimitr *et al.* combined *Lactobacillus Paracasei* and xylooligosaccharides for 12 weeks to treat obesity in a murine model which were resistant to insulin, studying their effects on inflammatory status and intestinal microflora. They found a decrease in gut inflammation, *Enterobacteriaceae* levels, and in *Firmicutes* to *Bacteroidetes* ratio while there was a significant improvement in their metabolism[61].

On the overall, these works gave us the idea that changing gut flora composition, with small or no alteration in the patient attitude, could lead to weight loss and reduction of energy harvest. However, all the procedures that have been done so far are related to fecal transplant from a healthy donor or to the use of prebiotics/probiotics in order to stimulate microbiota growth, acting just on one of the myriad of aspects involved in obesity[62,63]. Furthermore, starch seems a good candidate not only for colon deliver, which will be addressed later in this thesis, but also as a prebiotic. However, as the idea of prebiotics is fully accepted nowadays, little is known on their interaction with bacteria and how to modulate a single bacteria strain specifically, naturally present in the human gut, i.e., to promote or inhibit its proliferation without using antibiotics.

### 1.2.4. *Ruminococcus Bromii*

To choose the bacteria of interest, we firstly focused our attention on bacteria typical of the gut flora of obese subjects, so that we are able to make them lose weight and to reduce the insurgence of cardiovascular and colonic diseases by reducing its proliferation.

As said before, obesity is correlated with a higher *Firmicutes* to *Bacteroidetes* ratio, so it is needed to reduce *Firmicutes* concentration while increasing *Bacteroidetes* species. Among the *Firmicutes* bacteria family, the keystone bacteria capable of complex carbohydrates degradation, in the form of starch and RS, is *R. Bromii*[64]. It has a complex multienzymatic structure, called amylosome, which possesses the ability of degrading starch thanks to the glycoside-hydrolase 13 family enzymes specialized as α-amylases and pullanases. Such enzymes act by cutting the 1,4-α-D-glucosidic bond typical of starch molecules. In fact, the enzymes of *R. Bromii* have dockerin and cohesin modules which can interact one with each other forming the superstructure of the

amylosome (**Fig. 1.3**)[65,66]. Such choice was made because starch degradation is associated with an increase in SCFAs levels. In healthy conditions, SCFAs can regulate energy homeostasis and have beneficial effects. However, when there is an overproduction of SCFAs, such as in the case of obesity, the homeostasis is lost, favoring an enhanced energy harvesting and a subsequent adipogenesis, as explained above[36,37]. Therefore, in our case scenario, the reduction of *R. Bromii* proliferation is essential to recover the healthy status.

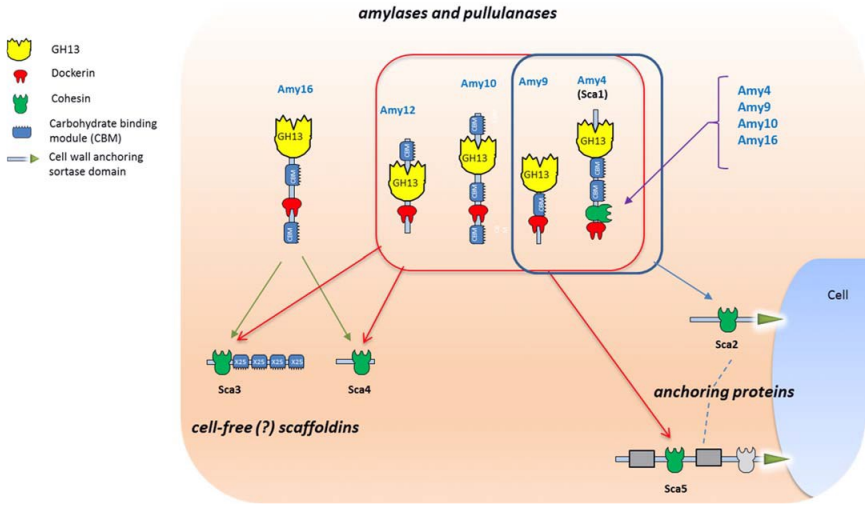


**Figure 1.3.** The structure of amylosome, the superstructured enzyme typical of *Ruminococcus Bromii*. Dockerin and cohesin interact together to bind different amylase enzymes, with enzymes belonging to glycoside-hydrolase 13 family[66].

Moreover, the metabolites of *R. Bromii* can promote the growth of other *Firmicutes* bacteria, being a keystone species in degrading complex carbohydrates, and being it on top of the starch degradation pyramid[67]. For these reasons, our aim is to produce a well-defined carrier that, interacting with *R. Bromii*, will be able to reduce its activity and the activity of other bacteria in cascade.

## 1.3. Oil-inducing satiety

In the recent years it has been discovered that oils have a satiety effect on the patient if delivered to the intestine. This occurs especially because of the ileal brake, a feedback mechanism activated by nutrients, especially fat, that has a potent effect on satiety[68].

This is due to a cascade of events that lead to an increase in the CCK peptide, that serves as a satiety signal. It acts in two ways: on the one hand, it gives a negative feedback signal to reduce the amount of food consumed; on the other hand, it gives a positive feedback signal to stimulate digestion[69,70]. Naturally, this depends also on the type of oil that has been given. For example, Maljaars *et al.* found out that oils which present polyunsaturated fatty acids are more likely to induce satiety with respect to saturated ones[71]. An additional study was performed by Prater *et al.* by studying cottonseed oil and olive oil effects on satiety as they are rich in polyunsaturated and monounsaturated fats, respectively. In particular, they tested them on adults during an

8-week-long experiment. Cottonseed oil was able to decrease energy and food intake, both associated with a suppression of appetite, in comparison with olive oil[72].

This was further investigated by Jurgonski *et al.* who demonstrated how a diet rich of saturated fatty acids led to obesity and higher intake of food with respect to a diet rich of unsaturated fatty acids, especially soybean oil. In the latter case there was a smaller percentage of butyrate production associated with lower dietary intake and less occurrence of dietary disorders[73].

The way in which the oil is presented to the intestine also affects the satiety effect. In fact, Maljaars *et al.* found that smaller droplets, with a diameter of ca. 1 μm, significantly affected satiety, gut peptide release and gastric emptying with respect to larger droplets, having a diameter of ca. 16 μm[74].

Furthermore, soy may have a beneficial role in treating obesity. It can reduce body weight and fat mass, improving insulin resistance, which is one of the hallmarks of obesity in humans[75]. Soybean oil can also be genetically modified to further limit obesity development[76].

For these reasons we chose soybean oil in its regular form as the oil phase, due to its actions on reducing obesity occurrence and increasing satiety levels and we chose a carrier with a diameter in the range of few μm to increase as much as possible the satiety effect.

## 1.4. Carriers for intestinal applications

### 1.4.1. Targeting strategies

To reach the intestine one of the most favorable route is by oral ingestion. However, any carrier that has to act in the gut must pass through the GIT where it is subjected to harsh changes in pH and to several enzymes' activity[77]. So, one of the crucial aspects when developing such a carrier is the resistance to pH and enzymes. Nonetheless, this strategy alone is not sufficient if a local administration and a single-bacteria targeting are desired.

Commonly, target-specific carriers are developed by taking advantage of bacterial external membrane proteins and ligands. Among them, adhesins are fundamental for colonization as they are the first step for bacteria-host interaction. Adhesins attach to carbohydrate receptors, glycoproteins or glycolipids on the host and any bacteria can express several of them, specific for their action and the type of interaction with the host[78]. As this is true, also the inverse process occurs, which is the adhesion of cells to bacteria by the recognition of bacteria carbohydrate receptors, a process that is the basis of bacterial recognition by the T cells of the immune system. Moreover, this recognition process leads to a cascade that is the main driver of intestinal inflammation[79].

For example, one idea is to use epithelial cells membranes as drug carriers as they naturally express proteins able to recognize bacteria. This strategy was performed by Angsantikul *et al.* for antibiotic delivery against

*Helicobacter pylori*, an infectious bacteria. They developed nanocores of antibiotics coated with gastric epithelial cell membranes. The result was an enhanced bactericidal effect *in-vitro* with respect to free antibiotic or uncoated nanoparticles. This can be explained by the host-pathogen interaction, which is crucial when developing an infection. This is also a strategy for active targeting as the bacteria, recognizing the protein on the outer membrane of the coated nanoparticles, attach to them and are more prone to be influenced by the antibiotic effect[80]. As this seems a good strategy, being this kind of cells naturally able to survive in GIT conditions, it is also vastly time and money consuming, without mentioning the high quality controls they have to pass to avoid any unwanted interaction with the host[81]. On the overall, these do not favor a clinical translation.

Bacteria have been targeted through specific moieties that can bind to bacterial membrane in a work published by the group of Capeletti. They covered silica nanoparticles with gluconamide moieties able to recognize and to attach to the bacterial membrane of gram-negative bacteria. The particles showed no toxicity and avoided unspecific protein adhesion on the nanoparticles, avoiding the process called protein corona which can modify nanoparticles properties. However, in this case, the specificity was only towards gram-negative bacteria, that have an outer membrane different from gram-positive bacteria, because of the outer lipopolysaccharide layer[82].

Regarding the interaction between nanocarriers and bacteria, one of the most interesting studies takes advantage of the production of hydrogen sulfide ($H_2S$) by the pathogen bacteria *Salmonella*. Here, Mu *et al.* produced $H_2S$-cleavable nanometric amphiphilic molecules loaded with CIP, as an antibiotic. They found out that CIP was actually released at the site of infection when orally delivered in *in-vivo* tests. After 4 hours from administration, CIP was mostly present in intestine and almost absent in the bloodstream, thus avoiding a quick absorption of antibiotics in the systemic circulation[83].

Peptides have also been implemented in order to specifically target bacteria, as done by Hussain *et al.* Using phage display, they were able to derive the proper peptide sequence that targets *S. Aureus*, a pathogen bacteria responsible for a wide variety of infections in humans. This peptide has been conjugated on the external shell of silica nanoparticles loaded with vancomycin, an antibiotic. They found out that the nanoparticles suppressed efficiently *S. Aureus* infection in mouse *in-vivo* models and accumulated in the site of infection, when intravenously administered, confirming the nanocarrier specificity as demonstrated by a poor reaction against *Pseudomonas* bacteria-infected mice[84].

### 1.4.2. pH resistant carriers

As stated above, the carrier has to survive in the severe conditions dictated by the digestion process, with particular attention given to the stomach, for its highly acidic environment. Chitosan, a polymer obtained by chitin, is a pH resistant polymer and can be used as a stabilizer for microparticles produced by emulsification process, as showed by Anal *et al.* Those microparticles, less than 10 μm in size, when coated with chitosan can survive up to 12 hours in a simulated gastric fluid with pepsin. As a test drug, ampicillin was loaded into the

above-cited microparticles and an optimal release behavior was found with a MIC able to inhibit the growth of *S. Aureus*[85]. Oligo-chitosan and de-esterified pectin were implemented to form hydrogels microbeads for colon delivery. The microbeads were obtained through ionic gelation with the consequent formation of cross-linking between the two molecules. By varying the amount of pectin, they observed that particle size increased as the pectin percentage increased, going from about 820 to 930 μm. Quercetin, a molecule belonging to the family of flavonoids, has been entrapped in the microbeads and its release tested in simulated fluids. The amount of quercetin released was close to 0% in simulated gastric and intestinal fluids while it reached almost 100% when put for 12 hours in colonic simulated fluids[86]. This shows once again the efficacy of chitosan-based carriers for localized release in the colon.

In order to treat ulcerative colitis, Yang *et al.* designed a co-delivery of small interfering RNA and berberine in nanoparticles embedded in a chitosan and alginate hydrogel. In details, they designed nanoparticles of 270 nm made of hyaluronic acid covered with chitosan that can be recognized by macrophages and can liberate $CO_2$ at a pH similar to the colonic one, delivering the small interfering RNA for regulation of barrier function and integrity. The co-delivery occurs by embedding the nanoparticles in the hydrogel where berberine was present. They tested this system both *in-vitro* in an LPS-induced inflammation culture and *in-vivo* in ulcerative colitis-induced mice. In both cases they saw a reduction in cytokines associated with inflammation[87].

Following the idea of using a pH resistant polymer, inulin has been used by Mandracchia *et al.* which formulated an inulin-based conjugate to achieve pH sensitivity which did not procure drug leakage at pH 1.2 while obtaining a high release, around 80%, at pH 6.8[88]. Another group did achieve a better kinetic profile using an inulin-based enzyme carrier, but the drug efficiency loading was pretty low, about 10%[89]. Inulin has also been utilized in O/W emulsions using sodium caseinate as a surfactant agent and by adding also konjac glucomannan. By changing the ratio between inulin and glucomannan, droplet size and stability changed considerably, ranging in the tens of microns. In details, droplet size and creaming decreased as the percentage of glucomannan increased. Along with that, viscoelasticity properties increased too as the emulsion assumed a more gelatinized structure, associated to a higher stability. Oil fraction was an interesting parameter too as the droplet size was highly dependent on the oil percentage, with smaller droplets associated with smaller quantities of oil, with the lowest being 20 wt%. As this seems an interesting carrier for inulin probiotics properties, further studies on colon delivery are yet to be performed[90].

The carriers can also be used to deliver prebiotics rather than antibiotics, which, even in case of local administration, can lead to multi-resistant bacteria. As a matter of fact, Mei *et al.* designed a carrier obtained through a shell made of a mixture of protamine and calcium alginate and a core of calcium alginate in which *Lactobacillus casei* was loaded with a final size of about 4 mm. The carrier was protected from the stomach low pH because of an obstruction of the pores by protamine molecules which hindered diffusion. Once reached the intestine, where the pH is neutral, protamine and trypsin worked together to easily and rapidly dissolve the carrier. They demonstrated these properties in simulated stomach and intestine fluids[91].

### 1.4.3. Starch carriers for colon delivery

A polysaccharide which is not degraded by low pH or human enzymes is starch, especially in its resistant form[92]. It can easily resist till the colon and be degraded there by bacteria, from which, we recall, *R. Bromii* is the keystone one[93]. Chen *et al.* developed a protein drug matrix system composed of pre-gelatinized starch cross-linked with bovine serum albumin. They analyzed the controlled release in simulated gastric, intestinal and colonic fluids. Thanks to the modification of the starch, especially the pre-gelatinization treatment, the enzymatic degradation was delayed. This allowed a slower and more precise delivery of the drug in the simulated colonic fluids[94]. By blending acid hydrolysis-carboxymethyl starch and xanthan gum and forming microparticles by spray-drying, Jiang *et al.* achieved an optimal stomach resistance and intestinal absorption of vitamin E. They aimed at delivering it to the small intestine and they were able to do so by finding and tuning the right ratio between carboxymethyl groups, xanthan gum and starch. However, the test was only performed in simulated conditions considering just the pH of stomach and small intestine, without any consideration on the colon and retention time[95].

Starch has been used to deliver antitumoral drugs, such as paclitaxel. As an example, Zhao *et al.* coated a starch carrier with chitosan entrapping paclitaxel in it. The chitosan addiction was useful because the porous starch could not retain correctly the paclitaxel inside. By adding chitosan, they were able to obtain a more controlled and localized release right in the colon, where the total release was over 80% in simulated GIT conditions[96]. The same group used a similar strategy, aiming to improve the paclitaxel entrapment thanks to hyaluronic acid. In effect, hyaluronic acid reacts with starch forming hydrogen bonds and cross-linking. This allowed an almost doubled cellular internalization. Furthermore, they performed an *in-vivo* administration to mice, from which they observed the effectiveness of the localized release[97].

Spray-drying technique was used to produce mucoadhesive microspheres of pre-gelatinized cassava starch succinate, a physically and chemically modified starch. The particle size ranged from 2 to 28 μm and encapsulation efficiency was near 90%. However, their muco-adhesive properties were not properly tuned as they indistinctly bound to gastric or intestinal mucosa and had a faster drug release in a lower pH, losing part of the pH modulation typical of natural starch[98].

Starch can be modified in different ways. One example is given by acetylation. This process can enhance the absorption of SCFAs at the colon level. It has been previously shown that acetate levels are correlated with anxiety. For this reason, Kimura-Todani *et al.* administered acylated starch to mice. They observed a shift in anxiety-like behaviors towards a normal behavior of mice, with respect to mice which were fed with starches that were modified with other SCFAs, namely butyrate and propionate, in a process similar to acetylation. Moreover, the acetylated starch was also able to promote a shift in microbial community towards acetate-consuming species, *Bacteroidetes* among all[99]. Another group used acetylated starch in order to protect microparticles of ca. 500 μm from GIT conditions and to deliver them specifically to the colon. To do so, they conjugated this kind of starch to a glycoprotein enhancing the adhesive properties of RS. In fact, the

glycoprotein is used to achieve a better interaction with the epithelium stratum by interacting with cell receptors. They tested the microparticles properties in mice with induced type-2 diabetes by delivering insulin. Insulin resistance diminished after oral administration of the starch-coated microparticles keeping glucose in a healthy range for about 50 hours[100].

Starch crystallinity effect was studied by Putro *et al.* by changing the preparation method of nanoparticles, whose size ranged from 80 to 180 nm depending also on surfactant modification. In details, precipitation method resulted in a lower crystallinity with respect to acid hydrolysis. Drug loading capacity was enhanced in case of lower crystallinity. Furthermore, the charge is another parameter important when dealing with drug delivery. As a matter of fact, they saw a more controlled release in case of cationic modified starch, with respect to a burst release typical of anionic starch[101].

An enzymatically modified RS3 was used as coating of microparticles, with a size of about 1 μm, which were then used to deliver orally ciprofloxacin HCl. The starch was obtained after a treatment with pullulanase and amylase enzymes. Firstly, they attested the properties of such a formulation as a prebiotic, founding an increase in *Lactobacillus reuteri* viable count. The microparticles, obtained through the single-emulsion evaporation method, were pH resistant, as a sustained release was observed only at a pH equal to 7.8, close to the colonic one. Furthermore, the release was also associated with anaerobic bacteria, as they were able to degrade the external starch film[102]. Starch degradation for active and localized release is also part of the strategy proposed in this PhD work, however we avoided the use of antibiotics, preferring oil for the formation of a film on cell epithelium and bacteria, to limit cell absorption from one side and bacteria SCFAs production from the other side. Additionally, by using an oil core, we also aim to deliver an anti-inflammatory molecule to treat inflamed gut tissue.

Regarding probiotics, three strains of *Lactobacilli* were efficiently encapsulated in microspheres of RS4 obtained from rice starch. The microspheres had a diameter of about 45 μm and were able to protect all the strains from simulated gastric fluids. The storage capabilities were also tested by measuring the amount of viable bacteria when stored at 4°C. They found that after two months the bacteria were still alive. Nonetheless, few tests were performed on bacteria release[103].

### 1.4.4. Curcumin delivery to the colon

Cur is a plant extract which has potent anti-inflammatory properties but which shows poor bioavailability when ingested in free form[104]. It has been shown that cur can prevent and treat intestinal inflammation when protected from the GIT harsh conditions. In fact, cur may prevent and treat chronic inflammation by playing a major role in inflammation pathways, leading to a reduction of cytokines levels, while improving barrier permeability and functions[105]. Recently, cur effects on obesity were studied too. Cur interacts with white adipose tissues, reducing the amount of adipocytes while treating the low-grade chronic inflammatory states typical of obese subjects' colon[106]. Among the most promising colon drug delivery systems that aims to deliver cur, there is a

study made by Hales *et al.* They made *in-vivo* tests on rats induced with ulcerative colitis and saw marked benefits from curcumin loading in a protected polymeric microcarrier, made by a mixture of polycaprolactone and Eudragit® FS, with respect to free cur. The benefits were evaluated in terms of oxidative stresses and inflammation status[107].

To exploit cur properties, nano-micelles were formed by conjugating cur with starch through acid-labile ester linking. The micelles were formed by self-assembling with a final size around 70 nm. In this way, cur was effectively protected from degradation enhancing its solubility and bioavailability along with augmented effects of its anticancer and antioxidant properties[108]. Another application for starch-cur conjugation is the treatment of inflammatory bowel disease. In a recent work by Xu *et al.*, they took advantage of α-amylase expressed by bacteria in the colon in inflamed status to let the outer shell of the nanocarrier, made of starch and about 50 nm in size, be degraded so that cur can be liberated together with nanoparticles containing dexamethasone, an anti-inflammatory glucocorticoid achieving a double action which was tested *in-vivo* on mice models. This approach is not dissimilar to ours, considering, in our case, the major role played by oil as bacteria quencher and barrier thickening agent[109]. With the idea of taking advantage of microbial degradation of starch in the colon, Amhad *et al.* developed bioadhesive microspheres made of rice starch, ranging from 110 to 485 μm in size. They studied the degradation of the microspheres in the GIT, the distribution of metronidazole, an antibiotic, delivered inside the microparticles *in-vivo* and its action on *Bacteroidetes Fragilis in-vitro*. They found that most of the carriers resisted to the GIT conditions till the colon, where it was degraded and, subsequently, the drug released[110]. Nanoparticles obtained from simple and acetylated-banana starch were tested for curcumin delivery by Acevedo-Guevara *et al.* in simulated digestive fluids. The nanoparticles' size was about 250 nm for both formulations. They saw that cur was better protected when acetylated-starch was used, maybe due to the stronger hydrogen bonds that form between cur and starch. This, in turn, allowed a more controlled release of cur with respect to native starch nanoparticles[111]. Cross-linked starch nanoparticles were used for protecting cur and their effects on inflamed epithelium were studied by Salah *et al.* in a Caco-2 model. The inflammation was obtained by adding TNF-α in the culture. Cur was correctly delivered and it acted majorly on endocytosis pathway. Furthermore, levels of cytokines associated with inflammation decreased, whereas levels of cytokines associated with anti-inflammatory effects increased[112].

Starch can also be used as a stabilizer for O/W emulsion production[113]. Lu *et al.* were able to protect cur from the GIT conditions by delivering it inside Pickering emulsions made from starch, with a final size of 43 μm. Moreover, they analyzed anti-cancer response in a Caco-2 cell model. Differently from digested free cur, digested emulsions were able to strongly reduce cell viability, showing an enhanced delivery ability and protecting effect[114].

We chose the emulsion approach because, having an oil core, lipophilic molecules, such as the vast majority of antitumoral and anti-inflammatory compounds, can be easily loaded and delivered. Furthermore, the oil can act as a quencher for bacteria activity and as a thickening agent for intestinal barrier.

## 1.5. *In-vitro* platforms for intestinal studies

### 1.5.1. Evaluating intestinal barrier properties

*In-vivo* studies are a prerequisite in order to have a drug or a carrier accepted by the food and drug administration. However, be it for ethical, economical or practical reasons, there is the urge of cutting down the number of animal studies. To do so, there are *in-vitro* platform that try to reproduce the micro and macroenvironment typical of an *in-vivo* situation. The gold standard, among cell types, is given by Caco-2 cells. These cells are obtained from human colon adenocarcinoma and are widely used as models for intestinal studies also in case of healthy status due to their ability to differentiate. In effect, it has been shown that Caco-2 cells form a cell monolayer which has various properties in common with human colonic barrier[115].

In order to validate an *in-vitro* model there are few aspects that should be considered. Among them, the most important are permeability and cell barrier integrity. Regarding permeability, the tests are usually done with small molecules that can pass by transcellular transport from a donor phase to a collector phase. Usually, such molecules are fluorescent or radiolabeled in order to be followed and quantified during their passage[116]. By measuring their passage, it is possible to calculate the apparent permeability of a particular compound. On the other hand, the cell barrier integrity is commonly considered by using TEER measurements. These measurements take advantage of the passage of ions through the barrier. A current is applied between two electrodes, one above and the other below the cell barrier, and the voltage is sensed. The measure is easy to make and does not damage cells as long as the current is not high enough. However, the results are difficult to interpret as they are the sum of various biological electrical parameters. A major role is played by the electrical model that is used during these measurements. The most accurate model is the one which considers an external resistance, given by the fluid, in which the cells are submerged; two resistances which consider ion permeability on the apical and basolateral parts of the cell layer; two capacitances representing apical and basolateral cell layers; a resistance representing the passage of ions through the tight junctions (**Fig. 1.4 A**). In order to simplify the model, the apical and basolateral properties are coupled, representing the whole cell layer (**Fig. 1.4 B**) and then transcellular and paracellular resistances are coupled together forming the TEER. So, the final circuit is formed by an external resistance, being the fluid, in series with an R-C circuit where R is the TEER and C is the capacitance of the cell layer (**Fig. 1.4 C**)[116,117].

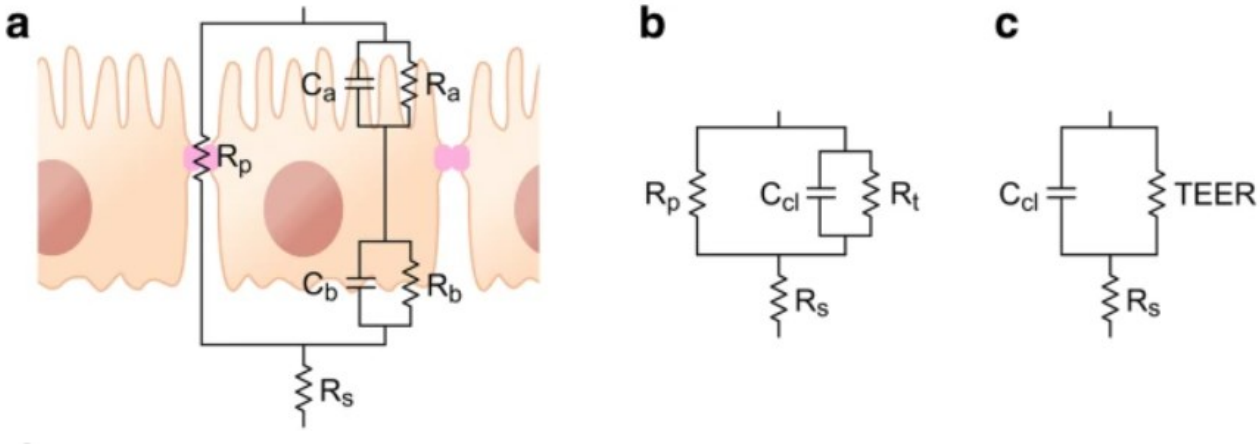


**Figure1.4.** Equivalent electrical circuit schematization of the passage of molecules through intestinal cells (a). Simplification of the circuit due to similarities between apical and basolateral sides (b). Final schematization arising from the coupling of paracellular and transcellular resistances (c)[116].

### 1.5.2. Static permeable supports

The first and most used platform to assess drug permeability is given by Transwell® systems. They consist in wells with a polycarbonate membrane on which cells adhere. They are composed of a donor phase, usually in the apical side, and a collector phase, usually in the basolateral side. The cells grow on the membrane and polarize thanks to the formation of a liquid-air interface after almost two weeks of culture (**Fig. 1.5**). Then, in the third and last week, the cells polarize and differentiate in order to form the classical villi structure of the intestine[118].

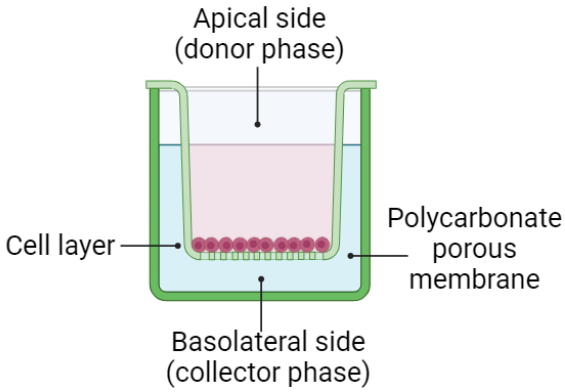


**Figure 1.5.** Transwell® typical configuration. Molecules are put in the donor phase and their passage in the basolateral side is analyzed. Image done using Biorender.com.

Usually, Transwells® are used as a first screening platform for drugs. As a matter of fact, Denaro *et al.* proved the transport and anti-inflammatory properties of ideain, an anthocyanin, in such model. They were able to exclude the passive transport in favor of an active one involving SGLT1 and GLUT2, hexose transporters typical of Caco-2 cell line. Moreover, studying apparent permeability they were able to discriminate the *in-vivo* absorption, which is confirmed by pharmacokinetic studies. By measuring interleukin levels in an LPS-

induced inflammation model before and after ideain administration, they were able to assess its anti-inflammatory properties[119]. Transwell® systems have also been used to study the effects of adverse molecules and the differences in their route of administration. As an example, Parajuli *et al.* studied arsenic exposure on T84 cells, derived from a lung metastasis of a human colon carcinoma, cultured on a Transwell® in case of oral and intravenous administrations. They differentiated the two routes by changing the concentration of arsenic in accordance to the ones used for each of them and by changing the location of the delivery, in the apical and basolateral part of the membrane for oral and intravenous, respectively. Analyzing TEER, cytotoxicity and tight junction expression, they found a more severe reaction for the system mimicking intravenous injection, which showed a more damaged barrier[120].

The system can also be complicated by adding different cell types. One example is the addition of dendritic cells as they are responsible of the first response to external agents in the intestine. Chalubinski *et al.* studied the effect of oxidized cholesterol in the case of a co-culture of Caco-2 monolayer and dendritic cells. The addition of dendritic cells did not change TEER values, and so the barrier integrity, whereas made interleukin concentration increase. However, when 7-ketocholesterol was added, a diminishing in barrier properties was observed together with a decreasing of interleukin expression induced by dendritic cells[121].

Mucus formation is of fundamental importance when dealing with absorption as it gives an additional barrier and resistance to drug passage. As Caco-2 cells produce small to none mucin in static conditions, they are usually accompanied by HT29 cells, which are also derived from human colon adenocarcinoma but can be modified in order to overexpress mucin, in a form called HT29-MTX [122]. One of the first works on co-culture in a Transwell® system was performed by Mahler *er al.* to study iron bioavailability obtained from food digesta. Increasing HT29-MTX cells percentage in the culture, over the physiological value, resulted in a decrease in iron bioavailability as Caco-2 cells are fundamental for absorption studies. However, when staying in the more coherent ratio of 9 to 1 for Caco-2 cells with respect to HT29-MTX cells, the model was able to predict the absorption in accordance with human studies[123]. A similar work, studying the interaction between these two cell lines, was performed by Béduneau *et al.* They tuned the permeability of a cell monolayer cultured in Transwell® systems by changing the day in which they added HT29-MTX cells to the initial Caco-2 culture. Paracellular permeability was closer to an only HT29-MTX culture when these cells were cultured the day before with respect to Caco-2 while, on the other hand, the permeability was closer to a cell monolayer containing Caco-2 only when they were added after 7 days. Permeability was not influenced by the co-culture when the HT29-MTX seeding happened between 1 and 3 days from initial Caco-2 culture. The results were obtained by TEER and by rhodamine 123 and lucifer yellow paracellular permeability assays[124].

Antunes *et al.* further complicated the model by adding also Raji B cell line, human lymphoblastoid cells. They co-cultured Caco-2 and HT29 cells in the apical part of the Transwell® while added Raji B cells in the basolateral part of the membrane. They studied insulin permeation as a drug model finding out a greater permeability in case of the triple culture in comparison to more classic HT29/Caco-2 culture. Furthermore,

they studied also an inverted model changing the position of HT29/Caco-2 and Raji B cells, putting them on basolateral and apical part of the membrane, respectively. By doing so they observed a greater absorption of insulin in the case of normally oriented cells[125].

Caco-2 cells have shown to express interleukin in inflammatory status. In effect, Leonard *et al.* in a recent work described the interaction of various intestinal cell lines to different inflammatory molecules, finding that Caco-2 cells were the most responsive ones. Once assured this, they tested the inflammation status by adding macrophages and dendritic cells to the Caco-2 monolayer in the Transwell® in a collagen matrix obtaining a similar 3D culture. In this case the inflammation was higher as demonstrated by interleukin levels with respect to the single cell model, validating the presence of macrophages and dendritic cells as a useful tool to achieve a better understanding of the *in-vivo* situation[126].

Gut microbiota can be added to have a better understanding of host-bacteria interaction. As an example, Zhang *et al.* cultured in a Transwell® *Bacteroides thetaiotaomicron* on a colon monolayer. The bacteria were added after four days from the formation of the monolayer. The contact lasted just for 8 hours. The strains were engineered as to carry a genetic circuit able to respond to some inducers typical of different colonic microenvironments. When the inducers were present, the circuit activated and the bacteria became luminescent[127]. To study host-bacteria interactions in inflamed tissues, Mohebali *et al.* cultured a mix of Caco-2 and HT29-MTX cells in a Transwell system and added three strains of commensal bacteria, after obtaining inflammation through LPS and interleukins. The addition of commensal bacteria assuaged the effects of inflammation, namely the level of interleukin-8 and the barrier integrity, computed through TEER measurements and permeability assay. This demonstrated that by reverting the dysbiosis, it is possible also to reduce the diseased status[128].

As these systems are useful and widely employed, they are time consuming as it typically takes 21 days for the cell monolayer to be fully developed. Few alternative methods have been proposed, consisting in 7 days of culture to obtain the final cell monolayer[129]. However, even if the shortened culture had similar properties with the long-term one, this cannot be considered a valid platform as it still lacks important features typical of intestinal *in-vivo* environment.

### 1.5.3. Organoids

The aim of better mimicking *in-vivo* conditions led to the idea of 3D structures that are able to form structures similar to the organs' ones. Organoids are defined as 3D masses of cells that, by proliferating, self-organizing and differentiating, can resemble a real organ. Usually the starting point is to take biopsies from patients' tissues and for this reason they are majorly involved as diseases platforms for drug screening and precision medicine[130]. In case of intestinal diseases there are several studies enlightening the protocols for an appropriate culture of colonic tissues and their ability to reproduce intestinal diseases, such as colorectal cancer and inflammation[131]. One example is given by a recent study by Rodrigues *et al.*, focusing on the effects of

doxorubicin, a potent anti-cancer drug that has several side effects. They studied doxorubicin effects on 3D colon and small intestine organoids and tuned drug concentration as to equalize the one commonly used in colonic cancer treatment. They analyzed the results in terms of apoptosis and cell viability by transcriptomics. The most affected pathways were the ones associated with oxidative stress and mitochondria functionality, impairing the overall growth and proliferation of cells[132].

By taking single cells and crypts from mice intestinal organoids, Altay *et al.* analyzed the influence of extracellular matrix stiffness on cell growth and structure. They found that a stiffer matrix does not allow the proliferation of cells in a 3D structure, while a softer one gives rise to organoids-like structures. Moreover, in such structures, they were able to observe a two-step process. In a first phase the cells differentiated in order to form crypts. Then, from the crypts, stem cells migrated to form villi, showing potential self-assembling properties. This was possible thanks to the softness of the matrix which allowed an easier migration of cells[133]. As above stated, the idea of having a precise and personalized medicine is the driving force of organoids experiments. As a proof of concept, Yao *et al.* took organoids from patients affected by colorectal cancer and studied the response of such model to chemoradiation comparing the results to the ones obtained from the clinical response of the patients. As a first step, they established the similarity in pathophysiology between the model and the real tumors. After that, they compared the responses to chemoradiation. The results were comparable as there were an accuracy of about 84% and a sensitivity of circa 78%[134]. Another group was able to reproduce Chron's disease by taking organoids from patients having such disease and adding cytokines to obtain the typical inflammatory state. Their work was focused on understanding the effects of corticosteroids on intestinal permeability, which is compromised in Chron's disease. Using prednisolone as the model corticosteroid, they observed a reduction in interleukins production and a restoring of barrier functions as demonstrated by a dextran permeability experiment[135].

Bacteria interaction with cells can be studied in such models. As an example, starting from pluripotent stem cells, Son *et al.* were able to produce organoids which mimicked the human intestine in both cellular diversity and structure. After that, they tried to understand host-microbiota interaction by culturing two *Lactobacilli* species using luminal microinjection. The maturity of the organoids was an important factor in viability of bacteria, with more structured organoids being more prone to allow bacteria survival. They demonstrated the possibility of using mature organoids as platforms for co-culture of bacteria. However, they studied only aerophilic bacteria, which are easier to culture as they need the same oxygen concentration as cells, but represent the smallest portion of bacteria present in the intestine[136]. Host-bacteria interaction is interesting also when talking about infections. One of the most severe infections is given by *Salmonella enterica*. Forbester *et al.* reproduced intestinal organoids from pluripotent stem cells and cultured, by microinjection, a strain of *Salmonella.* What they observed was an invasion of *Salmonella* coherent with a specific gene that, when silenced, diminished consistently its invasion capabilities[137]. Similarly, Engevik *et al.* studied the effect of *Clostridium difficile* infection on intestinal organoids. They focused specifically on mucus interaction, as this is the first barrier to overcome for bacteria in order to be invasive. Not only MUC2 production was reduced

when *Clostridium difficile* was added to the culture, but also it bound majorly to mucus taken from patients which had already a *Clostridium* infection. The diminishing of mucus can be explained as a first mechanism that bacteria have as to enhance their possibilities of attacking cells[138].

## 1.6. Gut-on-chip

As all the above-mentioned models are able to mimic one or more specific aspects and functions of the intestine, they all lack dynamic conditions. Organ-on-chips are microfluidic platforms that well mimic the *in-vivo* environment of a specific organ in order to diminish the cost of drug development, partly avoiding the use of animal testing[139]. They show functions typical of the organ they are reproducing both in healthy and diseased models[140]. Each organ-on-chip can interact with other platforms to reconstruct the interactions between tissues, with the final aim to reconstruct a body-on-chip in which a patient cells can be cultured, obtaining also personalized medicine[141].

Among them, greater interest has been given to gut-on-chip platforms that can reproduce the intestine microenvironment in terms of absorption, intestinal barrier properties, mucus production and host-bacteria interaction[142].

One of the first examples of such a device was made culturing Caco-2 cells in a double channel configuration. The cells were able to differentiate into epithelial cells forming villi-like structures when put in dynamic conditions. This was further enhanced by adding peristalsis-like motions. They demonstrated the interaction with gut flora by co-culturing *L. Rhamnosus*, which is an aerobic bacteria typical of the colon[143]. A single channel device was produced by Guo *et al.* by culturing Caco-2 cells in a dynamic environment on a planar layer and on nitrocellulose membrane. They assessed its properties by verifying tight junction formation and gene expression which were significantly enhanced in the case of nitrocellulose membrane. Two drugs were tested in such systems, a chemotherapeutic agent and a drug for high-blood pressure treatment to understand their metabolism. After 12 hours from the treatment, they analyzed the content of the supernatant. It showed a higher metabolic efficacy associated with cells cultured on the membrane for both drugs[144]. As this could be an interesting platform for drug metabolism studies, it lacks some fundamental intestinal properties such as absorption and host-bacteria interaction.

As nowadays it is well understood that Caco-2 cells differentiate and form villi structures when cultured in a dynamic environment, the influence of a static and dynamic flow rate were tested only in the latest years. This study arose from the knowledge that when cells polarize and differentiate the villi sense a different shear stress, which is higher with respect to not fully developed cells. After assessing this phenomenon by a computational fluid dynamics simulation, the group of Fois tried to tune the shear stresses during the cell growth in a simple single layer microfluidic device. They analyzed the villi and tight junctions formation, the level of mucin and gene expression. They did not find any significant difference between the classic culture with a constant flow rate and the one which takes into account the shear stress sensing, in which case the flow rate was reduced[145].

This can be useful for the reduction of medium consumption which is something that should be considered as the total growth can take up to 10 days.

Different groups performed a culture of organoids taken from patients to develop a gut-on-chip as to obtain a structural organization similar to the *in-vivo* intestine. There are few examples of protocols for the formation of 3D architectures in a microfluidic chip starting from organoids. One of such examples is given by the group of Shin. By applying shear stresses, the cells were able to proliferate and form villi-like structures, especially when starting from organoids. However, as the results seem promising, it is still difficult to obtain a crypt-villus axis that is in accordance with the *in-vivo* case, mainly due to the short height in which cells can proliferate in the organ-on-chip[146]. A work which has taken advantage of organoids to study intestinal environment has been performed by Kasendra *et al.* They took organoids from healthy donors in a double channel device. In one channel there were the organoids, whereas in the other one, separated by a porous membrane from the first one, they cultured micro-vascularized endothelial cells. By applying shear stresses given by fluid passage and cyclic deformation they were able to produce villi formation with a good approximation of intestinal characteristics as confirmed by transcriptomic analysis[147].

As explained in the previous paragraph, organoids are implemented also to study intestinal diseases. In order to study inflammatory bowel disease, Beaurivage *et al.* cultured epithelial cells obtained from organoids together with macrophages in a gut-on-chip. After recreating a healthy colon, they activated inflammation by using LPS and a cytokine associated with microbial invasion and enhancement of intestinal permeability. The inflammation status was confirmed by both interleukin analysis and pathway regulation given by transcriptomics. To demonstrate the model, they added TPCA-1, an anti-inflammatory drug. As a result, interleukin level decreased significantly along with an increasing of cell viability with respect to the inflamed case[148]. Shin *et al.* took organoids from patients with ulcerative colitis, Chron's disease or colorectal cancer and cultured in a double chamber device with vacuum chamber to simulate peristalsis. In this way they were able to reproduce the most common diseases of the colon, posing the bases for a precise medicine platform. The model was further complicated by adding fecal microbiota observing, after 48 hours, a colonization of bacteria in the intestinal folds, no change in barrier integrity and a good bacteria viability[149]. Apostolou *et al.* took organoids from colonic biopsies and put them in a double channel organ-on-chip. RNA sequencing demonstrated the similarities between this model and human intestine. As a proof of concept, they cultured organoids taken from different patients and analyzed the effects of interferon-γ. Permeability enhanced upon treatment together with a change in actin structure, revealing tight junctions modification and squamous cells formation[150]. In order to study inflammatory bowel disease, Marr *et al.* expanded stem cells obtained from human biopsies in a double channel microfluidic device. The epithelia barrier was inflamed by using cytokines. Analyzing TEER, they saw a decrease in barrier integrity after 24 hours of treatment which was further demonstrated by different molecular weight dextran permeability assay. Differently from results from HT29 2D culture, they observed a decrease in interleukin-8 after inflammation[151]. This further demonstrates the need of using dynamic, simil-3D cultures in spite of classic 2D ones.

If it is true that organoids represent a step towards a more real approximation of the *in-vivo* conditions in cell culture field, it should also be considered that drug studies are complicated to perform using them because of their enclosed lumen. Furthermore, bacteria are difficult to be added with respect to classical gut-on-chip which have a precise apical side. In fact, they are usually added by microinjection in such a configuration[152].

A drug test on the gut-on-chip was made by Kulthong *et al.* They compared a Transwell® culture with a dynamic one, finding no appreciable differences in term of apparent permeability, especially for low molecular weight compounds. The major difference between the two models is the possibility to follow online the passage of the compound and the smaller times of culture needed to have an adequate epithelial barrier[153].

Regarding inflammatory studies, Gijzen *et al.* proposed a platform where different epithelial cells were cultured, i.e., Caco-2 and HT29-MTX cell lines, along with immune cells. The inflammation was performed by exposing the cells to TNF-α. The levels of inflammation, quantified by epithelial barrier resistance and proinflammatory cytokines secretion, decreased when the cells were treated with TPCA-1. The platform consisted of forty microfluidic chips and cells were cultured in gel matrices[154].

Regarding host-bacteria interactions, there are few works that were able to establish an adequate co-culture of strictly anaerobic bacteria with intestinal cells. HuMiX platform is one of the most promising in this field (**Fig. 1.6 A**). It consists of a perfusion chamber, a cell culture chamber and a microbial culture chamber, each of them separated by a semiporous membrane. Even if the bacteria viability was preserved, the separation between cell and microbial chambers does not allow a full understanding of host-microbiome interaction. In fact, it adds a further barrier to the bacteria metabolites which are readily available for cells in *in-vivo* conditions[155]. A work where there was a real interaction between bacteria and intestine cells was performed by Jalili-Firoozinezhad *et al.* They took bacteria from feces and cultured them in anaerobic conditions, obtaining high microbial diversity. The chip was composed of two channels separated by a semiporous membrane where cells and bacteria were cultured in the same channel (**Fig. 1.6 B**). Oxygen sensors were added to effectively demonstrate the low oxygen concentration[156].

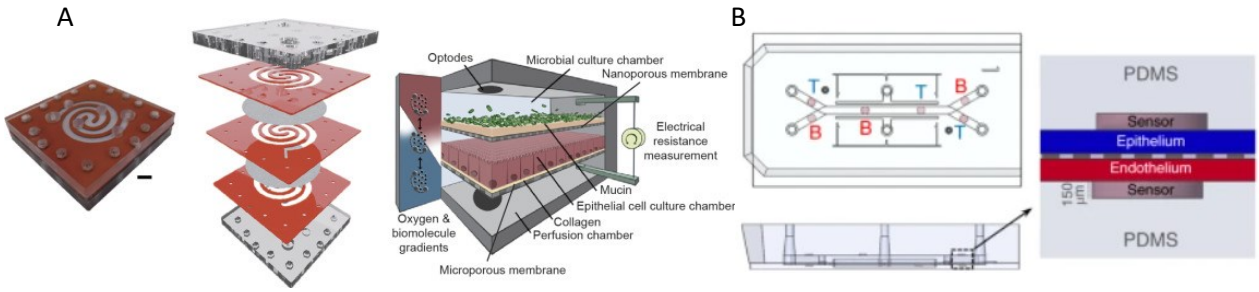


**Figure 1.4.** HuMix platform. Assembled and schematic illustration. Scale bar is 1 cm (A)[155]. Schematic illustration of double channel intestine-chip with oxygen sensors embedded for top and bottom channels (B)[156].

The gut-on-chips mentioned above are all promising platforms for mucus layer and villi formation, drug metabolism, inflammation studies and host-bacteria interactions. However, none of these works have put all these properties and analysis together, as it will be shown in the next chapters.

## 1.7. Aim of the Thesis

The aim of this thesis is to develop a strategy to reduce the insurgence of obesity and to treat its main comorbidities. Analyzing the state of art, we found that the principal comorbidities of obesity are the chronic inflamed status; the dysbiosis in gut microflora towards *Firmicutes* bacteria with respect to *Bacteroidetes*; the enhanced absorption of nutrients and calories. In literature, there are few strategies involving a restoration of the gut microflora balance, using either probiotics or prebiotics or a mixture of both. They saw that a body weight loss was associated with a healthier gut microbiota. This moved us to find the main *Firmicutes* bacteria involved in nutrient absorption and polysaccharide degradation. Such bacteria was found to be *Ruminoccocus Bromii* as it is a keystone bacteria in starch degradation and as its metabolites are used by other *Firmicutes* to grow. However, this species is present in a smaller percentage in healthy patients too. For this reason, along with the possible insurgence of multiresistant drug bacteria, we avoided the usage of antibiotics.

The strategy involved the use of oil as it is associated with an increased satiety feeling. The oil core was coated with a starch shell as this protects the oil from the harsh GIT conditions, till the colon where the bacteria starts degrading it. While degrading the starch, part of the bacteria will be entrapped in it and part of the oil will be released on the epithelium, liberating the curcumin, which has an anti-inflammatory effect, and thickening the barrier with a consequent reduction of intestinal absorption.

Obesity is difficult to be reproduced in an *in-vitro* situation, as factors associated with it, like body weight and hormones, cannot be mimicked. Anyway, as one main objective of this thesis we successfully developed a user friendly “gut on chip device” able to reproduce the main aspects of obesity *in-vitro*, such as inflammation, nutrient absorption and host-bacteria interaction.

Briefly, in **Chapter 2** we showed the development of the microcarrier, in the shape of an oil-in-water Pickering emulsion made with starch and loaded with curcumin. Along with this, we studied the growth of *R. Bromii* in standard anaerobic conditions and its interaction with the microcarrier. *L. Rhamnosus* was used as a negative control as it does not degrade starch.

In **Chapter 3** the development of a microfluidic device able to reproduce the principal features of the intestine was assessed. Furthermore, the chip allowed the co-culture of different bacteria species, anaerobic and microaerophilic, in the same channel of the cells as to preserve the host-bacteria interaction.

In **Chapter 4** a proof of concept of our strategy and the validation of the gut-on-chip were studied. In particular, inflammation was mimicked to observe the action of the curcumin-loaded oil core of the starch emulsion in presence and absence of *R. Bromii*. Additionally, the absorption of nutrients, in the shape of 3 kDa fluorescent dextran, was assessed before and after the addition of the starch macroemulsion.

In **Chapter 5** the future perspective and the conclusions of the work were discussed, focusing on its relevance with respect to the literature in treating obesity.

Finally, **Chapter 6** elucidated some of the side-works including a gradient-generator used as a gut-on-chip to study the propulsion of alginate microrobots and the development, scalability and GIT testing of nanoemulsions loaded with nutraceuticals to improve their bioavailability.

In conclusion, we proposed a novel strategy to treat the main issues involved in obesity that takes into account a stable microcarrier that has an action associated with the presence of adverse gut bacteria. Naturally, *in-vivo* test are essential as other features typical of obese subjects cannot be studied in an *in-vitro* environment.

## 1.8. Bibliography


1. Collins, J. T., Nguyen, A. & Badireddy, M. Anatomy, Abdomen and Pelvis, Small Intestine. in *StatPearls* (StatPearls Publishing, 2023).

2. *Colon: Structure and Function*. (Springer US, 1983). doi:10.1007/978-1-4757-0307-8.

3. Britannica, The Editors of Encyclopaedia. 'large intestine'. Encyclopedia Britannica, 23 Aug. 2023, https://www.britannica.com/science/large-intestine.

4. Huang, X. *et al.* Modulation of Mucin (MUC2, MUC5AC and MUC5B) mRNA Expression and Protein Production and Secretion in Caco-2/HT29-MTX Co-Cultures Following Exposure to Individual and Combined Aflatoxin M1 and Ochratoxin A. *Toxins* **11**, 132 (2019).

5. Johansson, M. E. V., Larsson, J. M. H. & Hansson, G. C. The two mucus layers of colon are organized by the MUC2 mucin, whereas the outer layer is a legislator of host–microbial interactions. *Proc. Natl. Acad. Sci.* **108**, 4659–4665 (2011).

6. Ruppin, H., Bar-Meir, S., Soergel, K. H., Wood, C. M. & Schmitt, M. G. Absorption of Short-Chain Fatty Acids by the Colon. *Gastroenterology* **78**, 1500–1507 (1980).

7. Duca, F. A., Waise, T. M. Z., Peppler, W. T. & Lam, T. K. T. The metabolic impact of small intestinal nutrient sensing. *Nat. Commun.* **12**, 903 (2021).

8. Meldrum, D. R., Morris, M. A. & Gambone, J. C. Obesity pandemic: causes, consequences, and solutions—but do we have the will? *Fertil. Steril.* **107**, 833–839 (2017).

9. Ward, Z. J. *et al.* Excess mortality associated with elevated body weight in the USA by state and demographic subgroup: A modelling study. *eClinicalMedicine* **48**, 101429 (2022).

10. Tarasiuk, A., Mosińska, P. & Fichna, J. The mechanisms linking obesity to colon cancer: An overview. *Obes. Res. Clin. Pract.* **12**, 251–259 (2018).

11. Bardou, M., Barkun, A. N. & Martel, M. Obesity and colorectal cancer. *Gut* **62**, 933–947 (2013).

12. Spagnuolo, M. I. *et al.* Relationship between severe obesity and gut inflammation in children: what's next? *Ital. J. Pediatr.* **36**, 66 (2010).

13. Pendyala, S., Neff, L. M., Suárez-Fariñas, M. & Holt, P. R. Diet-induced weight loss reduces colorectal inflammation: implications for colorectal carcinogenesis. *Am. J. Clin. Nutr.* **93**, 234–242 (2011).

14. Brun, P. *et al.* Increased intestinal permeability in obese mice: new evidence in the pathogenesis of nonalcoholic steatohepatitis. *Am. J. Physiol.-Gastrointest. Liver Physiol.* **292**, G518–G525 (2007).

15. Dailey, M. J. Nutrient-induced intestinal adaption and its effect in obesity. *Physiol. Behav.* **136**, 74–78 (2014).

16. Elias, K., Webb, D.-L., Diaz Tartera, H. O., Hellström, P. M. & Sundbom, M. Impact of biliopancreatic diversion with duodenal switch on glucose homeostasis and gut hormones and their correlations with appetite. *Surg. Obes. Relat. Dis.* **18**, 1392–1398 (2022).

17. Lutz, T. A. & Bueter, M. The physiology underlying Roux-en-Y gastric bypass: a status report. *Am. J. Physiol.-Regul. Integr. Comp. Physiol.* **307**, R1275–R1291 (2014).

18. Blachar, A., Federle, M. P., Pealer, K. M., Ikramuddin, S. & Schauer, P. R. Gastrointestinal Complications of Laparoscopic Roux-en-Y Gastric Bypass Surgery: Clinical and Imaging Findings. *Radiology* **223**, 625–632 (2002).

19. Bruschi Kelles, S. M., Diniz, M. F. H. S., Machado, C. J. & Barreto, S. M. Mortality rate after open Roux-in-Y gastric bypass: a 10-year follow-up. *Braz. J. Med. Biol. Res.* **47**, 617–625 (2014).

20. Lombardo, M. *et al.* Long-Term Iron and Vitamin B12 Deficiency Are Present after Bariatric Surgery, despite the Widespread Use of Supplements. *Int. J. Environ. Res. Public. Health* **18**, 4541 (2021).

21. Cresci, G. A. M. & Izzo, K. Gut Microbiome. in *Adult Short Bowel Syndrome* 45–54 (Elsevier, 2019). doi:10.1016/B978-0-12-814330-8.00004-4.

22. Sonnenburg, J. L. & Bäckhed, F. Diet–microbiota interactions as moderators of human metabolism. *Nature* **535**, 56–64 (2016).

23. Aagaard, K. *et al.* The Placenta Harbors a Unique Microbiome. *Sci. Transl. Med.* **6**, (2014).

24. Adlerberth, I. & Wold, A. Establishment of the gut microbiota in Western infants: Establishment of the gut microbiota in Western infants. *Acta Paediatr.* **98**, 229–238 (2009).

25. Hasan, N. & Yang, H. Factors affecting the composition of the gut microbiota, and its modulation. *PeerJ* **7**, e7502 (2019).

26. Gomaa, E. Z. Human gut microbiota/microbiome in health and diseases: a review. *Antonie Van Leeuwenhoek* **113**, 2019–2040 (2020).

27. Harmsen, H. J. M. & De Goffau, Marcus. C. The Human Gut Microbiota. in *Microbiota of the Human Body* (ed. Schwiertz, A.) vol. 902 95–108 (Springer International Publishing, 2016).

28. Weinroth, M. D. *et al.* Considerations and best practices in animal science 16S ribosomal RNA gene sequencing microbiome studies. *J. Anim. Sci.* **100**, skab346 (2022).

29. Rowland, I. *et al.* Gut microbiota functions: metabolism of nutrients and other food components. *Eur. J. Nutr.* **57**, 1–24 (2018).

30. Earle, K. A. *et al.* Quantitative Imaging of Gut Microbiota Spatial Organization. *Cell Host Microbe* **18**, 478–488 (2015).

31. Nava, G. M., Friedrichsen, H. J. & Stappenbeck, T. S. Spatial organization of intestinal microbiota in the mouse ascending colon. *ISME J.* **5**, 627–638 (2011).

32. Mark Welch, J. L., Hasegawa, Y., McNulty, N. P., Gordon, J. I. & Borisy, G. G. Spatial organization of a model 15-member human gut microbiota established in gnotobiotic mice. *Proc. Natl. Acad. Sci.* **114**, (2017).

33. Duranti, S., Ferrario, C., van Sinderen, D., Ventura, M. & Turroni, F. Obesity and microbiota: an example of an intricate relationship. *Genes Nutr.* **12**, 18 (2017).

34. Stephens, R. W., Arhire, L. & Covasa, M. Gut Microbiota: From Microorganisms to Metabolic Organ Influencing Obesity: Microbiota and Weight Gain. *Obesity* **26**, 801–809 (2018).

35. Meijnikman, A. S. *et al.* Distinct differences in gut microbial composition and functional potential from lean to morbidly obese subjects. *J. Intern. Med.* **288**, 699–710 (2020).

36. Tremaroli, V. & Bäckhed, F. Functional interactions between the gut microbiota and host metabolism. *Nature* **489**, 242–249 (2012).

37. May, K. S. & Den Hartigh, L. J. Modulation of Adipocyte Metabolism by Microbial Short-Chain Fatty Acids. *Nutrients* **13**, 3666 (2021).

38. Martín, R., Bermúdez-Humarán, L. G. & Langella, P. Gnotobiotic Rodents: An In Vivo Model for the Study of Microbe–Microbe Interactions. *Front. Microbiol.* **7**, (2016).

39. Backhed, F. *et al.* The gut microbiota as an environmental factor that regulates fat storage. *Proc. Natl. Acad. Sci.* **101**, 15718–15723 (2004).

40. Bäckhed, F., Manchester, J. K., Semenkovich, C. F. & Gordon, J. I. Mechanisms underlying the resistance to diet-induced obesity in germ-free mice. *Proc. Natl. Acad. Sci.* **104**, 979–984 (2007).

41. Ley, R. E. *et al.* Obesity alters gut microbial ecology. *Proc. Natl. Acad. Sci.* **102**, 11070–11075 (2005).

42. Vindigni, S. M. & Surawicz, C. M. Fecal Microbiota Transplantation. *Gastroenterol. Clin. North Am.* **46**, 171–185 (2017).

43. Turnbaugh, P. J. *et al.* An obesity-associated gut microbiome with increased capacity for energy harvest. *Nature* **444**, 1027–1031 (2006).

44. Lai, Z.-L. *et al.* Fecal microbiota transplantation confers beneficial metabolic effects of diet and exercise on diet-induced obese mice. *Sci. Rep.* **8**, 15625 (2018).

45. Allegretti, J. R. *et al.* Effects of Fecal Microbiota Transplantation With Oral Capsules in Obese Patients. *Clin. Gastroenterol. Hepatol.* **18**, 855-863.e2 (2020).

46. Yu, E. W. *et al.* Fecal microbiota transplantation for the improvement of metabolism in obesity: The FMT-TRIM double-blind placebo-controlled pilot trial. *PLOS Med.* **17**, e1003051 (2020).

47. Jung, S.-P. *et al.* Effect of *Lactobacillus gasseri* BNR17 on Overweight and Obese Adults: A Randomized, Double-Blind Clinical Trial. *Korean J. Fam. Med.* **34**, 80 (2013).

48. Yang, F. *et al.* Beneficial effects of a combination of Clostridium cochlearium and Lactobacillus acidophilus on body weight gain, insulin sensitivity, and gut microbiota in high-fat diet–induced obese mice. *Nutrition* **93**, 111439 (2022).

49. Nagata, S., Chiba, Y., Wang, C. & Yamashiro, Y. The effects of the *Lactobacillus casei* strain on obesity in children: a pilot study. *Benef. Microbes* **8**, 535–543 (2017).

50. Burakova, I. *et al.* The Effect of Short-Term Consumption of Lactic Acid Bacteria on the Gut Microbiota in Obese People. *Nutrients* **14**, 3384 (2022).

51. Linninge, C., Xu, J., Bahl, M. I., Ahrné, S. & Molin, G. *Lactobacillus fermentum* and *Lactobacillus plantarum* increased gut microbiota diversity and functionality, and mitigated *Enterobacteriaceae* , in a mouse model. *Benef. Microbes* **10**, 413–424 (2019).

52. Nicolucci, A. C. *et al.* Prebiotics Reduce Body Fat and Alter Intestinal Microbiota in Children Who Are Overweight or With Obesity. *Gastroenterology* **153**, 711–722 (2017).

53. Reimer, R. A. *et al.* Inulin-type fructans and whey protein both modulate appetite but only fructans alter gut microbiota in adults with overweight/obesity: A randomized controlled trial. *Mol. Nutr. Food Res.* **61**, 1700484 (2017).

54. Rawi, M. H., Abdullah, A., Ismail, A. & Sarbini, S. R. Manipulation of Gut Microbiota Using Acacia Gum Polysaccharide. *ACS Omega* **6**, 17782–17797 (2021).

55. Alvarado-Jasso, G. M. *et al.* Prebiotic effects of a mixture of agavins and green banana flour in a mouse model of obesity. *J. Funct. Foods* **64**, 103685 (2020).

56. Champ, M. Resistant starch. in *Starch in Food* 560–574 (Elsevier, 2004). doi:10.1533/9781855739093.4.560.

57. Liang, D., Li, N., Dai, X., Zhang, H. & Hu, H. Effects of different types of potato resistant starches on intestinal microbiota and short-chain fatty acids under *in vitro* fermentation. *Int. J. Food Sci. Technol.* **56**, 2432–2442 (2021).

58. Wang, Y. *et al.* Effects of the resistant starch on glucose, insulin, insulin resistance, and lipid parameters in overweight or obese adults: a systematic review and meta-analysis. *Nutr. Diabetes* **9**, 19 (2019).

59. Thompson, M. S. *et al.* An in vivo study: Prebiotic evaluation of the resistant Starch from Metroxylon sagu on obesity using fat-induced rats. *Bioact. Carbohydr. Diet. Fibre* **30**, 100365 (2023).

60. Fu, J., Wang, Y., Tan, S. & Wang, J. Effects of Banana Resistant Starch on the Biochemical Indexes and Intestinal Flora of Obese Rats Induced by a High-Fat Diet and Their Correlation Analysis. *Front. Bioeng. Biotechnol.* **9**, 575724 (2021).

61. Thiennimitr, P. *et al.* Lactobacillus paracasei HII01, xylooligosaccharides, and synbiotics reduce gut disturbance in obese rats. *Nutrition* **54**, 40–47 (2018).

62. Stojanov, S., Berlec, A. & Štrukelj, B. The Influence of Probiotics on the Firmicutes/Bacteroidetes Ratio in the Treatment of Obesity and Inflammatory Bowel disease. *Microorganisms* **8**, 1715 (2020).

63. Ng, S. C. *et al.* Microbiota engraftment after faecal microbiota transplantation in obese subjects with type 2 diabetes: a 24-week, double-blind, randomised controlled trial. *Gut* **71**, 716–723 (2022).

64. Ze, X., Duncan, S. H., Louis, P. & Flint, H. J. Ruminococcus bromii is a keystone species for the degradation of resistant starch in the human colon. *ISME J.* **6**, 1535–1543 (2012).

65. Ze, X. *et al.* Unique Organization of Extracellular Amylases into Amylosomes in the Resistant Starch-Utilizing Human Colonic Firmicutes Bacterium Ruminococcus bromii. *mBio* **6**, e01058-15 (2015).

66. Mukhopadhya, I. *et al.* Sporulation capability and amylosome conservation among diverse human colonic and rumen isolates of the keystone starch-degrader *Ruminococcus bromii*: Comparative genomics of *Ruminococcus bromii*. *Environ. Microbiol.* **20**, 324–336 (2018).

67. Crost, E. H. *et al.* Mechanistic Insights Into the Cross-Feeding of Ruminococcus gnavus and Ruminococcus bromii on Host and Dietary Carbohydrates. *Front. Microbiol.* **9**, 2558 (2018).

68. Maljaars, P. W. J., Peters, H. P. F., Mela, D. J. & Masclee, A. A. M. Ileal brake: A sensible food target for appetite control. A review. *Physiol. Behav.* **95**, 271–281 (2008).

69. Maljaars, P. W. J. *et al.* Effect of ileal fat perfusion on satiety and hormone release in healthy volunteers. *Int. J. Obes.* **32**, 1633–1639 (2008).

70. Beglinger, C. & Degen, L. Fat in the intestine as a regulator of appetite—role of CCK. *Physiol. Behav.* **83**, 617–621 (2004).

71. Maljaars, J., Romeyn, E. A., Haddeman, E., Peters, H. P. & Masclee, A. A. Effect of fat saturation on satiety, hormone release, and food intake. *Am. J. Clin. Nutr.* **89**, 1019–1024 (2009).

72. Prater, M. C., Scheurell, A. R., Paton, C. M. & Cooper, J. A. Hunger and satiety responses to diets enriched with cottonseed oil vs. olive oil. *Physiol. Behav.* **259**, 114041 (2023).

73. Jurgoński, A., Juśkiewicz, J. & Zduńczyk, Z. A High-Fat Diet Differentially Affects the Gut Metabolism and Blood Lipids of Rats Depending on the Type of Dietary Fat and Carbohydrate. *Nutrients* **6**, 616–626 (2014).

74. Maljaars, P. W. J. *et al.* The effect of lipid droplet size on satiety and peptide secretion is intestinal site-specific. *Clin. Nutr.* **31**, 535–542 (2012).

75. Velasquez, M. T. & Bhathena, S. J. Role of Dietary Soy Protein in Obesity. *Int. J. Med. Sci.* 72–82 (2007) doi:10.7150/ijms.4.72.

76. Segura Munoz, R. R. *et al.* Stearidonic-Enriched Soybean Oil Modulates Obesity, Glucose Metabolism, and Fatty Acid Profiles Independently of *Akkermansia muciniphila*. *Mol. Nutr. Food Res.* **64**, 2000162 (2020).

77. Homayun, B., Lin, X. & Choi, H.-J. Challenges and Recent Progress in Oral Drug Delivery Systems for Biopharmaceuticals. *Pharmaceutics* **11**, 129 (2019).

78. Bouguénec, C. L. Adhesins and invasins of pathogenic Escherichia coli. *Int. J. Med. Microbiol.* **295**, 471–478 (2005).

79. Avci, F. Y. & Kasper, D. L. How Bacterial Carbohydrates Influence the Adaptive Immune System. *Annu. Rev. Immunol.* **28**, 107–130 (2010).

80. Angsantikul, P. *et al.* Coating Nanoparticles with Gastric Epithelial Cell Membrane for Targeted Antibiotic Delivery against *Helicobacter pylori* Infection. *Adv. Ther.* **1**, 1800016 (2018).

81. Yaman, S., Chintapula, U., Rodriguez, E., Ramachandramoorthy, H. & Nguyen, K. T. Cell-mediated and cell membrane-coated nanoparticles for drug delivery and cancer therapy. *Cancer Drug Resist.* (2020) doi:10.20517/cdr.2020.55.

82. Capeletti, L. B. *et al.* Gram-Negative Bacteria Targeting Mediated by Carbohydrate–Carbohydrate Interactions Induced by Surface-Modified Nanoparticles. *Adv. Funct. Mater.* **29**, 1904216 (2019).

83. Mu, H. *et al.* Pathogen-targeting glycovesicles as a therapy for salmonellosis. *Nat. Commun.* **10**, 4039 (2019).

84. Hussain, S. *et al.* Antibiotic-loaded nanoparticles targeted to the site of infection enhance antibacterial efficacy. *Nat. Biomed. Eng.* **2**, 95–103 (2018).

85. Anal, A. K., Stevens, W. F. & Remuñán-López, C. Ionotropic cross-linked chitosan microspheres for controlled release of ampicillin. *Int. J. Pharm.* **312**, 166–173 (2006).

86. Lee, T. & Chang, Y. H. Structural, physicochemical, and in-vitro release properties of hydrogel beads produced by oligochitosan and de-esterified pectin from yuzu (Citrus junos) peel as a quercetin delivery system for colon target. *Food Hydrocoll.* **108**, 106086 (2020).

87. Yang, M. *et al.* An oral pH-activated "nano-bomb" carrier combined with berberine by regulating gene silencing and gut microbiota for site-specific treatment of ulcerative colitis. *Biomater. Sci.* **10**, 1053–1067 (2022).

88. Mandracchia, D. *et al.* pH-sensitive inulin-based nanomicelles for intestinal site-specific and controlled release of celecoxib. *Carbohydr. Polym.* **181**, 570–578 (2018).

89. Shivhare, K. *et al.* Enzyme sensitive smart inulin-dehydropeptide conjugate self-assembles into nanostructures useful for targeted delivery of ornidazole. *Int. J. Biol. Macromol.* **106**, 775–783 (2018).

90. Xu, W. *et al.* Stability, microstructural and rheological properties of complex prebiotic emulsion stabilized by sodium caseinate with inulin and konjac glucomannan. *Food Hydrocoll.* **105**, 105772 (2020).

91. Mei, L. *et al.* Novel Intestinal-Targeted Ca-Alginate-Based Carrier for pH-Responsive Protection and Release of Lactic Acid Bacteria. *ACS Appl. Mater. Interfaces* **6**, 5962–5970 (2014).

92. Apriyanto, A., Compart, J. & Fettke, J. A review of starch, a unique biopolymer – Structure, metabolism and in planta modifications. *Plant Sci.* **318**, 111223 (2022).

93. Magallanes-Cruz, P. A., Flores-Silva, P. C. & Bello-Perez, L. A. Starch Structure Influences Its Digestibility: A Review: Structure-digestibility relationship…. *J. Food Sci.* **82**, 2016–2023 (2017).

94. Chen, L. *et al.* Resistant starch as a carrier for oral colon-targeting drug matrix system. *J. Mater. Sci. Mater. Med.* **18**, 2199–2203 (2007).

95. Jiang, M. *et al.* Preparation of a starch-based carrier for oral delivery of Vitamin E to the small intestine. *Food Hydrocoll.* **91**, 26–33 (2019).

96. Zhao, B. *et al.* Polysaccharide-coated porous starch-based oral carrier for paclitaxel: Adsorption and sustained release in colon. *Carbohydr. Polym.* **291**, 119571 (2022).

97. Zhao, B. *et al.* Colon targeted releases and uptakes of paclitaxel loaded in modified porous starch. *Carbohydr. Polym.* **318**, 121126 (2023).

98. Surini, S., Anggriani, V. & Anwar, E. Study of Mucoadhesive Microspheres Based on Pregelatinized Cassava Starch Succinate as a New Carrier for Drug Delivery. *J. Med. Sci.* **9**, 249–256 (2009).

99. Kimura-Todani, T. *et al.* Dietary delivery of acetate to the colon using acylated starches as a carrier exerts anxiolytic effects in mice. *Physiol. Behav.* **223**, 113004 (2020).

100. Situ, W., Li, X., Liu, J. & Chen, L. Preparation and Characterization of Glycoprotein-Resistant Starch Complex As a Coating Material for Oral Bioadhesive Microparticles for Colon-Targeted Polypeptide Delivery. *J. Agric. Food Chem.* **63**, 4138–4147 (2015).

101. Putro, J. N., Ismadji, S., Gunarto, C., Soetaredjo, F. E. & Ju, Y. H. A study of anionic, cationic, and nonionic surfactants modified starch nanoparticles for hydrophobic drug loading and release. *J. Mol. Liq.* **298**, 112034 (2020).

102. Khan, A. *et al.* Development of Resistant Starch Film Coated Microparticles for an Oral Colon-Specific Drug Delivery. *Starch - Stärke* **72**, 1900262 (2020).

103. Ashwar, B. A., Gani, A., Gani, A., Shah, A. & Masoodi, F. A. Production of RS4 from rice starch and its utilization as an encapsulating agent for targeted delivery of probiotics. *Food Chem.* **239**, 287–294 (2018).

104. Pulido-Moran, M., Moreno-Fernandez, J., Ramirez-Tortosa, C. & Ramirez-Tortosa, Mc. Curcumin and Health. *Molecules* **21**, 264 (2016).

105. Burge, K., Gunasekaran, A., Eckert, J. & Chaaban, H. Curcumin and Intestinal Inflammatory Diseases: Molecular Mechanisms of Protection. *Int. J. Mol. Sci.* **20**, 1912 (2019).

106. Bianconi, V. *et al.* The Multifaceted Actions of Curcumin in Obesity. in *Natural Products and Human Diseases* (eds. Sahebkar, A. & Sathyapalan, T.) vol. 1328 81–97 (Springer International Publishing, 2021).

107. Hales, D. *et al.* Curcumin-Loaded Microspheres Are Effective in Preventing Oxidative Stress and Intestinal Inflammatory Abnormalities in Experimental Ulcerative Colitis in Rats. *Molecules* **27**, 5680 (2022).

108. Chen, S. *et al.* Nano-micelles based on hydroxyethyl starch-curcumin conjugates for improved stability, antioxidant and anticancer activity of curcumin. *Carbohydr. Polym.* **228**, 115398 (2020).

109. Xu, C. *et al.* Colon-targeted oral nanoparticles based on ROS-scavenging hydroxyethyl starch-curcumin conjugates for efficient inflammatory bowel disease therapy. *Int. J. Pharm.* **623**, 121884 (2022).

110. Ahmad, M. Z. *et al. In vitro* and *in vivo* evaluation of *Assam Bora* rice starch-based bioadhesive microsphere as a drug carrier for colon targeting. *Expert Opin. Drug Deliv.* **9**, 141–149 (2012).

111. Acevedo-Guevara, L., Nieto-Suaza, L., Sanchez, L. T., Pinzon, M. I. & Villa, C. C. Development of native and modified banana starch nanoparticles as vehicles for curcumin. *Int. J. Biol. Macromol.* **111**, 498–504 (2018).

112. Salah, N., Dubuquoy, L., Carpentier, R. & Betbeder, D. Starch nanoparticles improve curcumin-induced production of anti-inflammatory cytokines in intestinal epithelial cells. *Int. J. Pharm. X* **4**, 100114 (2022).

113. Kasprzak, M. M., Macnaughtan, W., Harding, S., Wilde, P. & Wolf, B. Stabilisation of oil-in-water emulsions with non-chemical modified gelatinised starch. *Food Hydrocoll.* **81**, 409–418 (2018).

114. Lu, X., Li, C. & Huang, Q. Combining in vitro digestion model with cell culture model: Assessment of encapsulation and delivery of curcumin in milled starch particle stabilized Pickering emulsions. *Int. J. Biol. Macromol.* **139**, 917–924 (2019).

115. Sambuy, Y. *et al.* The Caco-2 cell line as a model of the intestinal barrier: influence of cell and culture-related factors on Caco-2 cell functional characteristics. *Cell Biol. Toxicol.* **21**, 1–26 (2005).

116. Yeste, J., Illa, X., Alvarez, M. & Villa, R. Engineering and monitoring cellular barrier models. *J. Biol. Eng.* **12**, 18 (2018).

117. Felix, K., Tobias, S., Jan, H., Nicolas, S. & Michael, M. Measurements of transepithelial electrical resistance (TEER) are affected by junctional length in immature epithelial monolayers. *Histochem. Cell Biol.* (2021) doi:10.1007/s00418-021-02026-4.

118. Langella, A. *et al.* In vitro study of intestinal epithelial interaction with engineered oil in water nanoemulsions conveying curcumin. *Colloids Surf. B Biointerfaces* **164**, 232–239 (2018).

119. Denaro, M. *et al.* In vitro intestinal transport and anti-inflammatory properties of ideain across Caco-2 transwell model. *Fitoterapia* **146**, 104723 (2020).

120. Parajuli, P., Gokulan, K. & Khare, S. Preclinical In Vitro Model to Assess the Changes in Permeability and Cytotoxicity of Polarized Intestinal Epithelial Cells during Exposure Mimicking Oral or Intravenous Routes: An Example of Arsenite Exposure. *Int. J. Mol. Sci.* **23**, 4851 (2022).

121. Chalubinski, M., Wojdan, K., Gorzelak, P., Borowiec, M. & Broncel, M. The effect of oxidized cholesterol on barrier functions and IL-10 mRNA expression in human intestinal epithelium co-cultured with dendritic cells in the transwell system. *Food Chem. Toxicol.* **69**, 289–293 (2014).

122. Cohen, E., Ophir, I. & Shaul, Y. B. Induced differentiation in HT29, a human colon adenocarcinoma cell line. *J. Cell Sci.* **112**, 2657–2666 (1999).

123. Mahler, G. J., Shuler, M. L. & Glahn, R. P. Characterization of Caco-2 and HT29-MTX cocultures in an in vitro digestion/cell culture model used to predict iron bioavailability☆. *J. Nutr. Biochem.* **20**, 494–502 (2009).

124. Béduneau, A. *et al.* A tunable Caco-2/HT29-MTX co-culture model mimicking variable permeabilities of the human intestine obtained by an original seeding procedure. *Eur. J. Pharm. Biopharm.* **87**, 290–298 (2014).

125. Antunes, F., Andrade, F., Araújo, F., Ferreira, D. & Sarmento, B. Establishment of a triple co-culture in vitro cell models to study intestinal absorption of peptide drugs. *Eur. J. Pharm. Biopharm.* **83**, 427–435 (2013).

126. Leonard, F., Collnot, E.-M. & Lehr, C.-M. A Three-Dimensional Coculture of Enterocytes, Monocytes and Dendritic Cells To Model Inflamed Intestinal Mucosa in Vitro. *Mol. Pharm.* **7**, 2103–2119 (2010).

127. Zhang, J. *et al.* Coculture of primary human colon monolayer with human gut bacteria. *Nat. Protoc.* **16**, 3874–3900 (2021).

128. Mohebali, N., Ekat, K., Kreikemeyer, B. & Breitrück, A. Barrier Protection and Recovery Effects of Gut Commensal Bacteria on Differentiated Intestinal Epithelial Cells In Vitro. *Nutrients* **12**, 2251 (2020).

129. Cai, Y. *et al.* Development, validation, and application of a novel 7-day Caco-2 cell culture system. *J. Pharmacol. Toxicol. Methods* **70**, 175–181 (2014).

130. Yang, S. *et al.* Organoids: The current status and biomedical applications. *MedComm* **4**, e274 (2023).

131. Sato, T. *et al.* Long-term Expansion of Epithelial Organoids From Human Colon, Adenoma, Adenocarcinoma, and Barrett's Epithelium. *Gastroenterology* **141**, 1762–1772 (2011).

132. Rodrigues, D. *et al.* Unravelling Mechanisms of Doxorubicin-Induced Toxicity in 3D Human Intestinal Organoids. *Int. J. Mol. Sci.* **23**, 1286 (2022).

133. Altay, G. *et al.* Self-organized intestinal epithelial monolayers in crypt and villus-like domains show effective barrier function. *Sci. Rep.* **9**, 10140 (2019).

134. Yao, Y. *et al.* Patient-Derived Organoids Predict Chemoradiation Responses of Locally Advanced Rectal Cancer. *Cell Stem Cell* **26**, 17-26.e6 (2020).

135. Xu, P., Elizalde, M., Masclee, A., Pierik, M. & Jonkers, D. Corticosteroid enhances epithelial barrier function in intestinal organoids derived from patients with Crohn's disease. *J. Mol. Med.* **99**, 805–815 (2021).

136. Son, Y. S. *et al.* Maturation of human intestinal organoids in vitro facilitates colonization by commensal lactobacilli by reinforcing the mucus layer. *FASEB J.* **34**, 9899–9910 (2020).

137. Forbester, J. L. *et al.* Interaction of Salmonella enterica Serovar Typhimurium with Intestinal Organoids Derived from Human Induced Pluripotent Stem Cells. *Infect. Immun.* **83**, 2926–2934 (2015).

138. Engevik, M. A. *et al.* Human *Clostridium difficile* infection: altered mucus production and composition. *Am. J. Physiol.-Gastrointest. Liver Physiol.* **308**, G510–G524 (2015).

139. Leung, C. M. *et al.* A guide to the organ-on-a-chip. *Nat. Rev. Methods Primer* **2**, 33 (2022).

140. Ingber, D. E. Human organs-on-chips for disease modelling, drug development and personalized medicine. *Nat. Rev. Genet.* **23**, 467–491 (2022).

141. Sung, J. H. *et al.* Recent Advances in Body-on-a-Chip Systems. *Anal. Chem.* **91**, 330–351 (2019).

142. Marrero, D. *et al.* Gut-on-a-chip: Mimicking and monitoring the human intestine. *Biosens. Bioelectron.* **181**, 113156 (2021).

143. Kim, H. J., Huh, D., Hamilton, G. & Ingber, D. E. Human gut-on-a-chip inhabited by microbial flora that experiences intestinal peristalsis-like motions and flow. *Lab. Chip* **12**, 2165 (2012).

144. Guo, Y. *et al.* A Biomimetic Human Gut-on-a-Chip for Modeling Drug Metabolism in Intestine: Biomimetic Human Gut-on-a-chip. *Artif. Organs* **42**, 1196–1205 (2018).

145. Fois, C. A. M., Schindeler, A., Valtchev, P. & Dehghani, F. Dynamic flow and shear stress as key parameters for intestinal cells morphology and polarization in an organ-on-a-chip model. *Biomed. Microdevices* **23**, 55 (2021).

146. Shin, W. & Kim, H. J. 3D in vitro morphogenesis of human intestinal epithelium in a gut-on-a-chip or a hybrid chip with a cell culture insert. *Nat. Protoc.* **17**, 910–939 (2022).

147. Kasendra, M. *et al.* Development of a primary human Small Intestine-on-a-Chip using biopsy-derived organoids. *Sci. Rep.* **8**, 2871 (2018).

148. Beaurivage, C. *et al.* Development of a human primary gut-on-a-chip to model inflammatory processes. *Sci. Rep.* **10**, 21475 (2020).

149. Shin, Y. C. *et al.* Three-Dimensional Regeneration of Patient-Derived Intestinal Organoid Epithelium in a Physiodynamic Mucosal Interface-on-a-Chip. *Micromachines* **11**, 663 (2020).

150. Apostolou, A. *et al.* A Novel Microphysiological Colon Platform to Decipher Mechanisms Driving Human Intestinal Permeability. *Cell. Mol. Gastroenterol. Hepatol.* **12**, 1719–1741 (2021).

151. Marr, E. E. *et al.* A platform to reproducibly evaluate human colon permeability and damage. *Sci. Rep.* **13**, 8922 (2023).

152. Puschhof, J., Pleguezuelos-Manzano, C. & Clevers, H. Organoids and organs-on-chips: Insights into human gut-microbe interactions. *Cell Host Microbe* **29**, 867–878 (2021).

153. Kulthong, K. *et al.* Microfluidic chip for culturing intestinal epithelial cell layers: Characterization and comparison of drug transport between dynamic and static models. *Toxicol. In Vitro* **65**, 104815 (2020).

154. Gijzen, L. *et al.* An Intestine-on-a-Chip Model of Plug-and-Play Modularity to Study Inflammatory Processes. *SLAS Technol.* **25**, 585–597 (2020).

155. Eain, M. M. G. *et al.* Engineering Solutions for Representative Models of the Gastrointestinal Human-Microbe Interface. *Engineering* **3**, 60–65 (2017).

156. Jalili-Firoozinezhad, S. *et al.* A complex human gut microbiome cultured in an anaerobic intestine-on-a-chip. *Nat. Biomed. Eng.* **3**, 520–531 (2019).

# 2. Starch emulsion production, characterization and interaction with bacteria

## 2.1. Introduction

Nowadays, obesity is considered a pandemic[1]. In fact, it is worldwide spread with comorbidities, such as colorectal cancer and intestinal bowel disease, causing more deaths than smoking per year[2]. Obese subjects usually suffer from chronic inflammation at the intestinal level and experience increased nutrient absorption, linked to increased intestinal permeability[3,4]. Moreover, obesity is associated with gut flora dysbiosis, impacting energy homeostasis which is strictly connected to the quality of the gut flora. Several studies had connected a dysbiosis in colonic bacteria to different conditions and diseases[5]. In particular, it has been shown that obese patients exhibit a higher *Firmicutes* to *Bacteroidetes* ratio[6], influencing energy homeostasis. Specifically, elevated levels of SCFAs contribute to increased calories absorption, reducing the satiety feeling over time, acting at hormonal levels, with respect to healthy subjects[7,8].

Among the various *Firmicutes* species overrepresented in obese gut flora, *R. Bromii* is crucial for degrading complex carbohydrates, especially starch[10]. This ability is due to the presence of a complex super-enzymatic structure, called amylosome, which is able to bind and degrade starch, taking its name from the main enzyme involved in degradation, which is α-amylase[11]. It has also been demonstrated that other *Firmicutes* bacteria can proliferate better when co-cultured with *R. Bromii*, meaning that its metabolites are used as substrates for other strains and that *R. Bromii* is on the top of the starch degradation pyramid[12]. Hence, the inhibition of *R. Bromii* growth could impact other bacterial strains in a cascading manner. However, preserving the vitality of *R. Bromii* is essential, as it is present, albeit in smaller percentages, also in healthy subjects, so the use of antibiotics should be avoided.

A method to quench bacteria and inhibit their growth without killing them is through contact with an oil phase. In this way bacteria enzymes, being hydrophilic, will not work anymore, preventing bacteria proliferation although leaving them still viable, in a sort of stasis. Furthermore, oil is known for inducing satiety, mainly by increasing the levels of the CCK peptide, a typical satiety signal[13]. Among various oils, soybean oil is known for its beneficial properties on obesity[14].

Taking all these information into account, we developed an O/W microemulsion with starch. The starch, especially in its resistant form, is resistant to digestion as humans lack enzymes able to degrade it[15]. This property makes it suitable as a natural shell, preserving the particles until they reach the colon, where the majority of microflora is present[16]. Once there, bacteria will degrade the starch, releasing the drug. As the intestine of obese subjects is typically affected by chronic inflammation, oil phase can be loaded with anti-inflammatory agents, such as cur, to address this aspect. In addition, in our case, the presence of oil can quench the bacteria as they will be entrapped in the oil phase after starch degradation.

The idea of using starch as a coating agent to make the particles resist in the stomach has already been proposed by other researchers. They took advantage of anaerobic bacteria to degrade it and release the microparticles or the drug[17,18]. However, the main difference with our work is in the possibility of a triple action, taking advantage of the oil. In details, the oil plays a fundamental role as it is involved in quenching bacteria growth, thickening the intestinal barrier and increasing satiety feeling. Along with the potential to address these issues, the oil core loaded with cur can act also as an inflammation reducer (**Fig. 2.1**).

Here, we started with a small percentage of oil and tested the formulation on two bacteria strains. One is *R. Bromii*, while the other is *L. Rhamnosus,* a bacteria that does not degrade starch and should be unable to liberate the oil, serving as a negative control. After having ensured that *L. Rhamnosus* was not influenced by the addition of the starch emulsion, we studied the possibility of increasing the oil percentage, as this is directly connected to the drug payload. Along with that, we also aimed for a small percentage of starch, as the shell had to be the thinnest to promote faster and easier bacteria degradation and drug release. After having obtained the ideal formulation, its rheological properties were evaluated. Finally, cur loading and its resistance in simulated gastric and intestinal fluids were verified.

## 2.2 Materials and Methods

### 2.2.1. Emulsion preparation and characterization

Curcumin (Cur, Sigma-Aldrich, USA) or Nile Red (NR, Sigma-Aldrich, USA) was dissolved in the oil please (soybean oil, Sigma-Aldrich, USA) using a water bath at 60°C for 1 hour as to have a 4 mg/ml or a 0.1 mg/ml solution, respectively. Then, the oil phase was added to the starch solution (soluble starch, Sigma Aldrich, USA) in water phase, which had been pre-heated at 70°C for 30 min. The emulsification process was carried out on the entire solution at 8000 RPM for 20 min using a turbo-emulsifier (Silverson L5T, Silverson Machines Ltd, UK). The resulting emulsion was stored at room temperature. Using this method, three different formulations were produced by varying starch and oil content: 8 wt% starch and 10 wt% oil emulsion, 10 wt% starch and 25 wt% oil emulsion and 8 wt% starch and 25 wt% oil emulsion.

For image acquisition, a drop of emulsion loaded with cur was placed on a glass cover and mixed with a drop of rhodamine B solution (Sigma-Aldrich, USA) at a concentration of 0.1 mg/ml in water to stain the starch. A confocal microscope (LSM900, Zeiss, Germany) was used to observe the emulsion with a 63x objective. A 488 nm laser was employed to observe the oil phase, while a 555 nm laser was used to observe the starch shell.

Images were analyzed with ImageJ to measure the average diameter of the emulsion and, when possible, the thickness of the starch shell.

### 2.2.2. Rheological analysis

The rheological behavior of the emulsion was measured using Anton Paar rheometer (MCR 302, Anton Paar, Austria) coupled with a parallel plate with a diameter of 25 mm. The emulsion was placed on the plate and the gap was set at 1 mm. All measurements were performed at 25°C.

To determine the change in shear stress and viscosity of the material, an initial experiment was performed by varying shear rates from 0.01 1/s to 100 1/s.

An amplitude sweep was performed as to observe the LVE region and the yield point. The test was conducted at a frequency of 10 rad/s while varying the strain from 0.01% to 100%.

Subsequently, a frequency sweep test was conducted at a strain of 0.1%, a value for which the emulsion was within the LVE region. Here, the storage modulus (G') and the loss modulus (G'') were evaluated by varying the frequency from 0.1 Hz to 100 Hz. The complex modulus (G*) and the loss factor (tan δ) were computed based on G' and G'' according to the following formula:

$$\tan\delta = \frac{G''}{G'} \qquad G^* = \sqrt{(G'^2 + G''^2)}$$

### 2.2.3. Simulated digestion and curcumin availability

Curcumin retention in the starch emulsion and in the oil was evaluated in SGF and SIF prepared according to the INFOGEST protocol[19].

Briefly, electrolyte solutions were prepared according to INFOGEST protocol for both SGF and SIF and stored at 4°C until needed. Before the experiment, the fluids were warmed to 37°C and the pH was adjusted to 3 and 7 for SGF and SIF, respectively.

For the gastric phase, $CaCl_2(H_2O)_2$ was added to the solution to obtain a final concentration of 0.15 mM. Then, porcine pepsine and gastric lipase were added to achieve final activities of 2000 U/ml and 60 U/ml, respectively and the pH was adjusted to 3 by using HCl.

For the intestinal phase, $CaCl_2(H_2O)_2$ was added to the solution to obtain a final concentration of 0.6 mM. Then, pancreatin was added to achieve a final activity of 100 U/ml.

The emulsion or the oil were added to the SGF (1:2) and kept stirring at 37°C for 2h. Afterward, part of the solution was diluted in ethanol (1:1) and part was diluted in SIF (1:1). For the SIF, the pH was adjusted at 7 using NaOH and the solution was kept under stirring at 37°C for 2h. Then, ethanol was added to the solution (1:1).

The gastric and intestinal samples were diluted in ethanol to inactivate the enzymes and to extract the CUR from the emulsion. Briefly, after dilution with ethanol, the samples were kept overnight under stirring at room temperature to extract cur. Then, centrifugation (13000 rpm, 15 min) was performed to separate the undigested emulsion and enzymes from the supernatant containing cur. 1 ml of the supernatant was collected and analyzed using UV-visible spectroscopy (Cary 100 Spectrophotometer, Varian, Australia), with cur having a peak at 425 nm. The Lambert-Beer equation was used to compute the overall concentration of the retained CUR inside the emulsion. The retained CUR was computed as a percentage of the theoretical one.

### 2.2.4. Bacteria culture

*Ruminococcus Bromii* (*R. Bromii*) (ATCC 27255) and *Lactobacillus Rhamnosus* (*L. Rhamnosus*) GG strain (ATCC 53103) were obtained in a commercial lyophilized form.

Culture conditions for *R. Bromii* involved an anaerobic incubator with a gas mixture composed of 10% $H_2$, 10% $CO_2$ and 80% $N_2$ (Concept plus anaerobic workstation (AW), Ruskinn technology limited, Italy) at 37 °C. *R. Bromii* was grown in tryptone peptone glucose yeast extract broth base without trypsin (Himedia, India). On the other hand, *L. Rhamnosus* was cultured in static de Man-Rogosa-Sharpe broth (MRS, Oxoid, UK) under microaerophilic conditions at 37°C in a 10% $CO_2$ humidified incubator. Agar (Agar agar type I, Himedia, India) at a final concentration of 1.5 wt% was added to bacteria medium to obtain plates for plate counting.

To obtain the growth curve, the optical density of each strain was read at 600 nm (OD600) through turbidimetric analysis (BioPhotometer Eppendorf, Italy). For the experimental phase, bacteria were selected when in exponential phase, as observed through the formulation of the bacteria growth curve.

### 2.2.5. Live/dead assay on bacteria

The total count of viable/not-viable bacteria was assessed by using the Live/Dead BacLight Bacterial Viability Stain Kit (Molecular Probes, Eugene, USA). Specifically, a sample of each bacteria strain was centrifuged (10000 RPM, 10 min) and washed two times with phosphate buffer solution (PBS, Sigma-Aldrich, USA). Then, 3 µL of a mixture of SYTO9 and PI (1:2) was diluted in 0.5 mL of bacterial suspension and incubated in darkness for 15 min at 37°C. A confocal microscope (LSM900, Zeiss, Germany) with a 63x objective was used for the analysis. Quantitative analyses of each bacterial strain were carried out by analyzing the digital images of live (green) and dead (red) bacteria using ImageJ software.

### 2.2.6. SEM sample preparation and acquisition

1 ml of *R. Bromii* suspension was centrifuged (10000 RPM, 10 min) and washed two times with PBS. Then, 100 µl of this solution was included in an agarose gel to block the bacteria.

The samples were placed in a well and immersed in a 2.5% glutaraldehyde solution (Gluteraldehyde 25% solution, EM grade distillation purified, Electron Microscopy Sciences, USA) in 0.1 M cacodylate (Sodium cacodylate buffer 0.4 M, pH 7.2, Electron Microscopy Sciences, USA) overnight at 4°C. After three washes of 10 min in 0.1 M cacodylate, a 1% osmium solution (Osmium tetroxide 4% aqueous solution, Electron Microscopy Sciences, USA) in 0.1 M cacodylate was applied in the well for 1h at 4°C to strengthen and fix the biological structures. Subsequently, three 10-minute washes in cacodylate were performed. The sequence included washes with ethanol at 10%, 25%, 50% and 70% followed by two washes with ethanol at 80% and 95%, and three washes with 100% ethanol, during which the sample was left until the critical point dryer (EM CPD300, Leica, Germany) procedure.

After drying, samples were placed on the stubs, and metallization was performed using a sputter coater (sputter coater 208-HR, Thickness controller MTM-20, Cressington, UK). The samples were coated with a 20 nm-thick layer of gold and imaged using the scanning electron microscope (Ultra Plus SEM, Zeiss, Germany).

### 2.2.7. Bacteria and emulsion interaction

The emulsions were brought into contact at different concentrations with each bacteria strain for 2 hours in anaerobic or microaerophilic conditions, according to the bacteria's requirements. Subsequently, the bacteria were plated and the colony-forming units per ml (CFU/ml) were calculated.

### 2.2.8. Statistical analysis

Experiments were conducted in triplicates. Briefly, three formulations of the starch emulsion were produced for each case and images were taken at the confocal microscope to analyze their size. For bacteria growth curve and interaction with the carrier, each experiment was repeated three times having three spots in the plate for each experiment and condition. The statistical significance was evaluated with a Welch's T-test. Statistical significance was set as follows: * $p < 0.05$; ** $p < 0.01$; *** $p < 0.001$; **** $p < 0.0001$.

## 2.3. Results

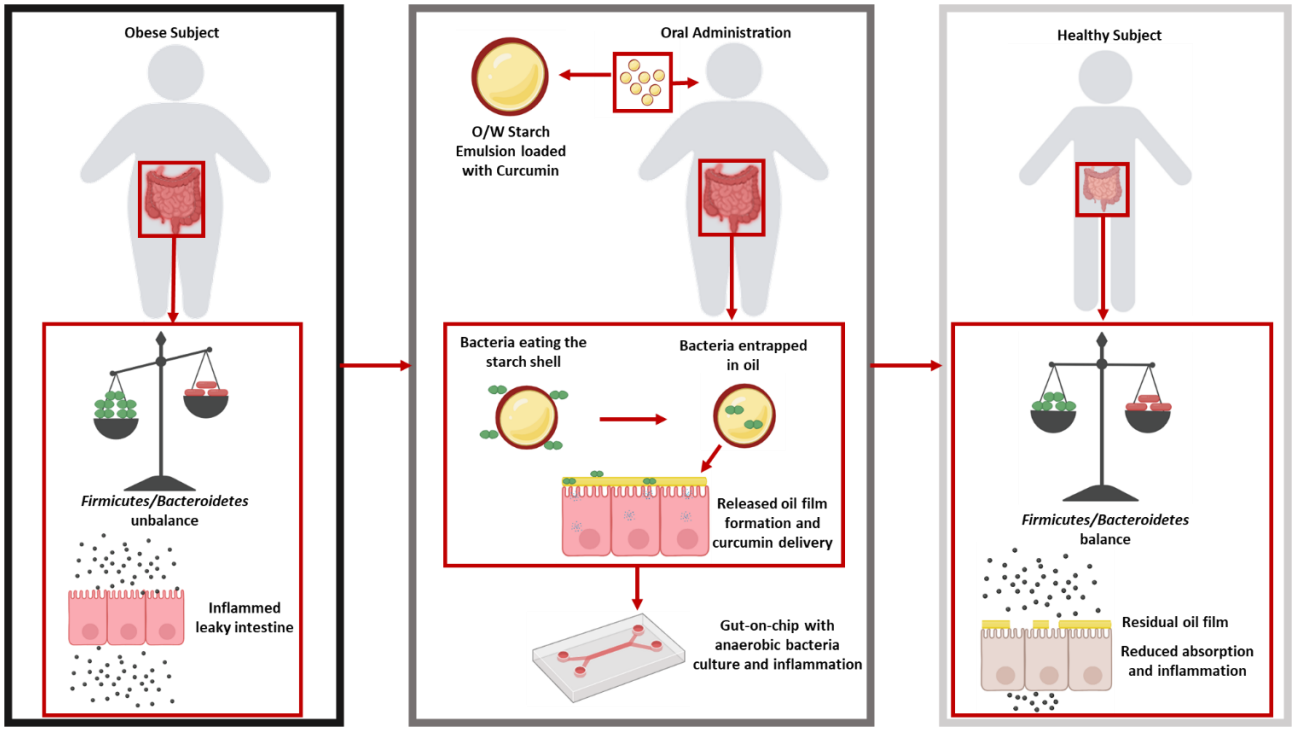


**Figure 2.1**. Graphical Abstract. Image was obtained using Biorender.com.

As mentioned earlier, we chose O/W starch emulsion to address various issues, achieving a triple action. Firstly, the starch is protected until the colon due to the absence of human enzymes capable of degrading it. Here, as the bacteria consume the starch, they are entrapped in the oil losing their metabolic activity, while the liberated oil is released onto the colonic epithelium, thickening it and releasing cur to reduce inflammation status (**Fig. 2.1**).

As previously stated, we selected *R. Bromii* as the bacteria-of-interest since it has the main strain involved in starch degradation and its metabolites can sustain the growth of other *Firmicutes* bacteria. To understand its conformation and size, we imaged it through live/dead and SEM (**Fig. 2.2**). We observed that it tended to form chain-like structures and that is round-shaped, properties typical of *cocci* strains. The size of a single bacterium was around few microns.

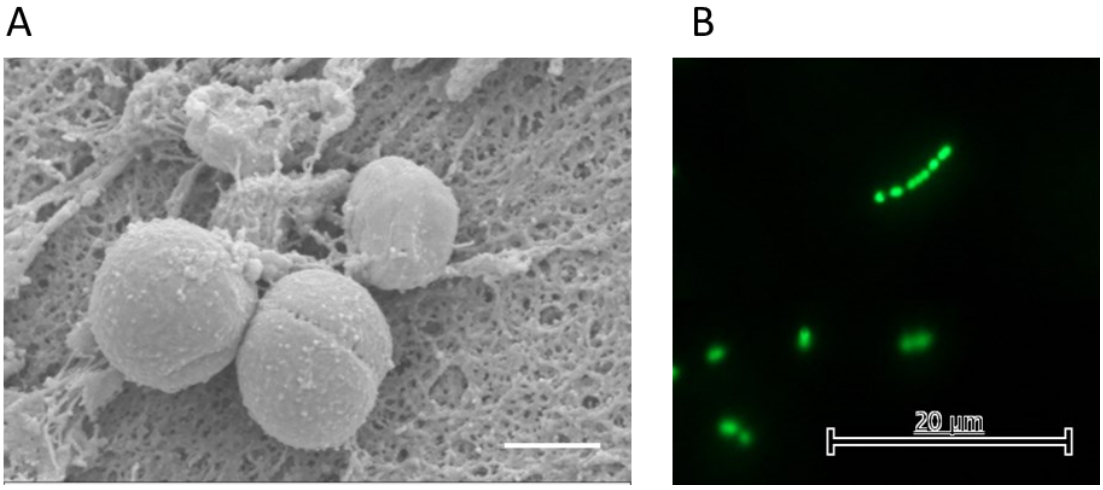


**Figure 2.2.** Imaging of *Ruminococcus Bromii*: SEM image. Scale bar is 500 nm (A); Live staining (B).

Moreover, to perform experiments with bacteria, knowing when they are in exponential phase is crucial, as this is the starting point when bacteria are more prone to grow and proliferate. To achieve this, we developed a growth curve, measuring turbidity, in the form of OD600, at different times. (**Fig. 2.3 A**). From the graph we can discern the different phases typical of bacterial growth. At the beginning there is the lag phase (**Fig. 2.3 B**), during which the bacteria do not grow or grow very slowly due to the adaptation to the growth medium and the new environment. Here, they process the medium proteins, preparing themselves for cellular division (up to about 4 hours, corresponding to an OD600 of 0.19). After this phase, we can recognize the exponential phase, during which cellular division is preponderant and the bacteria start growing consistently in a small amount of time (up to about 24 hours, corresponding to an OD600 of 2.61). Then, the stationary phase takes place. Here the bacteria rate of death and growth are almost equal, as most of the supplements present in the medium have already been used (up to about 31 hours, corresponding to an OD600 of 2.57). Finally, there is the death phase, the first part in which can be seen a significant shift in the curve as the rate of dead bacteria overcomes the rate of new growing ones. Before each experiment, it is fundamental to have an equal starting point, which, in the case of bacteria, is recognized as the start of the exponential phase, which for *R. Bromii* is around an OD600 of 0.70 (**Fig. 2.3 C**).

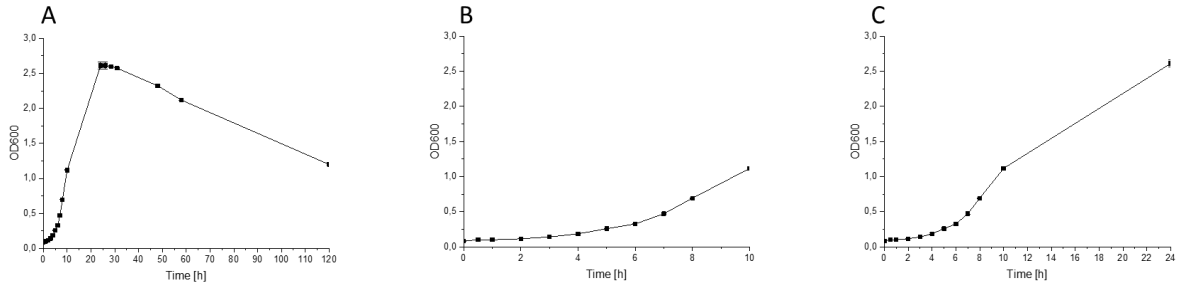


**Figure 2.3.** Growth curve of *Ruminoccocus Bromii* (A). Zoom on the lag phase (B). Zoom on the initial point of the exponential phase (C).

Regarding the emulsions, the first formulation comprised 10 wt% oil and 8 wt% starch. The formulation remained stable for over 1 month and had an average diameter of 4.89 µm with an almost negligible starch shell (**Fig. 2.4**). However, the distribution was right-skewed, featuring a small tail at diameters above 10 µm, due to the production process, which alone did not guarantee a narrow and precise distribution.

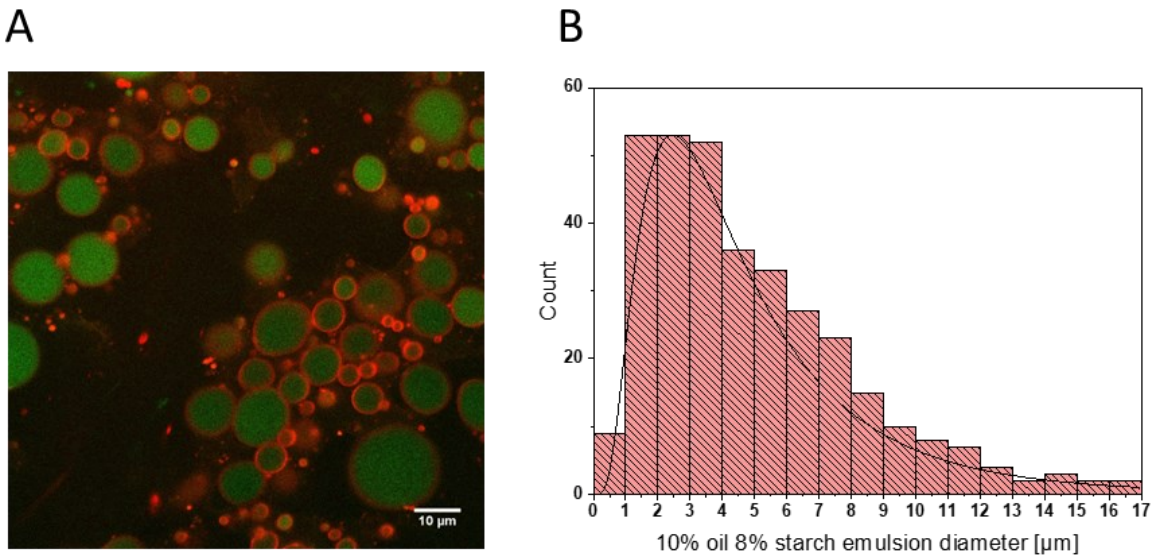


**Figure 2.4.** 10 wt% oil and 8 wt% starch emulsion*:* oil was loaded with curcumin (green) and starch was stained with rhodamine B (red) (A); diameter distribution of the emulsion measured through image analysis (B).

After confirming the conformation and the growth of *R. Bromii* and characterizing the emulsion size, we tested this formulation on both *R. Bromii*, our species of interest which degrades starch, and *L. Rhamnosus*, a *Bacteroidetes* strain which does not degrade starch. Two different concentrations were tested as to achieve a final percentage of oil equal to 2 wt% and 0.2 wt%. As a control, the same concentration of starch present in the emulsion was dissolved in the culture broth but in a free state. A live/dead assay was performed to estimate the difference between viability and growth. All tested concentrations showed no toxic effects, as the live bacteria were all comparable to the control.

*L. Rhamnosus* growth was not affected by either free starch or the emulsion, demonstrating its inability to degrade starch, whether in a free form or used as a surfactant agent for emulsion. The difference in growth was not significant, meaning that the bacteria were not influenced by either free starch or the emulsion, which remained unaltered after the contact (**Fig. 2.5 D-E-F**). On the other hand, *R. Bromii* colonies significantly decreased by almost one order of magnitude when in contact with a final concentration of oil equal to 2 wt%, compared to the corresponding free starch. In fact, it decreased from 9.58 CFU/ml to 8.75 CFU/ml (p-value < 0.01). In contrast, the lower oil concentration (0.2 wt%) showed no significant difference compared to the corresponding free starch. This suggests that there is a threshold in the oil concentration needed to observe a significant effect on *R. Bromii* growth. Vitality was not affected by the emulsion presence in the growth medium (**Fig. 2.5 A-B-C**).

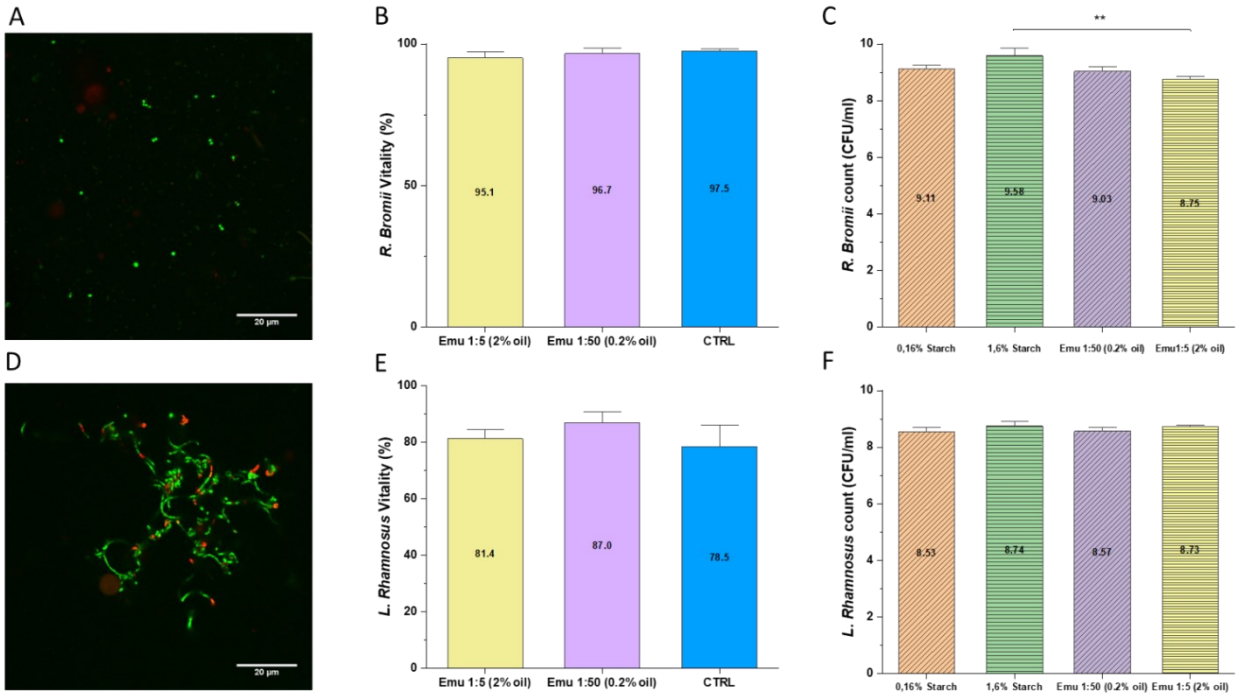


**Figure 2.5**. Bacteria interaction with 10 wt% oil and 8 wt% starch emulsion. *Ruminoccocus Bromii*: live (green)/dead (red) staining (A); vitality was computed through live/dead image analysis (B); growth computed through plate counting as log (C). *Lactobacillus Rhamnosus*: live (green) /dead (red) staining (D); vitality was computed through live/dead image analysis (E); growth computed through plate counting as log (F). (** $p < 0.01$; n = 3 plates for 3 different experiments).

As this seems a promising result, the quantity of emulsion needed to have a significant effect is very high. To improve the dosage, we increased the oil percentage from 10 wt% to 25 wt%. In a first attempt, we also increased the starch quantity from 8 wt% to 10 wt% to achieve a more stable formulation. In such a case, the average diameter was equal to 4.14 µm (**Fig. 2.6 A-B**). However, as the size seemed to diminish due to the higher starch concentration, the starch shell became much thicker than the previous formulation, around 0.5 µm (**Fig. 2.6 C**). This does not favor bacteria degradation. In fact, if the starch is too thick, the oil will not be available for the bacteria and will not be released as they have to travel and undergo further degradation before the oil core can be liberated. Hence, we produced a 25 wt% oil and 8 wt% starch emulsion with an average diameter of 6.16 µm and a thinner starch shell (**Fig. 2.6 D-E**).

Comparing the three formulations, we observed significant differences. In particular, the increase in starch content resulted in diminished particle dimensions. This could be attributed to the starch mesh becoming more compact as its concentration increases. As expected, the 25 wt% oil and 8 wt% starch formulation had the highest particles diameter, as an increase in the oil percentage led to particles having less space within the meshes, making them more prone to collapse one to another, thereby increasing the overall particle size (**Fig. 2.6 F**).

Furthermore, all the three formulations exhibited right-skewed distributions, with particles above 10 µm appearing. This skewness could be mainly attributed to the production method, which consisted of turbo-emulsification only and did not guarantee a narrow distribution. Methods to improve this aspects are currently being tested.

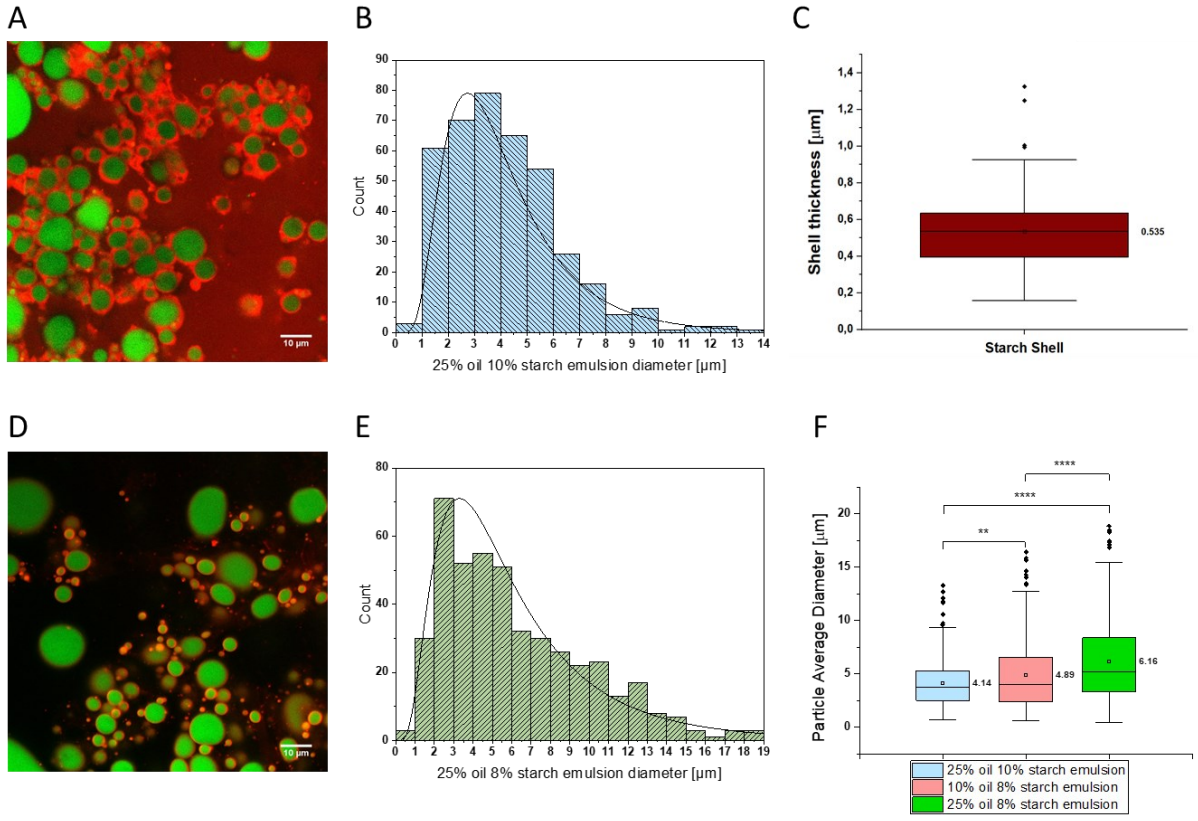


**Figure 2.6.** 25 wt% oil and 10 wt% starch (w/w) emulsion: oil was loaded with curcumin (green) and starch was stained with rhodamine B (red) (A); Diameter distribution of the emulsion measured through image analysis (B); average shell thickness measured through image analysis (C). 25 wt% oil and 8 wt% starch emulsion: oil was loaded with curcumin (green) and starch was stained with rhodamine B (red) (D); diameter distribution of the emulsion measured through image analysis (E). Comparison between the particle average diameter of the three formulations (F). (** $p < 0.01$; **** $p < 0.0001$; n = 3 formulations).

Once we obtained the final formulation, i.e., the 25 wt% oil and 8 wt% starch emulsion, we further characterized it through rheometer analysis. During the production of the emulsion, the starch underwent a jellification process, meaning that its rheological properties changed considerably. Indeed, the emulsion acted as a shear-thinning fluid as the viscosity decreased with increasing shear rates (**Fig. 2.7 A**). This behavior is

typical of colloidal fluids, where particles at rest or subjected to low shear rates are randomly arranged, acting almost as solids. When higher shear rates are applied, the soft particles are broken or deformed, increasing the amount of free space between particles and resulting in lower viscosity values[20].

This behavior is further confirmed by the analysis of storage and loss modulus during an amplitude sweep (**Fig. 2.7 B**). Here, we can notice a LVE region up to about 1% of strain, where the storage modulus (G') is higher than the loss modulus (G''), indicating a viscoelastic solid-like behavior, while both of them remained linear. After that, G' started to decrease, while G'' increased up to about 10% strain. After this point, both moduli decreased up to the yield point, where occurs the most consistent change in viscoelastic properties, as G'' > G'. After the yield point, the emulsion started to act as a viscoelastic fluid. A frequency sweep was performed to understand the properties of the emulsion. We conducted this test at a constant strain equal to 0.1% because at this strain the emulsion was still in the LVE region, computing G' and G'' (**Fig. 2.7 C**). From these two parameters it is possible to compute the tangent of δ (tan δ) and the complex modulus (G*). As **Fig. 2.7 D** shows, G* ranged between 900 Pa and 1200 Pa, with mechanical properties increasing with the frequency. Regarding tan δ, it ranged between 0.11 and 0.30, values typical of gel-like materials. In fact, for tan δ < 1 the material is considered an elastic material.

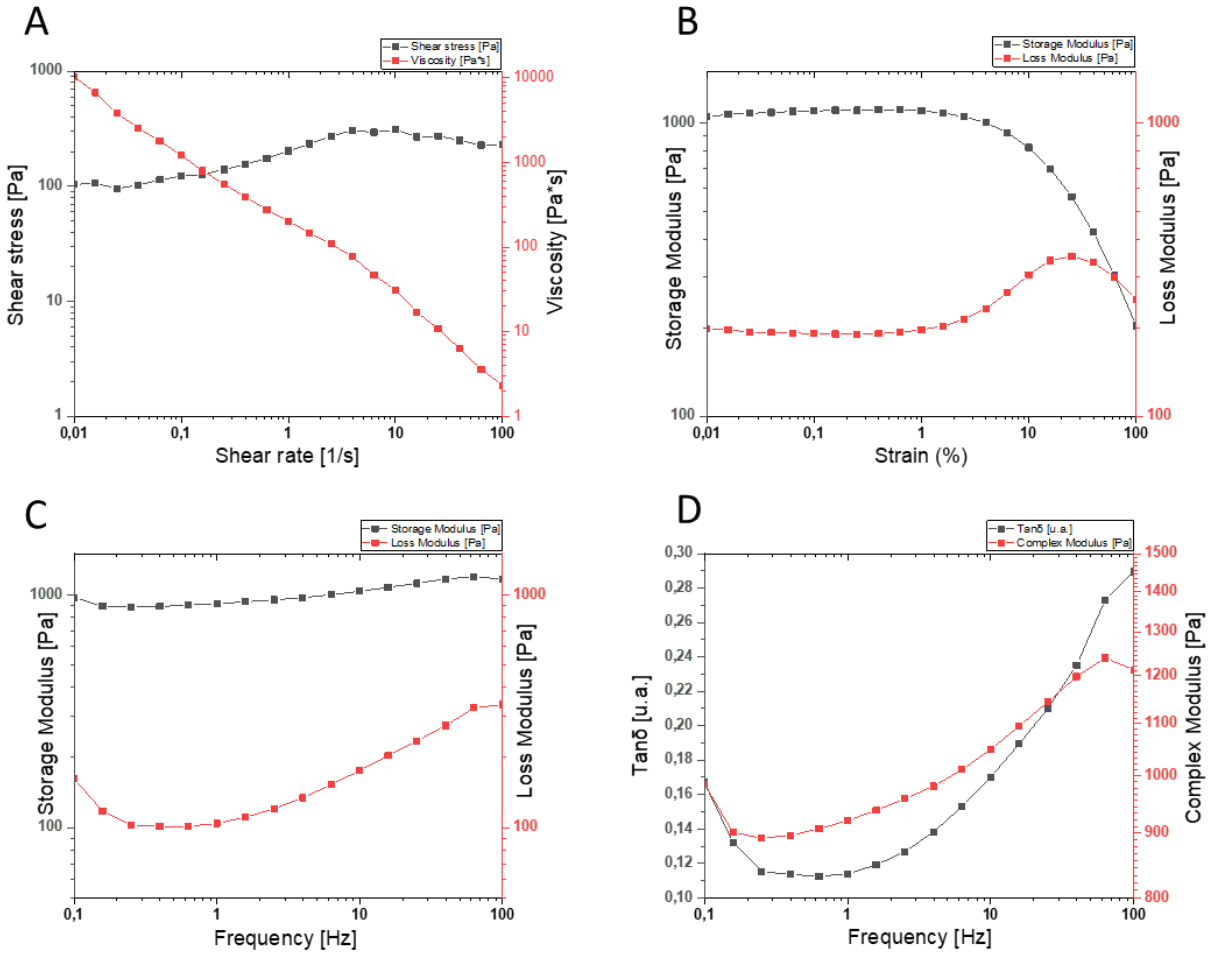

**Figure 2.7**. Rheological analysis of 25 wt% oil and 8 wt% starch emulsion. Shear stress and viscosity compared to shear rate indicates a shear thinning behavior (A). The amplitude sweep was used to compute loss and storage moduli as to understand the viscoelastic linear region and the yield point (B). Frequency sweep was implanted to compute the storage modulus (G') and the loss modulus (G'') (C). Complex modulus (G*) and tan δ computed from G' and G'' (D).

To further characterize the cur-loaded emulsion, we studied its degradation in SGF and SIF. As a control, we used cur-loaded oil. We quantified the remaining cur either inside the oil or the emulsion by extracting it after each digestion phase. As shown in **Fig. 2.8 A**, the emulsion consistently protected the cur better than the free oil in each phase ($p < 0.001$).

To further demonstrate the impact of the oil on *R. Bromii*, we studied its growth when in contact with the 25 wt% oil and 8 wt% starch emulsion for 2 hours, using the same dilution to achieve a final oil concentrations of 0.2 wt% and 2 wt%. As observed in **Fig. 2.8 B**, an increase in the oil percentage led to a significant decrease in the growth of *R. Bromii*. In details, the differences from the free starch control were not significant for 0.2 wt%, while it was significantly different for a final oil concentration equal to 2 wt% ($p < 0.0001$), aligning with the earlier results obtained with the first formulation (**Fig. 2.5**). In particular, the final formulation was able to decrease the growth of *R. Bromii* of over one order of magnitude, dropping from 10.1 CFU/ml for the free starch control to 8.74 CFU/ml.

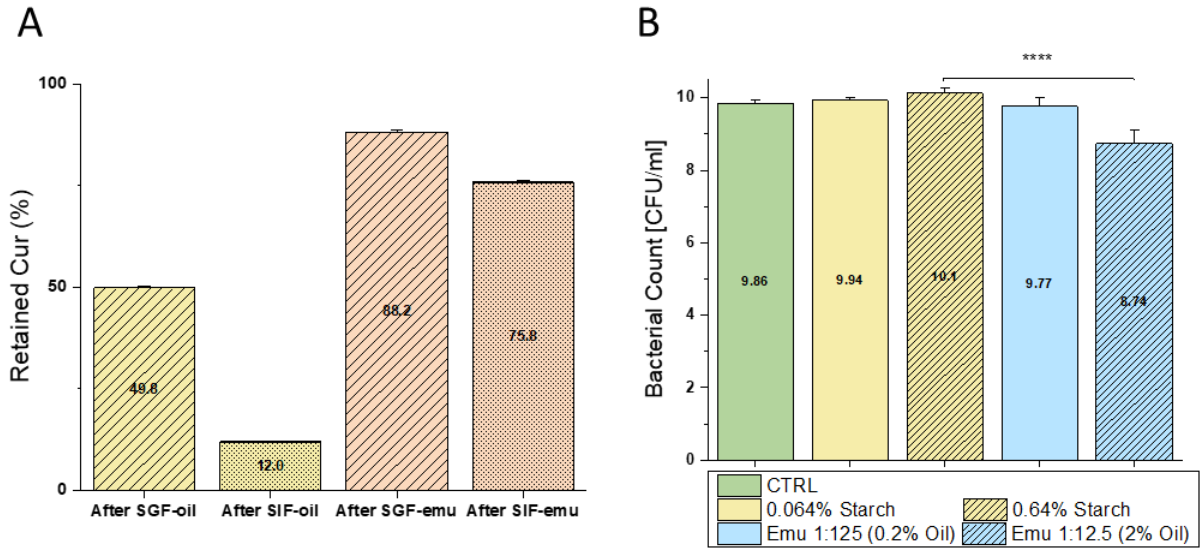


**Figure 2.8**. Digestion of curcumin loaded emulsion (25 wt% oil and 8 wt% starch) and oil in simulated gastric and intestinal fluids. The retained curcumin was calculated from the theoretical one (A). *Ruminoccocus Bromii* interaction with 25 wt% oil and 8 wt% starch emulsion. Free starch was used as a control. Growth was computed through plate counting. The bacteria counts are presented as log (B). (**** $p < 0.0001$; n = 3 plates for 3 different experiments).

Furthermore, the bacteria where entrapped in the oil, which can motivate their inability to grow (**Fig. 2.9**).

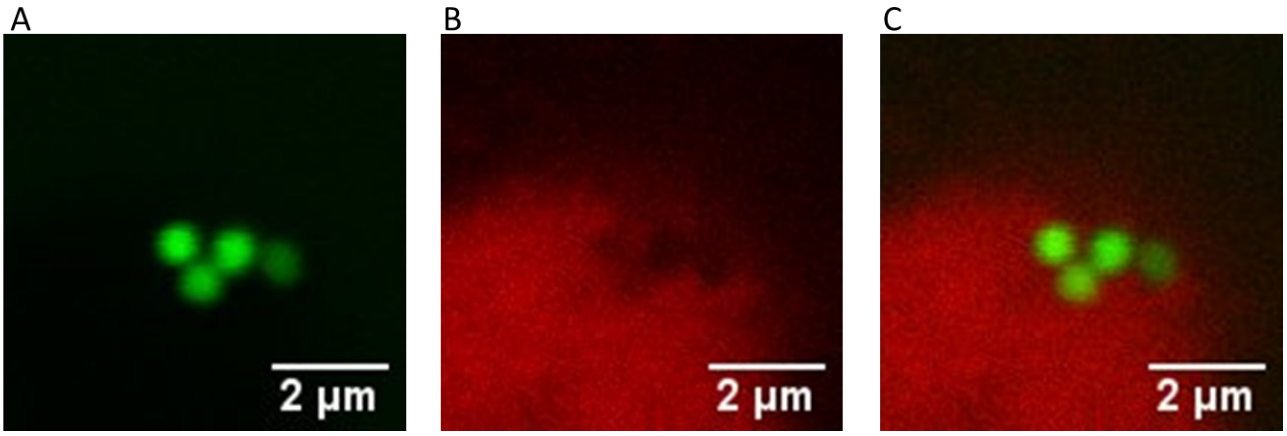


**Figure 2.9**. Entrapment of *Ruminococcus Bromii* into the oil phase. Live staining (green, A); nile red staining of the oil phase (red, B); merge of the two channels (C).

## 2.4. Discussion

In this chapter, firstly the growth and size of *R. Bromii* under standard anaerobic conditions were analyzed to visualize its shape and understand its behavior. The growth curve allowed us to appreciate each phase typical of bacterial growth, with a specific focus on the exponential phase, serving as a starting point for subsequent bacterial experiments.

Simultaneously, a stable O/W starch emulsion was developed, beginning with a formulation containing 10 wt% oil and 8 wt% starch to ensure optimal stability. This emulsion was tested on two bacteria strains: *R. Bromii,* a strictly anaerobic strain crucial for starch degradation, and *L. Rhamnosus,* a microaerophilic strain that does not degrade starch, serving as a negative control. Results demonstrated *R. Bromii*'s ability to degrade the particles while being entrapped in the oil phase, quenching its metabolic activity without affecting its viability. Conversely, *L. Rhamnosus* was not significantly impacted by the emulsion or free starch, nor in metabolic activity nor in viability. These findings correlated well with *L. Rhamnosus*'s inability to degrade the emulsion's external shell and to release the oil core, highlighting the emulsion's efficacy in connection with starch degradation.

However, considering that a final concentration of oil equal to 0.2 wt% did not produce significant differences, the required amount of emulsion for effectiveness seemed quite high. To address this, we increased the oil percentage, recognizing that higher oil percentages could achieve similar results with lower dosages. Initially, a 25 wt% oil and 10 wt% starch emulsion was tested taking into account that a higher percentage of oil is usually connected to a higher percentage of the surfactant to provide similar stability. While this formulation displayed lower poly-dispersion and a smaller average diameter, the increase in starch concentration led to a significant thickening of the starch shell, which can be detrimental to our objectives. As a matter of fact, oil percentage and starch shell thickness are two fundamental parameters in our work. A thin starch shell ensures a easier breakage of the particles by the bacteria, so that they have to travel less to reach the oil core upon

starch shell degradation. On the other hand, the oil percentage is important when considering dosage. In fact, increasing the oil percentage, a higher amount of cur can be administered without changing the initial dosage.

Recognizing the importance of both starch shell thickness and oil percentage, the formulation was adjusted to 25 wt% oil and 8 wt% starch, maintaining stability and a small particle size. This change in oil percentage enhances patient compliance, allowing for lower dosages to achieve the same beneficial effects. However, it should be noted that turboemulsification alone cannot provide a monomodal distribution of particles, as evidenced by a small percentage of particles above 10 μm. This final formulation had the highest average particle diameter due to the increase in the oil phase to starch ratio.

After selecting the appropriate formulation, it was further characterized. The rheological analysis showed that the emulsion behaves as a shear thinning fluid, displaying decreased viscosity with increasing shear rates. In particular, viscosity decreased rapidly from 1000 Pa*s at a shear rate of 0.01 1/s to nearly 1 Pa*s at a shear rate of 100 1/s. This rapid change is typical of emulsions, where high shear rates deform and even break oil particles, resulting in more viscous properties[21].

The starch jellification contributed to a transition towards a gel-like behavior of the emulsion, particularly noticeable at large strain percentages, approximately around 50%. This shift was corroborated by the frequency sweep, where tan δ remained below 1 across the entire frequency range, indicative of properties typical of a gel-like material. This aligns with findings from other studies on jellified potato starch[22,23] and starch-based emulsion gels[24].

The starch shell demonstrated the capability to protect the cur-loaded in the oil phase from the harsh conditions of the GIT, as demonstrated by the INFOGEST protocol *in-vitro*. Nearly 80% of cur remained available after exposure to the SIF, indicating the emulsion's potential to reach the colon nearly intact.

Concerning bacteria, once it was established through a live/dead assay that the emulsion was not toxic to the gut flora, as expected due to its composition of biodegradable and food grade compounds, and acted specifically on starch-degrading species, the final formulation was tested on *R. Bromii*. Here, a significant decrease in *R. Bromii* growth was observed as the oil percentage exceeded 0.2 wt%. Notably, administering a final oil concentration of 2 wt% resulted in a decrease of more than one order of magnitude. Additionally, *R. Bromii* was entrapped in the oil, providing explanation for its growth reduction.

In other words, *R. Bromii* could "eat" the starch and reach the oil core, where the oil effectively inhibited the catalytic sites of *R. Bromii* enzymes, which are hydrophilic, quenching its metabolic activity without compromising viability.

## 2.5. Conclusion

In conclusion, in this chapter a stable, we developed few-micron-sized starch emulsion with a thin external starch shell and a high oil loading (25 wt%). These parameters are crucial for effectively targeting bacteria, considering the distance they need to travel before reaching the oil core upon starch shell degradation. The emulsion efficiently and specifically targeted starch-degrading bacteria, resulting in significant results above 0.2 wt% of oil, with a difference of one order of magnitude for a final oil concentration equal to 2 wt%, without affecting the growth of other gut flora bacteria and maintaining high viability for all strains.

The carrier exhibited viscoelastic properties similar to other gel emulsions made with starch, displaying a prominent gel-like behavior up to large shear rates, where the viscous properties became predominant. Overall, the rheological behavior indicated a shear-thinning material, typical of colloidal materials. Considering all aspects, this strategy holds promise for implementation in treating obese subjects due to the ability to quench without killing bacteria overrepresented in their gut, thereby diminishing energy harvesting associated with SCFAs formation by starch-degrading bacteria.

In the upcoming chapters, we will show how the oil can act also as a thickening agent for the intestinal epithelial barrier, demonstrating this in a suitable *in-vitro* platform, namely, the gut-on-chip.

## 2.6. Bibliography


1. Meldrum, D. R., Morris, M. A. & Gambone, J. C. Obesity pandemic: causes, consequences, and solutions—but do we have the will? *Fertil. Steril.* **107**, 833–839 (2017).

2. Ward, Z. J. *et al.* Excess mortality associated with elevated body weight in the USA by state and demographic subgroup: A modelling study. *eClinicalMedicine* **48**, 101429 (2022).

3. Spagnuolo, M. I. *et al.* Relationship between severe obesity and gut inflammation in children: what's next? *Ital. J. Pediatr.* **36**, 66 (2010).

4. Brun, P. *et al.* Increased intestinal permeability in obese mice: new evidence in the pathogenesis of nonalcoholic steatohepatitis. *Am. J. Physiol.-Gastrointest. Liver Physiol.* **292**, G518–G525 (2007).

5. Guarner, F. & Malagelada, J.-R. Gut flora in health and disease. *The Lancet* **361**, 512–519 (2003).

6. Duranti, S., Ferrario, C., van Sinderen, D., Ventura, M. & Turroni, F. Obesity and microbiota: an example of an intricate relationship. *Genes Nutr.* **12**, 18 (2017).

7. Tremaroli, V. & Bäckhed, F. Functional interactions between the gut microbiota and host metabolism. *Nature* **489**, 242–249 (2012).

8. May, K. S. & Den Hartigh, L. J. Modulation of Adipocyte Metabolism by Microbial Short-Chain Fatty Acids. *Nutrients* **13**, 3666 (2021).

9. Duca, F. A., Waise, T. M. Z., Peppler, W. T. & Lam, T. K. T. The metabolic impact of small intestinal nutrient sensing. *Nat. Commun.* **12**, 903 (2021).

10. Ze, X., Duncan, S. H., Louis, P. & Flint, H. J. Ruminococcus bromii is a keystone species for the degradation of resistant starch in the human colon. *ISME J.* **6**, 1535–1543 (2012).

11. Mukhopadhya, I. *et al.* Sporulation capability and amylosome conservation among diverse human colonic and rumen isolates of the keystone starch-degrader *Ruminococcus bromii*: Comparative genomics of *Ruminococcus bromii*. *Environ. Microbiol.* **20**, 324–336 (2018).

12. Crost, E. H. *et al.* Mechanistic Insights Into the Cross-Feeding of Ruminococcus gnavus and Ruminococcus bromii on Host and Dietary Carbohydrates. *Front. Microbiol.* **9**, 2558 (2018).

13. Beglinger, C. & Degen, L. Fat in the intestine as a regulator of appetite—role of CCK. *Physiol. Behav.* **83**, 617–621 (2004).

14. Velasquez, M. T. & Bhathena, S. J. Role of Dietary Soy Protein in Obesity. *Int. J. Med. Sci.* 72–82 (2007) doi:10.7150/ijms.4.72.

15. Apriyanto, A., Compart, J. & Fettke, J. A review of starch, a unique biopolymer – Structure, metabolism and in planta modifications. *Plant Sci.* **318**, 111223 (2022).

16. Chen, L. *et al.* Resistant starch as a carrier for oral colon-targeting drug matrix system. *J. Mater. Sci. Mater. Med.* **18**, 2199–2203 (2007).

17. Khan, A. *et al.* Development of Resistant Starch Film Coated Microparticles for an Oral Colon-Specific Drug Delivery. *Starch - Stärke* **72**, 1900262 (2020).

18. Xu, C. *et al.* Colon-targeted oral nanoparticles based on ROS-scavenging hydroxyethyl starch-curcumin conjugates for efficient inflammatory bowel disease therapy. *Int. J. Pharm.* **623**, 121884 (2022).

19. Brodkorb, A. *et al.* INFOGEST static in vitro simulation of gastrointestinal food digestion. *Nat. Protoc.* **14**, 991–1014 (2019).

20. Xu, W. *et al.* Rheological behavior and microstructure of Pickering emulsions based on different concentrations of gliadin/sodium caseinate nanoparticles. *Eur. Food Res. Technol.* **247**, 2621–2633 (2021).

21. Pei, Y., Zhang, Y., Ding, H., Li, B. & Yang, J. Stability and Rheological Behavior of Mayonnaise-like Emulsion Co-Emulsified by Konjac Glucomannan and Whey Protein. *Foods* **12**, 2907 (2023).

22. Hu, Y., Li, C., Tan, Y., McClements, D. J. & Wang, L. Insight of rheology, water distribution and in vitro digestive behavior of starch based-emulsion gel: Impact of potato starch concentration. *Food Hydrocoll.* **132**, 107859 (2022).

23. Liu, Z., Zhang, M., Bhandari, B. & Yang, C. Impact of rheological properties of mashed potatoes on 3D printing. *J. Food Eng.* **220**, 76–82 (2018).

24. Zhao, X., Li, D., Wang, L. & Wang, Y. Rheological properties and microstructure of a novel starch-based emulsion gel produced by one-step emulsion gelation: Effect of oil content. *Carbohydr. Polym.* **281**, 119061 (2022).

# 3. Gut-on-chip production and characterization

## 3.1. Introduction

In recent years, there has been an intensified need for cost and animal use reduction in drug screening for both efficacy and toxicity tests. One way to address this problem is through the use of microfluidic platform capable of reproducing the main functions of several organs, known as organ-on-chips[1]. These platforms typically consist of microfluidic channels where mechanical forces and environmental cues are able to make cells differentiate and behave like an *in-vivo* organ, closely mimicking its main functionalities. This approach offers an alternative to animal testing as a first screening platform. Organ-on-chip models not only reduce the number of animals needed, but also provide a more accurate response to drugs compared to simple 2D cell culture, owing to the dynamic environment[2]. Additionally, they open up the possibility of personalized medicine, allowing the analysis of unique drug responses starting from biopsies taken from patients[3].

Among various organ-on-chip models, the gut-on-chip has garnered significant attention due to its central role in oral delivery, the ability to include gut flora associated to various diseases, and the integration of immune cells[4]. These platforms can replicate physiological and functional aspects of the human intestinal tract[5]. Furthermore, they serve as valuable tools to study pathological conditions such as inflammation, infections and cancer[6,7].

Typically, gut-on-chip models consist of two channels separated by a polymeric membrane, where shear stresses induce cell differentiation[8]. Incorporating gut bacteria can occur in two ways. The easiest method is to add another channel, so that cells and bacteria are separated, which is useful because of the difference in environmental needs as most gut bacteria are strictly anaerobic[9]. Nevertheless, this method does not take into account a real host-bacteria interaction and there is a time loss in each experiment as the metabolites produced by bacteria are not readily available for cells having to pass another membrane before reaching the epithelium.

The other possibility is to co-culture cells and bacteria in the same channel. This is certainly closer to the *in-vivo* situation, although there is a complication arising from the difference in oxygen need between bacteria, which are anaerobic, and cells, which are aerobic[10]. In this case the oxygen gradient becomes fundamental and it should be properly engineered to ensure both cells and bacteria viability.

Here, a gut-on-chip platform composed of two channels separated by a polycarbonate membrane was described. One channel represents the epithelium, while the other serves as a collection channel. Two gold wires were added to each channel for TEER measurements. Anaerobic and aerobic bacteria were cultured in the cell channel, demonstrating their vitality. Key features typical of the intestine, such as mucus production, villi formation, and tight junction formation, were assessed.

Overall, this platform appears promising for pharmacokinetic and drug screening experiments, as it encompasses key *in-vivo* characteristics typical of the intestine. The next chapter will provide evidence of its capabilities.

## 3.2. Materials and Methods

### 3.2.1. Cells and bacteria culture

Human colonic epithelial cell lines (Caco-2) were obtained from the American Type Culture Collection (ATCC) and cultured in High-glucose DMEM (Hg-DMEM, GIBCO). The medium was supplemented with 10% fetal bovine serum (FBS, Sigma-Aldrich, USA), 1% of L-glutamine (Himedia, India), and 1% of penicillin and streptomycin solution (P/S, Sigma Aldrich, USA) and grown at 37 °C in a 5% $CO_2$ humidified incubator. Cells from passages 5 to 20 were used for experiments.

*Ruminococcus Bromii* (*R. Bromii*) (ATCC 27255) and *Lactobacillus Rhamnosus* (*L. Rhamnosus*) GG strain (ATCC 53103) were obtained in a commercial lyophilized form. Culture conditions for *R. Bromii* involved an anaerobic incubator with an anaerobic gas mixture composed of 10% $H_2$, 10% $CO_2$ and 80% $N_2$ (Concept plus anaerobic workstation (AW), Ruskinn technology limited, Italy) at 37 °C. *R. Bromii* were grown in tryptone peptone glucose yeast extract broth base without trypsin (Himedia, India). On the other hand, *L. Rhamnosus* was cultured in static de Man-Rogosa-Sharpe broth (MRS, Oxoid, UK) in microaerophilic condition at 37°C in a 10% $CO_2$ humidified incubator. For the experimental phase, each strain's optical density was read at 600 nm (OD600) by turbidimetric analysis (BioPhotometer Eppendorf, Italy) and bacteria were selected when in exponential phase. Before the experiment, *R. Bromii* was grown in cell medium without P/S, previously set in anaerobic conditions to avoid oxygen presence, while *L. Rhamnosus* was grown in standard conditions.

### 3.2.2. CFD Simulation

To understand the oxygen gradient and the shear stresses forming at the cell layer, we used a commercial simulation software, Comsol Multiphysics version 6.0.0.354 (COMSOL Inc., Sweden). The device was schematized as two channels separated by a porous membrane and a cell layer. PDMS layers on the top and bottom of the device were added. We implemented "Laminar flow" in the two channels as well as in the cell and membrane layers. "Transport of diluted species in porous media" was implemented in every region. The simulations considered the culture medium having the same properties as water, and various parameters were employed to model oxygen diffusion and consumption by cells. The parameters used were the followings:

**Tab. 3.1**: Comsol simulation parameters

| Parameter | Value |
|---|---|
| Dcell | $10^{-10}\ m^2/s$ |

| | |
|---|---|
| Vmax | $3.5 * 10^{-5}$ mol/($m^3$s) |
| Km | $10^{-3}$ mol/$m^3$ |
| Dmed | $3.24 * 10^{-9}$ $m^2$/s |
| Dpdms | $3 * 10^{-9}$ $m^2$/s |
| Q | 2 µl/min |
| εp | 0.15 |
| $CO_2$_0 | 0.22 mol/$m^3$ |

where, Dcell, Dmed and Dpdms are the diffusion coefficients of oxygen in the cell layer, the culture medium and the PDMS, respectively.

The oxygen consumption by the cells was schematized by Michaelis-Menten equation:

$$-\frac{Vmax*c}{Km+c}$$

where c is the oxygen concentration, while $V_{max}$ is the maximum reaction rate of oxygen and Km is the concentration of oxygen at which half of $V_{max}$ is achieved. The last two are the ones defined in **Tab. 3.1.**

εp is the porosity of the membrane, while Q is the flow rate of the culture medium in each channel.

The simulations were performed in two cases: i) oxygen passing through both the bottom and top PDMS layers; ii) oxygen passing only through the upper PDMS layer.

The study was time-dependent with a step size of 0.2 hours ranging from 0 to 10 hours.

Two cut lines were defined, one at the center of the whole device, the other at the center of the lower channel for better observation of oxygen variations.

### 3.2.3. Device production

The microfluidic gut-on-chip was fabricated through replica molding of polydimethylsiloxane 10:1 (w/w) with the curing agent (PDMS; Sylgard 184; Mascherpa, Italy) from a poly-(methyl methacrylate) (PMMA, Goodfellow, UK) master. The PMMA master, designed using AutoCAD and created with Micromilling (Minithech CNC, Mini-Mill, USA), featured a single channel (53 mm length x 2 mm width x 1 mm height) and two housings for inlet and outlet. The PDMS was poured on the PMMA master, degassed under vacuum for 30min to remove air bubbles, cured in an oven at 80°C for 60 min and then peeled off from the PMMA master. To obtain the gut-on-chip two identical replicas were needed. In one of the two replicas, 4 holes were punched with a 1.5 mm biopsy punch (Cantabria Labs, DIFA COOPER S. p.A, Italy) in correspondence of the

housing of the upper and lower channel inlet and outlet. A scalpel was used to make a small cut in the central part of the device, perpendicular to the channel, to house the gold wire. A drop of PDMS was dispensed on it and then the whole replica was cured in an oven at 80°C for 60 min in order to close the cut. The replica with the 4 holes was treated with oxygen plasma for 1 min at 50 W (Plasma Femto, Diener, Diener electronic GmbH, Germany). Then, a piece of polycarbonate membrane (Isopore polycarbonate membrane 0.4 µm pore size, Millipore, USA) was cut and put on the channel and few drops of a solution of (3-Aminopropyl)triethoxysilane (Aptes, Sigma-Aldrich, USA) at 5% in MilliQ water pre-heated at 80°C for 15 min were dropped on the membrane. Then, this was cured in an oven at 80°C for few minutes in order to let water dry. The replica with the membrane was treated with oxygen plasma for 1 min at 50 W together with the replica without it and a glass cover (24 mm wide × 60 mm long**,** Menzel-Gläser, Epredia, USA). The two pieces were combined together and the glass cover was put on the size without punch holes. The final device was cured in an oven at 80°C overnight to make all pieces bond together.

### 3.2.4. Cell and bacteria culture in gut-on-chip

The gut-on-chip was sterilized under biological hood with a filtered 70% ethanol solution (w/w), perfused in both channels and let rest for 50 min, followed by a filtered P/S 2% solution in PBS (w/w) perfused three times to avoid any ethanol leftover. Air was then perfused and the device was left under UV light for 1 hour with inlet and outlet opened.

To allow cell adhesion to the membrane, the device was perfused with a collagen (collagen type I, rat tail, IBIDI, Germany) solution in PBS (0.03 mg/ml) and placed in the humidified incubator at 37°C for 45 min. The collagen was then washed with PBS once, and the cell medium was perfused, allowing the gut-on-chip to acclimatize for 20 min. Afterward, 600000 cells were added to the device overnight in static conditions. The day after, the microfluidic device was transitioned to dynamic conditions using a syringe pump (Harvard Apparatus, USA) with a flow rate of 2 µl/min for 7 to 10 days.

For bacteria culture, the cell medium without P/S was left overnight in the anaerobic hood, open to allow the replacement of oxygen with nitrogen. The cell medium without P/S was put in the gut-on-chip overnight after two PBS washing. The day after, 1 ml of bacteria in exponential phase were centrifuged (10000 RPM, 10 min) and washed with PBS one time. Then, they were resuspended in the oxygen-free medium. The device were put under the anaerobic hood to insert bacteria in the cell channel. The bacteria were left for 4 hours in the device to let them adhere to cells. After that, the device was put in dynamic conditions again at 2 µl/min with oxygen-free medium for 3 days.

### 3.2.5. TEER Measurements

To measure the TEER, the two gold wires coming from the upper and lower channel of the gut-on-chip were connected to a potentiostat/galvanostat (Autolab PGSTAT204, Metrohm, Switzerland) operating in

potentiostatic mode at 10 µA. The Nova software (version 2.1.3, Metrohm, Switzerland) was utilized for resistance computation across frequencies ranging from 10 to 100000 Hz. The medium resistance, representing the device's resistance without cells, was subtracted from the TEER. The resulting value was then multiplied by the surface area of the cell culture to obtain the final TEER value.

### 3.2.6. Fluorescein isothiocyanate (FITC)-dextran permeability assay

For the permeability assay, a solution of FITC-conjugated dextran (0.01 mg/ml, 3kDa, Invitrogen, USA) in cell medium was put in the cell layer, while the collection layer was put in flux at 10 µl/min in order to simulate bloodstream collection of metabolites. The dextran fluorescence in the cell layer was analyzed for 100 min at a confocal microscope (LSM700, Zeiss, Germany) with an incubator mounted on set at 37°C and 5% of $CO_2$, taking an image every two minutes of different positions.

To measure dextran permeability, fluorescence was analyzed using ImageJ image analysis, and each value was compared to the initial value at time 0.

The assay was performed with and without gut bacteria.

### 3.2.7. Claudin and Mucin staining

For the visualization of tight junctions and mucus production, claudin-1 and mucin-2 were stained in the gut-on-chip. Following a PBS wash, a 4% of paraformaldehyde (PAF, Sigma-Aldrich, USA) in PBS was fluxed and allowed to act for 20 minutes. Subsequent to another PBS wash, a solution of 0.1% triton and 3% BSA in PBS was fluxed and allowed to act for 90 minutes at room temperature. The primary antibodies, namely Claudin-1 (1:100, rabbit polyclonal, Abcam, UK) or Mucin-2 (1:100, rabbit recombinant, Abcam, UK) were fluxed in the microfluidic device and allowed to act overnight at 4°C. After a wash in 0.1% Triton, the secondary antibodies (1:500, goat anti-rabbit, Alexa Fluor™ 546, Invitrogen, USA) were fluxed and allowed to act for 90 minutes at room temperature. To include actin fiber staining, phalloidin (1:200, Acti-stain™ phalloidin 488, SIC, Italy) was fluxed, after a 0.1% triton wash, and allowed rest for 1 hour at room temperature. Finally, after another 0.1% Triton wash, Hoechst (1:1000, Thermo Fisher Scientific, USA) was fluxed and allowed to rest for 20 minutes. Each step involved a flow rate of 20 µl/min. The microfluidic device was then washed again with a 2% solution of P/S in PBS and imaged using a confocal microscope (LSM900, Zeiss, Germany).

### 3.2.8. Preparation for SEM image acquisition

For the examination of bacteria and cells using the scanning electron microscope (Ultra plus SEM, Zeiss, Germany) the device was dissected, and the membrane was separated from the PDMS. It was then placed in a well and immersed in a 2.5% glutaraldehyde solution (Gluteraldehyde 25% solution, EM grade distillation purified, Electron Microscopy Sciences, USA) in 0.1 M cacodylate (Sodium cacodylate buffer 0.4 M, pH 7.2,

Electron Microscopy Sciences, USA) overnight at 4°C. Following three washes of 10 min in 0.1 M cacodylate, a 1% osmium solution (Osmium tetroxide 4% aqueous solution, Electron Microscopy Sciences, USA) in 0.1 M cacodylate was applied in the well for 1 hour at 4°C to strengthen and block the biological structures. Subsequently, three 10-min washes in cacodylate were performed. The sequence included washes with ethanol at 10%, 25%, 50% and 70% followed by two washes with ethanol at 80% and 95%, and three washes with 100% ethanol, during which the sample was left until the critical point dryer (EM CPD300, Leica, Germany) procedure.

After drying, samples were placed on the stubs, and metallization was performed using a sputter coater (sputter coater 208-HR, Thickness controller MTM-20, Cressington, UK). The samples were coated with a 20 nm-thick layer of gold.

### 3.2.9. Statistical analysis

Experiments were conducted in triplicates. For bacteria plate count, it was tested in three devices and the plate count was performed by using three spots per each experiment. In the case of FITC-dextran permeability assay, three different microfluidic devices were used. The statistical significance was evaluated with a Welch's T-test. Statistical significance was set as follows: * $p < 0.05$; ** $p < 0.01$; *** $p < 0.001$; **** $p < 0.0001$.

## 3.3. Results

In order to obtain a suitable platform for the study of host-bacteria interactions and drug delivery in the colon, a microfluidic device able to mimic the most important features of human intestine, namely a gut-on-chip, was designed and fabricated.

The device consisted of two channels separated by a polycarbonate membrane. The addition of gold wires in each channel was implemented in order to allow TEER measurements.

Comsol simulations were implemented to investigate the shear stresses that cells will feel. The device was schematized with a 2D geometry composed of an upper and lower layer separated by a cell layer and a porous membrane layer. Two further layers of PDMS were added in order to study oxygen diffusion, which will be discussed later on (**Fig. 3.1 A**). A velocity equal to 2 µl/min was chosen to ensure a shear stress equal to 0.004 $\mathrm{dyne/cm^2}$ at the cell layer (**Fig. 3.1 B-C**). This value is comprised in the typical range of 0.002 – 0.8 $\mathrm{dyne/cm^2}$ present in the human gut[11].

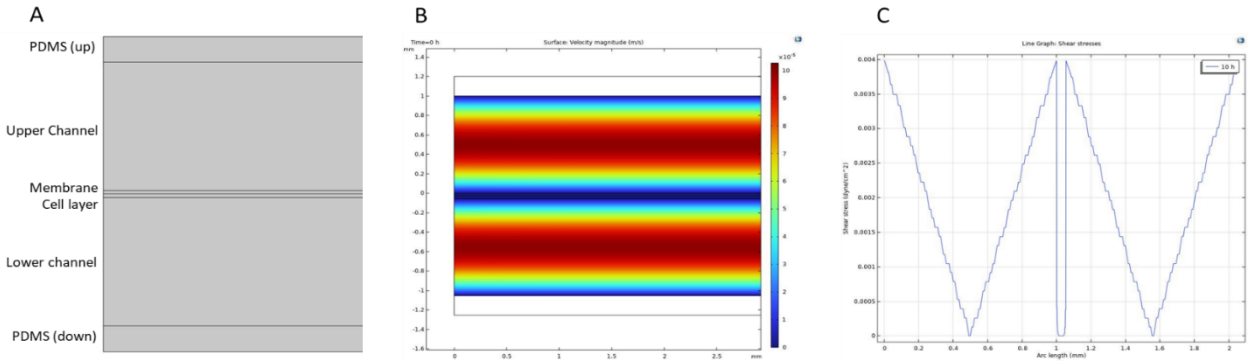


**Figure 3.1.** Geometrical schematization of the device (A). Velocity field inside the channels (B). Shear stresses along the whole device (C). Simulations were made by using Comsol Multiphysicis.

In these experiments the co-culture of cells with anaerobic bacteria is a fundamental aspect. To understand this possibility, Comsol simulations were also used to study oxygen concentration along the two channels in different scenarios. Two cut lines were defined in order to better observe oxygen variation along the lower channel length (**Fig. 3.2 A**) and along the whole device (**Fig. 3.2 B**).

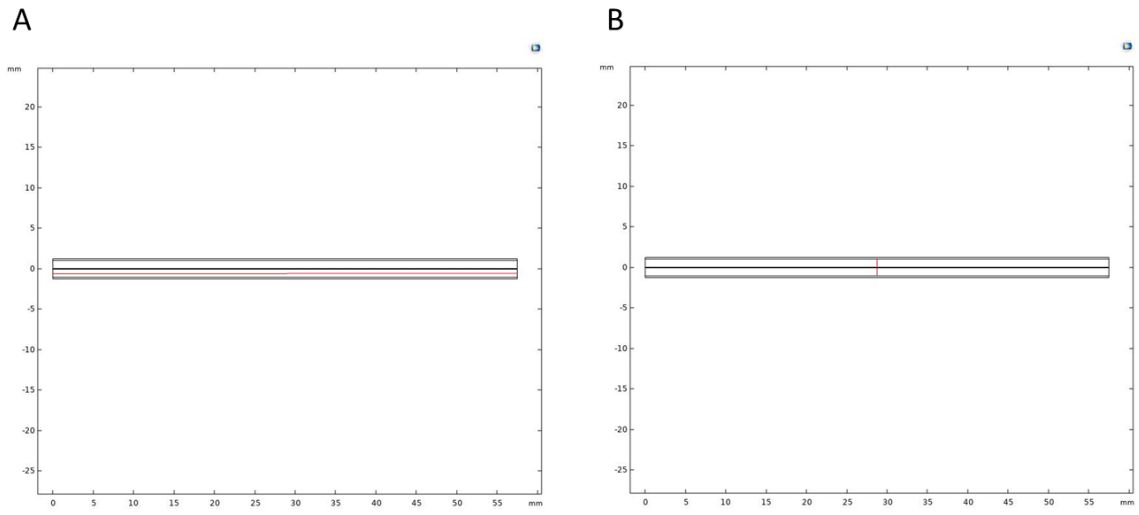


**Figure 3.2.** Cut lines used in the oxygen concentration computation. In the center of the lower (cell) channel (A); in the center of the whole device (B).

We considered a straightforward approach by utilizing deoxygenated medium in the cell-bacteria channel and oxygenated medium in the upper channel to establish an oxygen gradient across the device. However, a substantial challenge arose due to the PDMS high permeability to oxygen, nearly equivalent to that of water. Consequently, even with an oxygen-free medium, the PDMS layer allowed a rapid influx of oxygen, jeopardizing the vitality of anaerobic bacteria. After only 0.4 hours, the oxygen concentration inside the device was almost equal to the external one, especially in the latter part of the lower channel (**Fig. 3.3 A-B-C-D**). Extending the observation to 10 hours, the situation was almost equal, with a substantial portion of the lower

channel registering an oxygen concentration above 0.1 $mol/m^3$ (**Fig. 3.3 E-F-G-H**). Notably, oxygen penetration into the device occurred almost instantaneously, reaching a steady-state swiftly (**Fig. 3.3 I-J**).

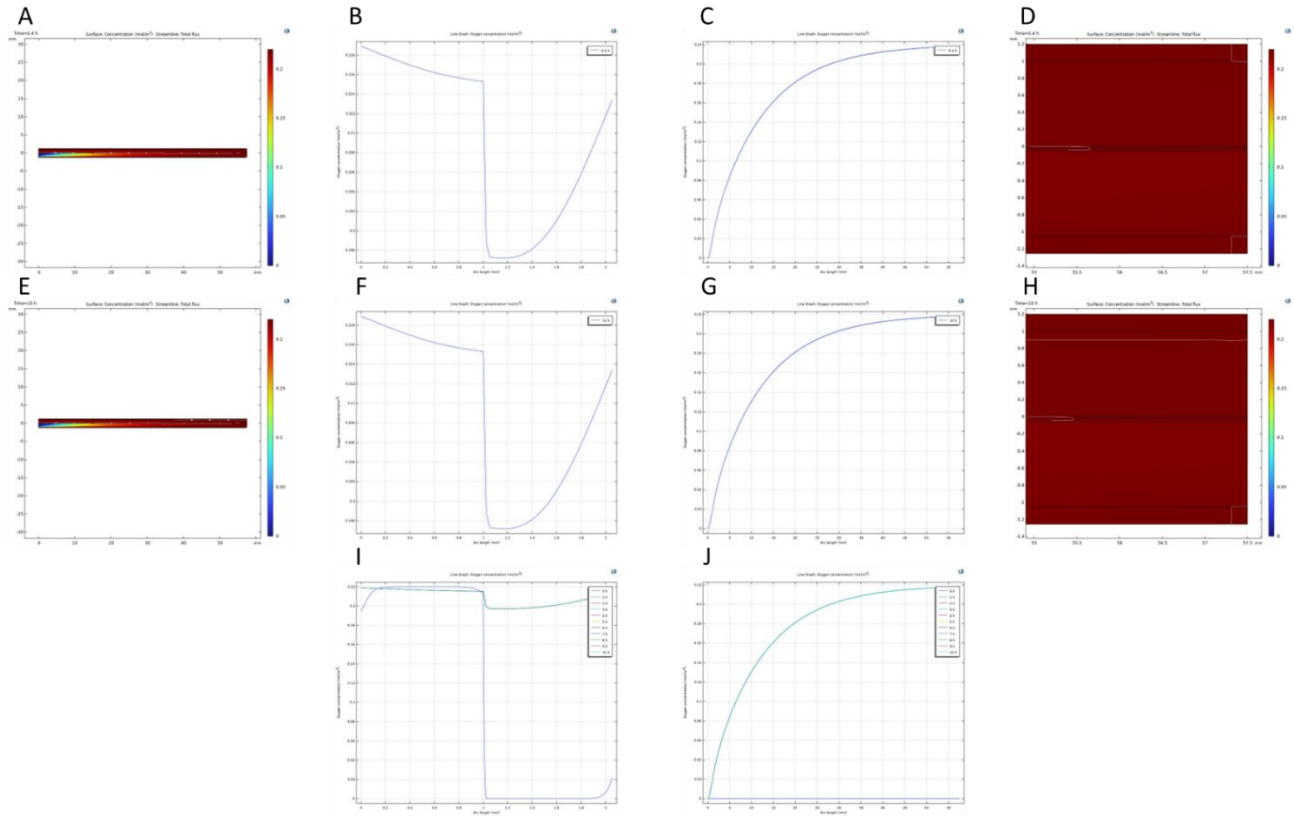


**Figure 3.3.** Comsol Multiphysics simulation of oxygen concentration in the case of oxygen permeable PDMS both in the upper and in the lower part of the device. Oxygen concentration field at 0.4h (A) and 10h (E). Oxygen concentration along the central part of the whole device at 0.4h (B), 10h (F) and its variation in time (I). Oxygen concentration along the central part of the lower channel at 0.4h (C), 10h (G) and its variation in time (J). A zoom of the oxygen concentration field at the end of the device at 0.4h (D) and 10h (H).

To overcome this challenge, we attempted to render the PDMS impermeable to oxygen by introducing a thin layer of glass on the cell channel, being the glass impermeable to oxygen. Despite these efforts, oxygen diffusion remained rapid, reaching a steady state within 0.4 hours. However, leveraging the oxygen consumption by the cells, coupled with the impermeability of glass and the use of a deoxygenated medium in the upper channel, allowed the formation of a proper oxygen gradient along the device. Notably, the maximum oxygen concentration in the lower channel was around 0.04 $mol/m^3$, a value that enables the vitality of anaerobic bacteria (**Fig. 3.4**)[12].

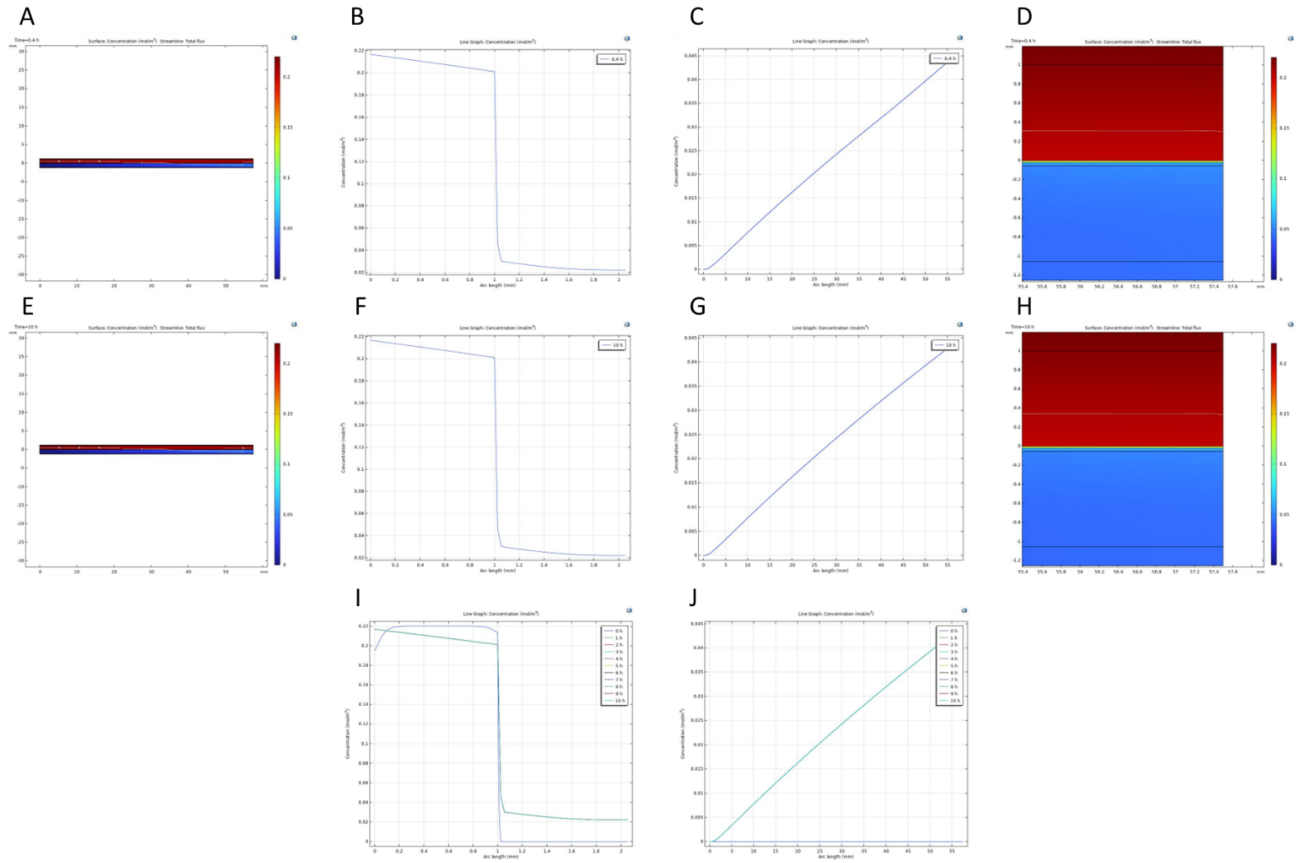


**Figure 3.4.** Comsol Multiphysics simulation of oxygen concentration in the case of oxygen permeable PDMS only in the upper part of the device. Oxygen concentration field at 0.4h (A) and 10h (E). Oxygen concentration along the central part of the whole device at 0.4h (B), 10h (F) and its variation in time (I). Oxygen concentration along the central part of the lower channel at 0.4h (C), 10h (G) and its variation in time (J). A zoom of the oxygen concentration field at the end of the device at 0.4h (D) and 10h (H).

After having ensured the feasibility of co-culturing cells and gut anaerobic bacteria and that the shear stresses remained within a physiological range, we started the culture of Caco-2 cells in the microfluidic device (**Fig. 3.5 B**). TEER measurements showed that within 7 to 10 days, the cells successfully formed a differentiated, complete epithelium under and thanks to the dynamic conditions (**Fig. 3.5 C**). The TEER value at day 8 reached 3.7 $k\Omega * cm^2$, aligning with the typical TEER values of a fully-developed epithelium[13].

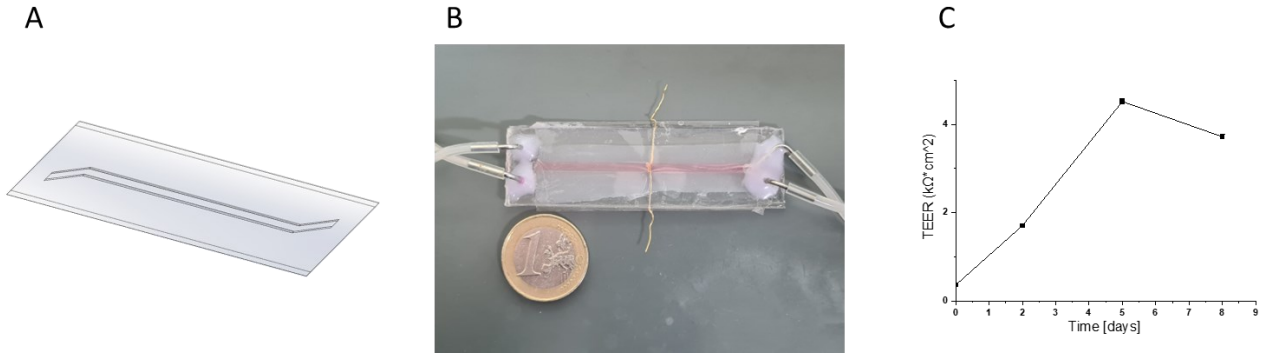


**Figure 3.5.** Schematization of the channels of the device (A). The channels are equal and opposite. Final composition of the device including gold wires (B). TEER measurements at different days of Caco-2 culture (C).

For a comprehensive characterization of the gut-on-chip features, we conducted staining for mucus (Mucin-2) and tight junctions (Claudin-1), that together give information on cell differentiation and correct formation of the epithelium, respectively. Mucus was uniformly spread along the epithelium, with an average thickness of approximately 30 µm (**Fig. 3.6**).

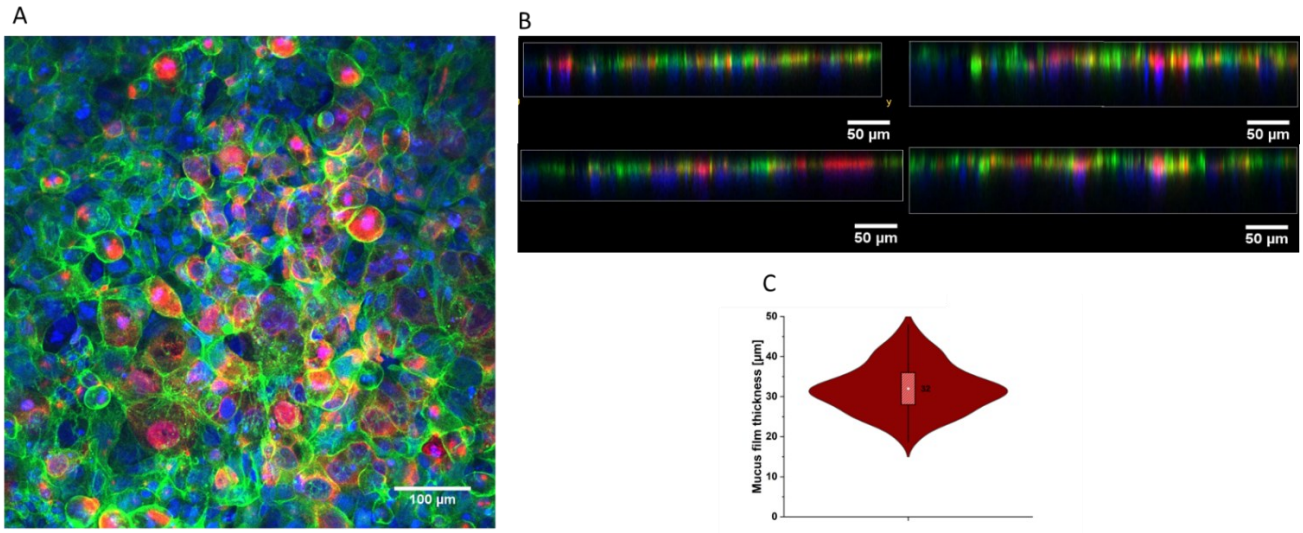


**Figure 3.6.** Immunostaining of cells cultured in the gut-on-chip. Nuclei are stained in blue, actin in green and mucin (MUC-2) in red (A). Different projections of z-stack images (B) used to compute the average mucus thickness (C).

Tight junctions are the first sign of a healthy and integral epithelium. They are fundamental when performing permeability assays since they control the passage of molecules within the epithelium. For this reason, as demonstrated by claudin-1 protein immunostaining, tight junctions exhibited a well-defined web-like structure around the edges of the cells (**Fig. 3.7**).

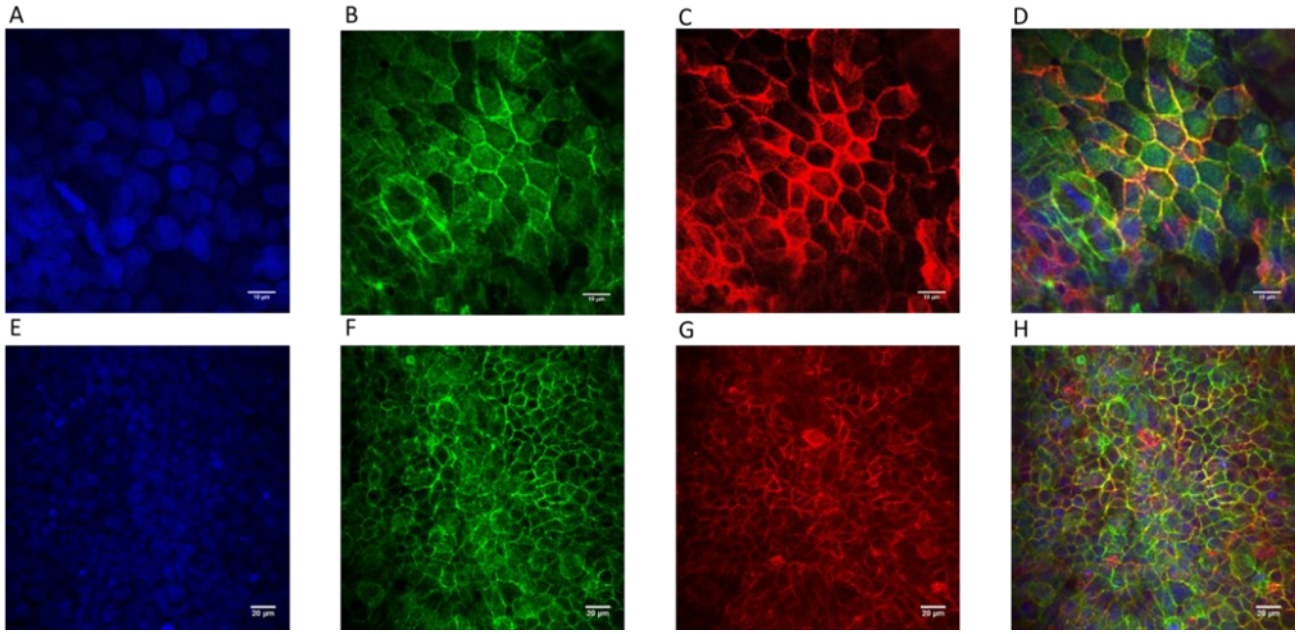


**Figure 3.7.** Immunostaining of the cells cultured in the gut-on-chip. Nuclei are stained in blue (A, E). Actin is stained in green (B, F). Tight junctions (Claudin-1) are stained in red (C, G). Merge of the three channels (D, H).

Once the most important features of the gut-on-chip were validated, we cultured *R. Bromii* inside the cell channel. Live/dead assay and bacteria counts revealed significantly higher growth of *R. Bromii* in the device compared to cultures in an anaerobic hood (**Fig. 3.8 C**). Specifically, the bacteria count reached almost 8 CFU/ml when cultured in the anaerobic hood, whereas it was almost 9 CFU/ml when cultured in the gut-on-chip, indicating a significant difference of about one order of magnitude (p-value < 0.0001). This difference is attributed to the dynamic flow and continuous medium changes, washing out dead bacteria while maintaining the remaining ones in the exponential growth phase.

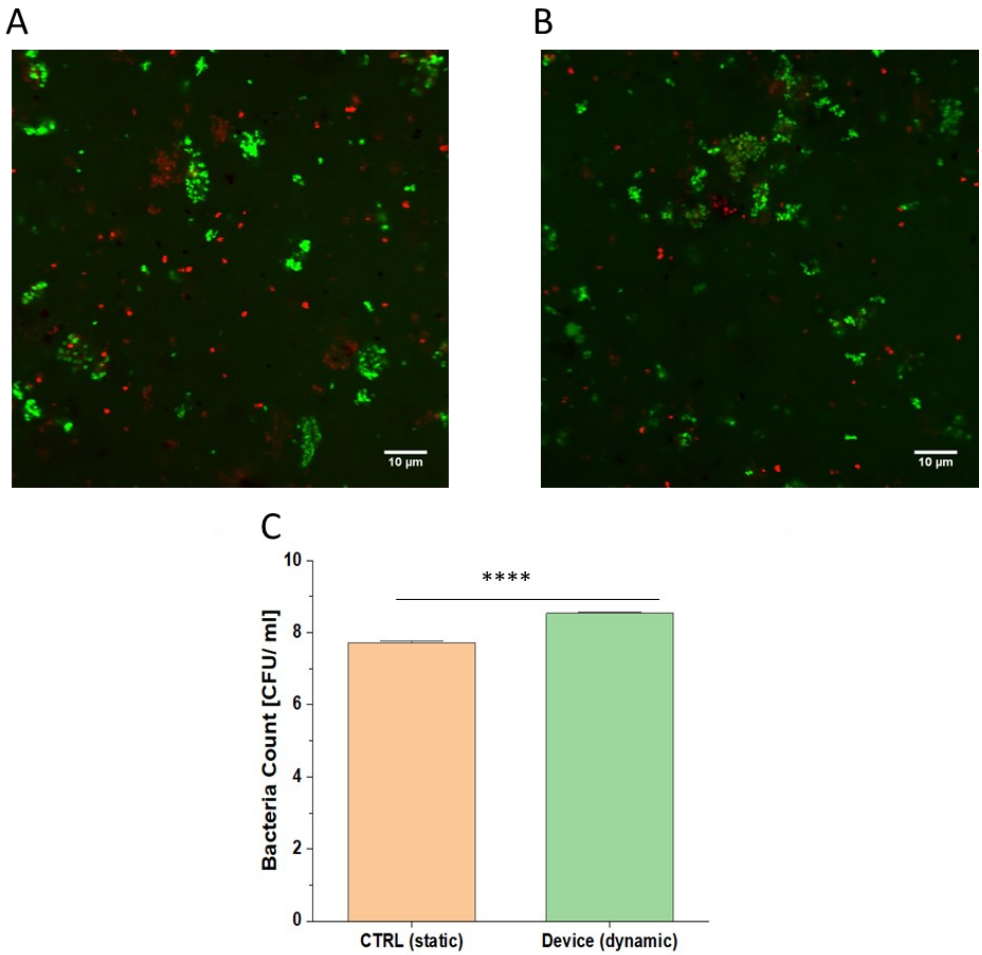


**Figure 3.8.** Live (green) /dead (red) staining of *R. Bromii* after 72h of static culture in the anaerobic incubator (A) and after 72h of dynamic culture in the gut-on-chip (B). Bacteria count (in log scale) comparison between *R. Bromii* cultured in dynamic (gut-on-chip) or static (anaerobic incubator) conditions after 72h. (**** p-value < 0.0001; n = 3 plates for 3 different experiments).

Subsequently, SEM was utilized to further illustrate the key features of the microfluidic device, including villi formation (**Fig. 3.9 A-B**), mucus production (**Fig. 3.9 C-D**) and host-bacteria interaction. The study considered anaerobic bacteria only (**Fig. 3.9 E-F**) and a mixture of anaerobic and aerobic bacteria (**Fig. 3.9 G-H**) to demonstrate the possibility of co-culturing different bacterial species in the gut-on-chip.

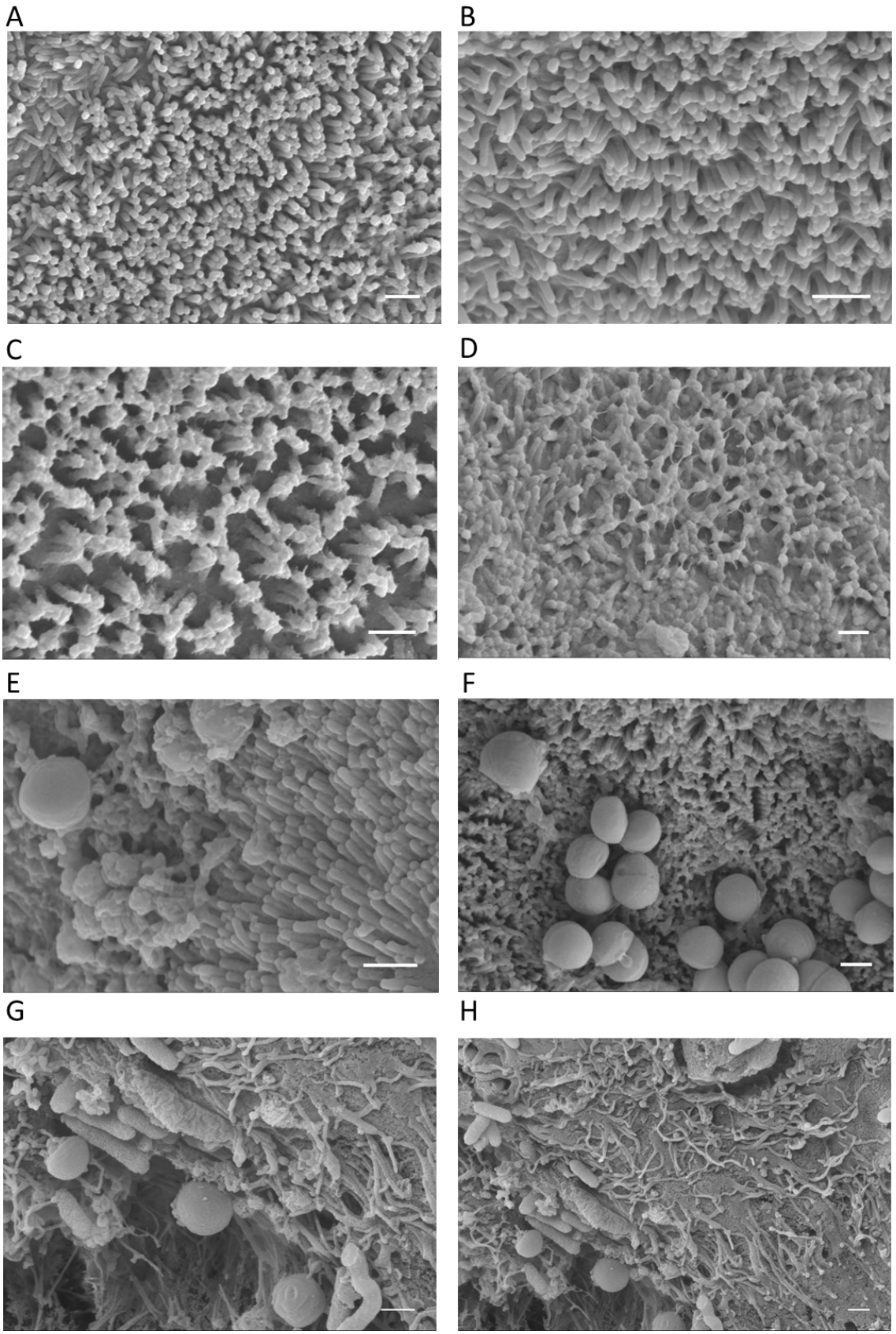


**Figure 3.9.** SEM images of cells and bacteria cultured in dynamic conditions in the gut-on-chip. Villi structures (A, B). Mucus production on the villi structures (C, D). *R. Bromii* culture in the gut-on-chip (E, F). *R. Bromii* and *L. Rhamnosus* co-culture in the gut-on-chip (G, H). Scale bar is 500 nm.

Finally, a dextran permeability assay was conducted to assess the potential use of the platform as a drug screening tool. Initially performed with only Caco-2 cells cultured in the microfluidic device (**Fig. 3.10**), the dextran passage exhibited an initial burst absorption followed by a sustained absorption after circa 40 min. At 100 min, the total dextran absorbed reached around 35%.

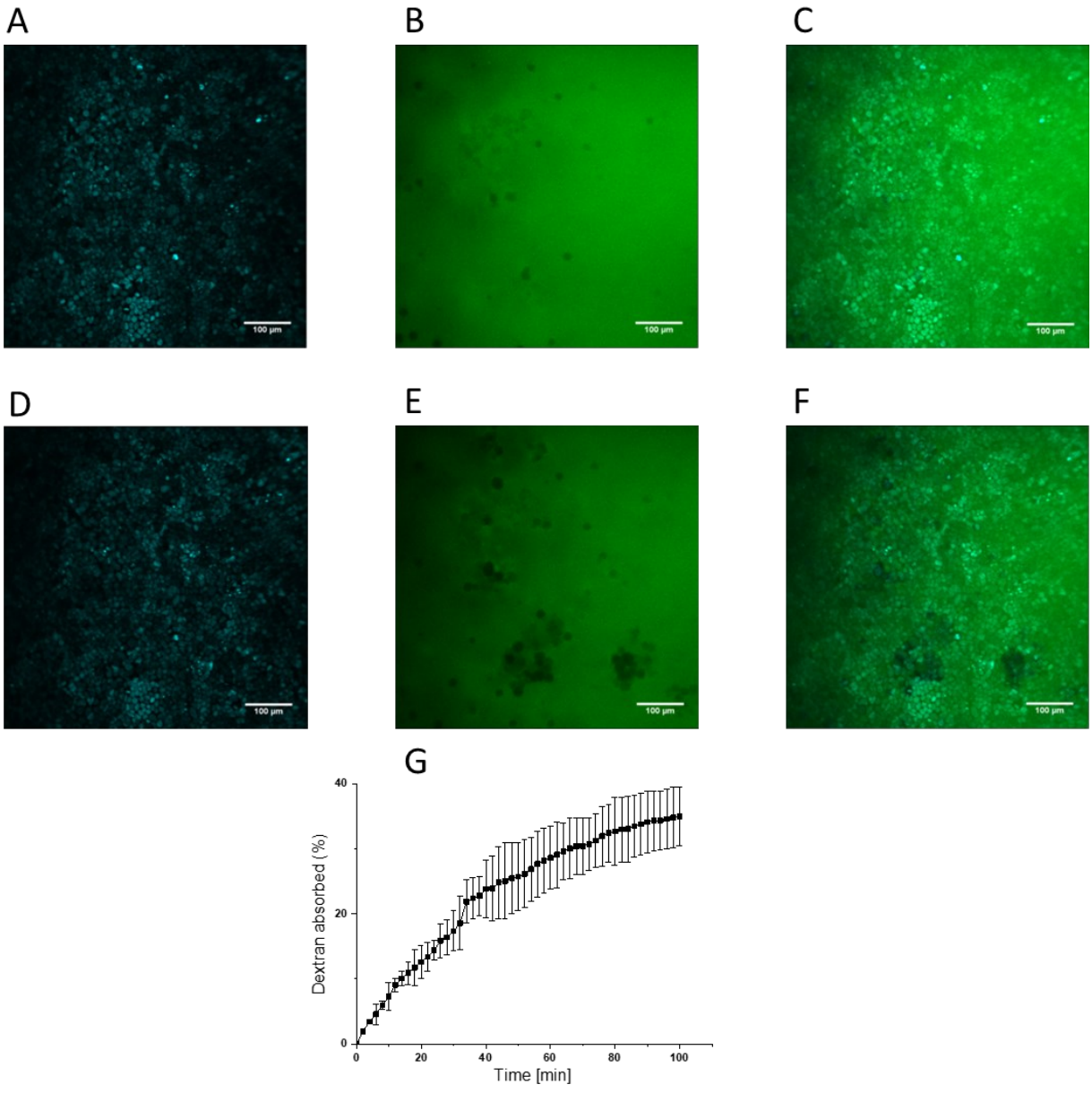


**Figure 3.10.** 3 kDa fluorescent dextran (green) permeability assay of Caco-2 cells cultured in the gut-on-chip. Nuclei were stained with Hoechst (blue). Nuclei at 0 min (A) and 100 min (D). Dextran intensity at 0 min (B) and at 100 min (E). Merge of the two channels at 0 min (C) and 100 min (F). Dextran absorbed in the collection chamber computed as difference in dextran fluorescence over time (G) (n = 3 microfluidic devices).

Then, the same experiment was repeated with the addition of *R. Bromii*. While maintaining a similar absorption curve pattern with an initial burst followed by a sustained absorption, the presence of bacteria introduced a

delay in the absorption. This accounts for the final percentage of dextran absorption, which was approximately 20% at 100 min.

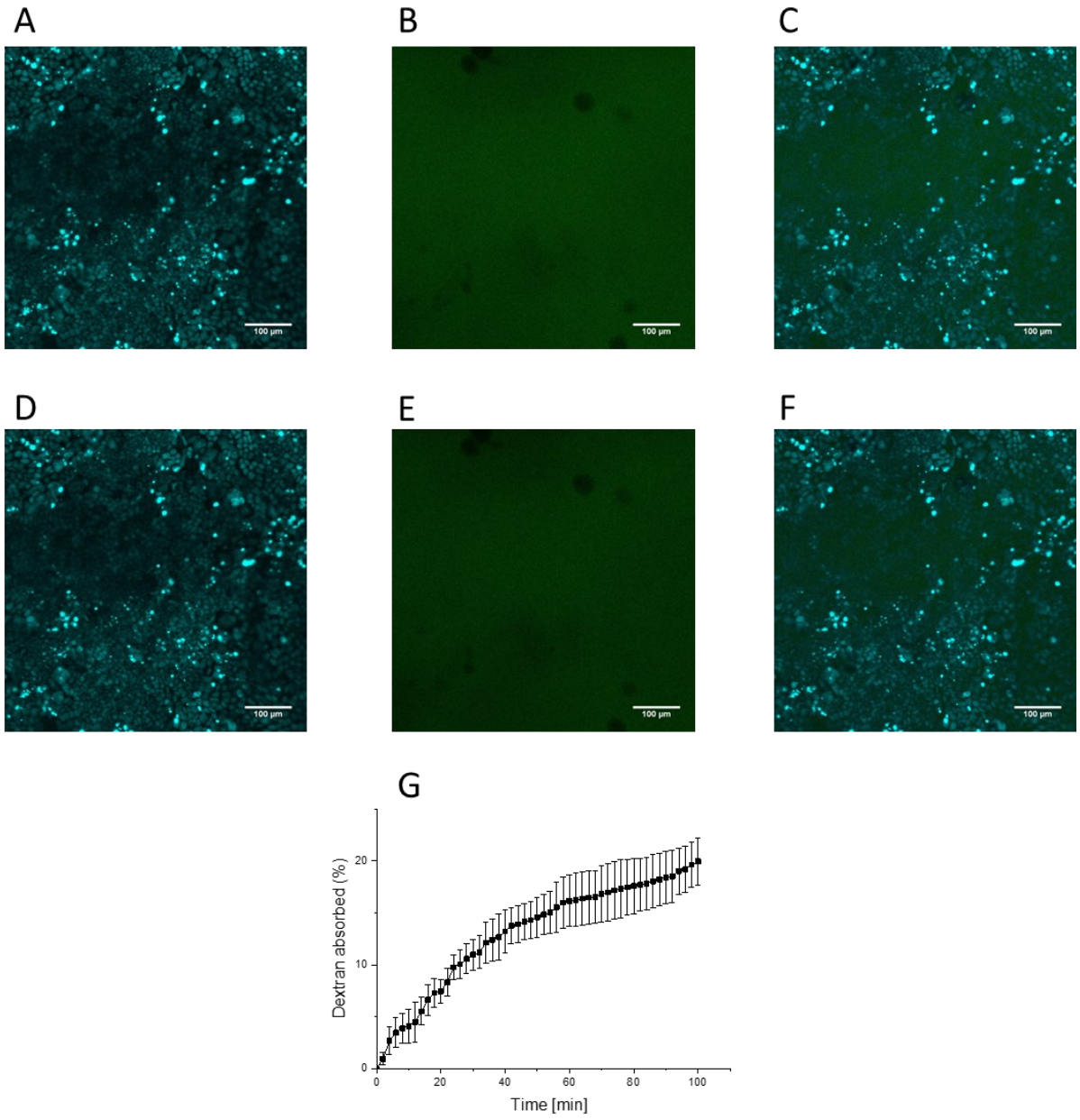


**Figure 3.11.** 3 kDa fluorescent dextran (green) permeability assay of Caco-2 cells and *R. Bromii* cultured in the gut-on-chip. Nuclei were stained with Hoechst (blue). Nuclei at 0 min (A) and 100 min (D). Dextran intensity at 0 min (B) and at 100 min (E). Merge of the two channels at 0 min (C) and 100 min (F). Dextran absorbed in the collection chamber computed as difference in dextran fluorescence over time (G) (n = 3 microfluidic devices).

## 3.4. Discussion

We developed a platform that successfully replicates major features of the intestine. Caco-2 cells, typically unable to produce mucus in static conditions, demonstrated mucus production in response to physiological shear stresses capable to promote their differentiation and therefore mucus production. The observed mucus

layer of around 30 μm compares favorably with the strongly adherent mucus thickness of 50 μm found in the colon[14]. The lower thickness may be due to the loss of looser mucus during the various washing processes typical of immunostaining. SEM images further confirmed the presence of mucus which is fundamental for its function of physical barrier against bacterial infections. Speaking of bacteria, most of the ones present in the gut have a mucin-binding-protein, so the presence of mucus allow their anchor inside the gut-on-chip[15]. This means that the presence of mucus is essential and in our microfluidic device its production is almost comparable to the *in-vivo* one.

TEER measurements and claudin immunostaining collectively verified the formation of well-defined tight junctions, crucial for permeability tests. In fact, tight junctions are the first barrier to passive passage from one side to the other of the epithelium. They play a major role in barrier integrity and functionality[16]. Their disfunction or under expression could result in diseases, so they are also a first feature that should be considered when studying a disease model[17]. For all these reasons, having well-formed and packed tight junctions is crucial to have a performant drug screening platform.

In addition, SEM showed the presence of villi-like structures indicating cellular differentiation and polarization that enhances the surface area for absorption, rendering the platform even closer to the *in-vivo* situation. Their presence gave to the whole system a sort of 3D structure. Furthermore, villi play an essential role in host-bacteria interaction and in diseased model, as their shape can be influenced by inflammation[18].

After confirming the presence of fundamental intestinal features within the microfluidic device, we tested its ability in culturing anaerobic bacteria. To this aim, we first performed a Comsol simulation to address the pronounced permeability of PDMS to oxygen. The simulations suggested that incorporating a thin glass layer on the cell channel could substantially reduce the presence of oxygen by almost one order of magnitude, ensuring anaerobic bacteria vitality. Subsequently, we tested this hypothesis by co-culturing *R. Bromii* alongside the cells in the same channel. While this choice introduced additional complexity to the design of the device, requiring both cells and bacteria to grow in the same channel, it offered a more cohesive host-bacteria interaction. This approach eliminated the delay typically encountered when bacteria metabolites pass from a bacteria layer to a cell layer, as demonstrated by other research groups[9]. In our case, metabolites were readily available for cells and could pass into the collection channel. The concept of rendering PDMS impermeable by adding a thin layer of glass was straightforward yet effective, supporting the formation of an oxygen gradient conducive to the growth of *R. Bromii.* This was further validated through bacteria count experiments and SEM images. Furthermore, the generated oxygen gradient within the gut-on-chip facilitates the culture of diverse bacteria species, including anaerobic organisms like *R. Bromii* or microaerophilic as *L. Rhamnosus*. This versatility enhances the platform's applicability for studying various host-microbe interactions.

Overall, our approach not only addressed the challenges associated with PDMS permeability, but also demonstrated the successful co-culture of cells and anaerobic bacteria in a shared channel. This innovative design ensures a more realistic representation of host-bacteria dynamics within the microenvironment.

Two permeability assays using 3 kDa fluorescent dextran, one with only cells and the other together with bacteria, were conducted for platform validation. The addition of bacteria introduced resistance to dextran diffusion delaying its passage as compared to the device bacteria-free. This could be attributed to the interaction of the bacteria with the epithelium, as commensal bacteria are known to enhance the properties of the barrier. In fact, *in vivo* studies have been shown that the presence of commensal bacteria diminishes gut permeability by interacting at the mucus level and influencing the overall barrier structure[19–21]. This observation can be directly translated to our case, where the addition of commensal bacteria further improves gut permeability.

## 3.5. Conclusion

This study presents the successful development of a microfluidic platform capable of mimicking crucial features of the human gut, from villi and epithelium formation (in the shape of tight junction) to mucus production and host-bacteria co-culture, even in anaerobic conditions. Such gut-on-chip holds promise as a robust drug screening platform. By avoiding the need for animal experimentation, it offers a cost-effective alternative for drug assessment. Additionally, the device may involve immune system cells to investigate their role in case of inflammation or infection.

In the next chapter, we will utilize this platform to conduct absorption and inflammation studies, and to assess the action of the proposed starch O/W emulsion.

## 3.6. Bibliography


1. Leung, C. M. *et al.* A guide to the organ-on-a-chip. *Nat. Rev. Methods Primer* **2**, 33 (2022).

2. Ingber, D. E. Human organs-on-chips for disease modelling, drug development and personalized medicine. *Nat. Rev. Genet.* **23**, 467–491 (2022).

3. Sung, J. H. *et al.* Recent Advances in Body-on-a-Chip Systems. *Anal. Chem.* **91**, 330–351 (2019).

4. Cresci, G. A. M. & Izzo, K. Gut Microbiome. in *Adult Short Bowel Syndrome* 45–54 (Elsevier, 2019). doi:10.1016/B978-0-12-814330-8.00004-4.

5. Marrero, D. *et al.* Gut-on-a-chip: Mimicking and monitoring the human intestine. *Biosens. Bioelectron.* **181**, 113156 (2021).

6. Beaurivage, C. *et al.* Development of a human primary gut-on-a-chip to model inflammatory processes. *Sci. Rep.* **10**, 21475 (2020).

7. Marr, E. E. *et al.* A platform to reproducibly evaluate human colon permeability and damage. *Sci. Rep.* **13**, 8922 (2023).

8. Fois, C. A. M., Schindeler, A., Valtchev, P. & Dehghani, F. Dynamic flow and shear stress as key parameters for intestinal cells morphology and polarization in an organ-on-a-chip model. *Biomed. Microdevices* **23**, 55 (2021).

9. Eain, M. M. G. *et al.* Engineering Solutions for Representative Models of the Gastrointestinal Human-Microbe Interface. *Engineering* **3**, 60–65 (2017).

10. Jalili-Firoozinezhad, S. *et al.* A complex human gut microbiome cultured in an anaerobic intestine-on-a-chip. *Nat. Biomed. Eng.* **3**, 520–531 (2019).

11. Thomas, D. P., Zhang, J., Nguyen, N.-T. & Ta, H. T. Microfluidic Gut-on-a-Chip: Fundamentals and Challenges. *Biosensors* **13**, 136 (2023).

12. Espey, M. G. Role of oxygen gradients in shaping redox relationships between the human intestine and its microbiota. *Free Radic. Biol. Med.* **55**, 130–140 (2013).

13. Kim, H. J., Huh, D., Hamilton, G. & Ingber, D. E. Human gut-on-a-chip inhabited by microbial flora that experiences intestinal peristalsis-like motions and flow. *Lab. Chip* **12**, 2165 (2012).

14. Johansson, M. E. V., Larsson, J. M. H. & Hansson, G. C. The two mucus layers of colon are organized by the MUC2 mucin, whereas the outer layer is a legislator of host–microbial interactions. *Proc. Natl. Acad. Sci.* **108**, 4659–4665 (2011).

15. Mark Welch, J. L., Hasegawa, Y., McNulty, N. P., Gordon, J. I. & Borisy, G. G. Spatial organization of a model 15-member human gut microbiota established in gnotobiotic mice. *Proc. Natl. Acad. Sci.* **114**, (2017).

16. Saeedi, B. J. *et al.* HIF-dependent regulation of claudin-1 is central to intestinal epithelial tight junction integrity. *Mol. Biol. Cell* **26**, 2252–2262 (2015).

17. Barmeyer, C., Schulzke, J. D. & Fromm, M. Claudin-related intestinal diseases. *Semin. Cell Dev. Biol.* **42**, 30–38 (2015).

18. Ritchie, J. M. *et al.* Inflammation and Disintegration of Intestinal Villi in an Experimental Model for Vibrio parahaemolyticus-Induced Diarrhea. *PLoS Pathog.* **8**, e1002593 (2012).

19. Jakobsson, H. E. *et al.* The composition of the gut microbiota shapes the colon mucus barrier. *EMBO Rep.* **16**, 164–177 (2015).

20. Ohland, C. L. & MacNaughton, W. K. Probiotic bacteria and intestinal epithelial barrier function. *Am. J. Physiol.-Gastrointest. Liver Physiol.* **298**, G807–G819 (2010).

21. Yoshida, N. *et al. Bacteroides vulgatus* and *Bacteroides dorei* Reduce Gut Microbial Lipopolysaccharide Production and Inhibit Atherosclerosis. *Circulation* **138**, 2486–2498 (2018).

# 4. Starch emulsion as absorption and inflammation reducer: testing in the gut-on-chip

## 4.1. Introduction

Obesity is recognized as the new millennium pandemic[1]. As said in a previous chapter, one of the main differences between healthy and obese subjects is the composition of gut microflora, with obese patients having a higher *Firmicutes* to *Bacteroidetes* ratio[2]. However, other significant differences should be considered. For example, obese patients suffer from chronic inflammation of the intestine, which over time could lead to more severe diseases, as colorectal cancer[3,4]. This chronic inflammation is correlated to dysbiosis and to an altered absorption of nutrients, leading to a distorted sense of satiety. In fact, a more leaky intestine is connected to a different expression of claudins and occludins, proteins that form the cellular junctions[5]. In details, in cases of inflammation and obesity, claudin-1 is downregulated, while claudin-2 is upregulated, especially at the colon level. This, connected with the increased production of SCFAs by the overrepresented *Firmicutes* population, leads to an increase in body weight over time[6]. Along with more pronounced caloric absorption, the sense of satiety also plays a predominant role. Interestingly, obese patients have hormonal dysfunction, which comprises lower sensitivity to CCK, leading to higher energy intake[7].

Our strategy aims to treat obesity by acting at different levels. Firstly, as previously demonstrated, we tried to restore a physiological gut microflora by quenching the activity of overrepresented bacteria (*R. Bromii*), while not affecting other normally present species (*L. Rhamnosus*). Then, experiments were conducted to reduce intestinal permeability and the consequent nutrient absorption in the gut-on-chip. In a first attempt, an O/W macroemulsion without a surfactant was used to observe the role of the oil alone. After that, the starch emulsion was implemented by co-culturing *R. Bromii*. Finally, inflammation was studied by using LPS in the microfluidic device. The reduction in inflammatory status was evaluated by ROS levels and claudin-1 expression and was associated with *R. Bromii* presence and cur-loaded starch emulsion treatment.

## 4.2. Materials and Methods

### 4.2.1. MTT Vitality Test

To assess cell viability, an MTT test was conducted. In details, Caco-2 cells were cultured in a 96-well plate with each condition, including the control, performed in triplicates. The day after, a solution in cell medium of various emulsions was applied to the cells for 2 hours at 37°C in the incubator. After that, the solution was washed with PBS to simulate wash-out and the solution was replaced by cell medium. After 24 and 48 hours from the initial contact, MTT powder (Thyazolyl blue tetrazolium bromide, Sigma, USA) was dissolved in cell medium (0.5 mg/ml), filtered to eliminate possible particulates and exposed to the cells for 3 hours at 37°C in the incubator. After removing the supernatant, 2-Propanol was used to dissolve crystals and it was left to act

for 20 min. Finally, a plate-reader (EnSpire multimode plate reader, Perkin Elmer, USA) at 570 nm was used. To obtain the viability percentage value, the emission of each well was compared with the control.

### 4.2.2. Oil macroemulsion production

A commercially available microfluidic device (Dolomite junction chip, Dolomite, UK) with a T junction was used to produce oil macroemulsions and the oil (soybean oil, Sigma-Aldrich, USA) and water (MilliQ) phase were perfused at different flow rates and the macroemulsion size was measured using a microscope with a camera (Olympus, Japan). The particle size was computed through ImageJ, with the chosen flow rates ensuring the smallest oil macroemulsion size without exceeding a total flow rate of100 µl/min.

### 4.2.3. Fluorescein isothiocyanate (FITC)-dextran permeability assay for macroemulsion

For the permeability assay, a solution of FITC-conjugate dextran (0.01 mg/ml, 3kDa, Invitrogen, USA) in cell medium was applied to the cell layer, while the collection layer fluxed at 10 µl/min to simulate bloodstream collection of metabolites. Dextran fluorescence in the cell layer was analyzed for 100 min using a confocal microscope (LSM700, Zeiss, Germany) within an incubator set at 37°C and 5% of $CO_2$ and taking an image every two minutes at different positions.

In case of the oil macroemulsions, the dextran solution served as the water phase. After that the experiment, PBS was fluxed to simulate wash-out, eliminating dextran and then the experiment was carried out again using cell culture medium. This was repeated for two times. These experiments were performed without the addition of gut bacteria. After two days of dynamic culture, the permeability assay was repeated and fluorescence was compared to the initial value at time 0.

In case of starch emulsion, *R. Bromii* was added to the cell layer as mentioned before. After 1 day of cell-bacteria co-culture, the starch emulsion was diluted in cell culture medium without P/S (1:12.5) and perfused inside the cell layer for 2 hours. After that, the experiment was conducted as stated above, using dextran dissolved in cell culture medium without P/S, by putting the collection channel in flux at 10 µl/min and acquiring images every two minutes. Then, PBS was fluxed and the experiment was repeated for two times.

### 4.2.4. Inflammation in the gut-on-chip

Lipopolysaccharide (LPS, Sigma-Aldrich, USA) was used to induce intestinal inflammation. In details, a solution of 15 µg/ml of LPS was applied the cell layer for 4 hours in the incubator. After that, PBS was used for washing and a ROS assay (Fluorometric intracellular ROS kit, Sigma-Aldrich, USA) was performed. Briefly, 1 µl of ROS detector was added to 500 µl of cell medium and the solution was put in contact with the cell layer for 1 hour at 37°C. Then, after a PBS washing, a confocal microscope (LSM700, Leica, Germany) was used to evaluate the ROS presence. To compute the ROS concentration, the images were analyzed with Imagej. For the control case, only the ROS detector was used, without LPS contact.

To evaluate the anti-inflammatory capacity of emulsions, after adding the LPS solution, the cur-loaded emulsion was perfused inside the gut-on-chip and left to rest for 2 hours at 37°C in an humified incubator. This was done in the presence or absence of *R. Bromii*.

### 4.2.5. Tight junction staining

For the visualization of tight junctions, claudin-1 was stained in a gut-on-chip that underwent inflammation and in another one that was inflamed and treated with the cur-loaded starch emulsion, following the same procedure. Following a PBS wash, a 4% of paraformaldehyde (PAF, Sigma-Aldrich, USA) in PBS was fluxed and allowed to act for 20 minutes. Subsequent to another PBS wash, a solution of 0.1% triton and 3% BSA in PBS was fluxed and allowed to act for 90 minutes at room temperature. Claudin-1 (1:100, rabbit polyclonal, Abcam, UK) was fluxed into the microfluidic device and allowed to act overnight at 4°C. After a wash in 0.1% Triton, the secondary antibody (1:500, goat anti-rabbit, Alexa Fluor™ 647, Invitrogen, USA) was fluxed and allowed to act for 90 minutes at room temperature. To include actin fiber staining, phalloidin (1:200, Acti-stain™ phalloidin 488, SIC, Italy) was fluxed after a 0.1% triton wash, and allowed to rest for 1 hour at room temperature. Finally, after another 0.1% Triton wash, Hoechst (1:1000, Thermo Fisher Scientific, USA) was fluxed and allowed to rest for 20 minutes. Each step involved a flow rate of 20 µl/min. The microfluidic device was then washed again with a 2% solution of P/S in PBS and imaged using a confocal microscope (LSM900, Zeiss, Germany).

### 4.2.6. Preparation for SEM image acquisition

For the examination of villi conformation after inflammation and after the treatment with cur-loaded starch emulsion, the scanning electron microscope (Ultra plus SEM, Zeiss, Germany) was used. To prepare the samples, the device was dissected, and the membrane was separated from the PDMS. It was then placed in a well and immersed in a 2.5% glutaraldehyde solution (Gluteraldehyde 25% solution, EM grade distillation purified, Electron Microscopy Sciences, USA) in 0.1 M cacodylate (Sodium cacodylate buffer 0.4 M, pH 7.2, Electron Microscopy Sciences, USA) overnight at 4°C. Following three washes of 10 minutes in 0.1 M cacodylate, a 1% osmium solution (Osmium tetroxide 4% aqueous solution, Electron Microscopy Sciences, USA) in 0.1 M cacodylate was applied in the well for 1h at 4°C to strengthen and block the biological structures. Subsequently, three 10-minute washes in cacodylate were performed. The sequence included washes with ethanol at 10%, 25%, 50% and 70% followed by two washes with ethanol at 80% and 95%, and three washes with 100% ethanol, during which the sample was left until the critical point dryer (EM CPD300, Leica, Germany) procedure.

After drying, samples were placed on the stubs, and metallization was performed using a sputter coater (sputter coater 208-HR, Thickness controller MTM-20, Cressington, UK). The samples were coated with a 20 nm-thick layer of gold.

### 4.2.7. Statistical analysis

Experiments were conducted in triplicates. In the case of FITC-dextran permeability assay, three different microfluidic devices were used. For ROS levels and claudin-1 fluorescent intensity three different microfluidic devices were used for each condition and different zones were analyzed for each device. The statistical significance was evaluated with a Welch's T-test. Statistical significance was set as follows: * $p < 0.05$; ** $p < 0.01$; *** $p < 0.001$; **** $p < 0.0001$.

## 4.3. Results

Once demonstrated that the microfluidic platform successfully replicated essential features of the human intestine (villi, mucus and tight junctions), we proceeded to assess whether our idea of using oil as an absorption reducer was correct. For this purpose, we used a commercially available microfluid device (T junction) to produce an O/W macroemulsion. Various flow rates of oil and water were tested, and the average particles size was computed using a camera mounted on a microscope (**Fig. 4.1**). As expected, an increase in the flow rate of the aqueous phase led to a decrease in particle size. The emulsion size was around 300 µm for each formulation, except for the one obtained by setting a flow rate of 10 µl/min for the oil phase and 100 µl/min for the water phase. However, such a flow rate could be dangerous for cells. For this reason, we opted for the formulation with a flow rate of 10 µl/min for the oil phase and 70 µl/min for the water phase. The difference in size with other formulation is not significant and the overall flow rate remains within a range that does not harm cells. We deliberately avoided the use of a surfactant, as our goal was not to achieve a stable emulsion but to release the oil onto the epithelium as quickly as possible.

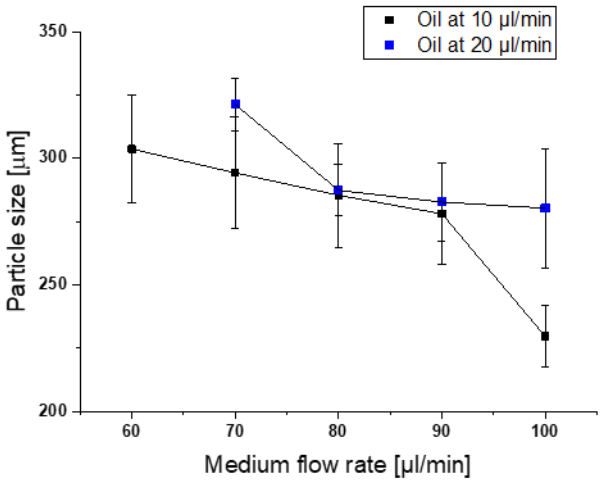


**Figure 4.1.** Particle size of the oil-in-water emulsion obtained by T junction varying the flow rates of the oil and water phases.

Once we identified the optimal macroemulsion formulation, we performed a dextran permeability assay. Initially, we connected the two microfluidic devices, i.e., the T junction and the gut-on-chip in series, so that the macroemulsion was directly fluxed into the gut-on-chip. In this setup, we used the dextran dissolved in the cell culture medium as the water phase. After ensuring the emulsion covered the whole surface of the device,

we stopped the flux in the cell layer and initiated the confocal analysis (**Fig. 4.2 C**). Then, we washed the system with PBS and repeated the experiment two more times (**Fig. 4.2 D**).

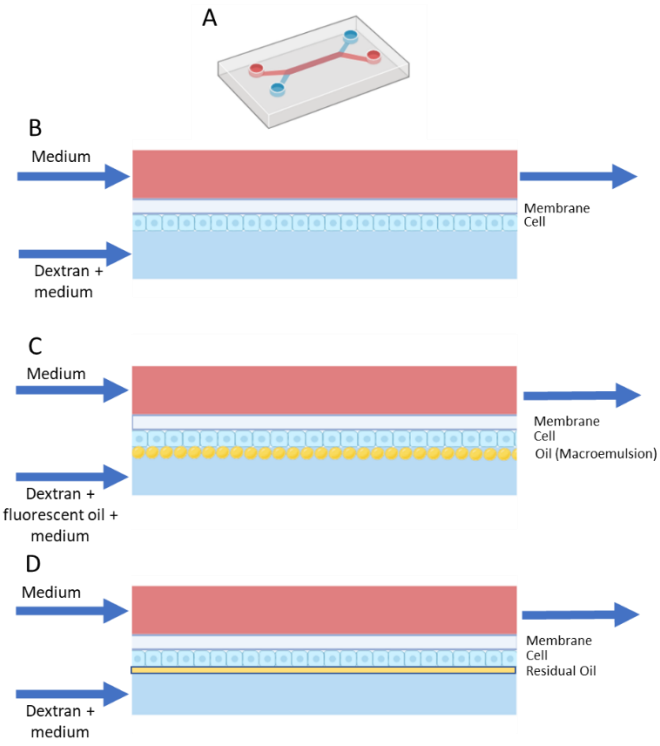


**Figure 4.2.** Schematization of the dextran permeability assay performed with the oil-in-water macroemulsion. Schematization of the gut-on-chip (A). Schematization of the control experiment (without macroemulsion) (B). Schematization of the experiment after the addition of the macroemulsion (C). Schematization of the experiment after the PBS washing (D). In each experiment the flow rate of the collection channel was equal to 10 µl/min and the images were acquired for 100 min.

In details, immediately after adding the macroemulsion, the dextran absorption exhibited an almost linear trend through the entire observation period (**Fig. 4.3**). The presence of oil, in the form of O/W macroemulsion, could have hindered the absorption, resulting in approximately 7.68% after 100 min.

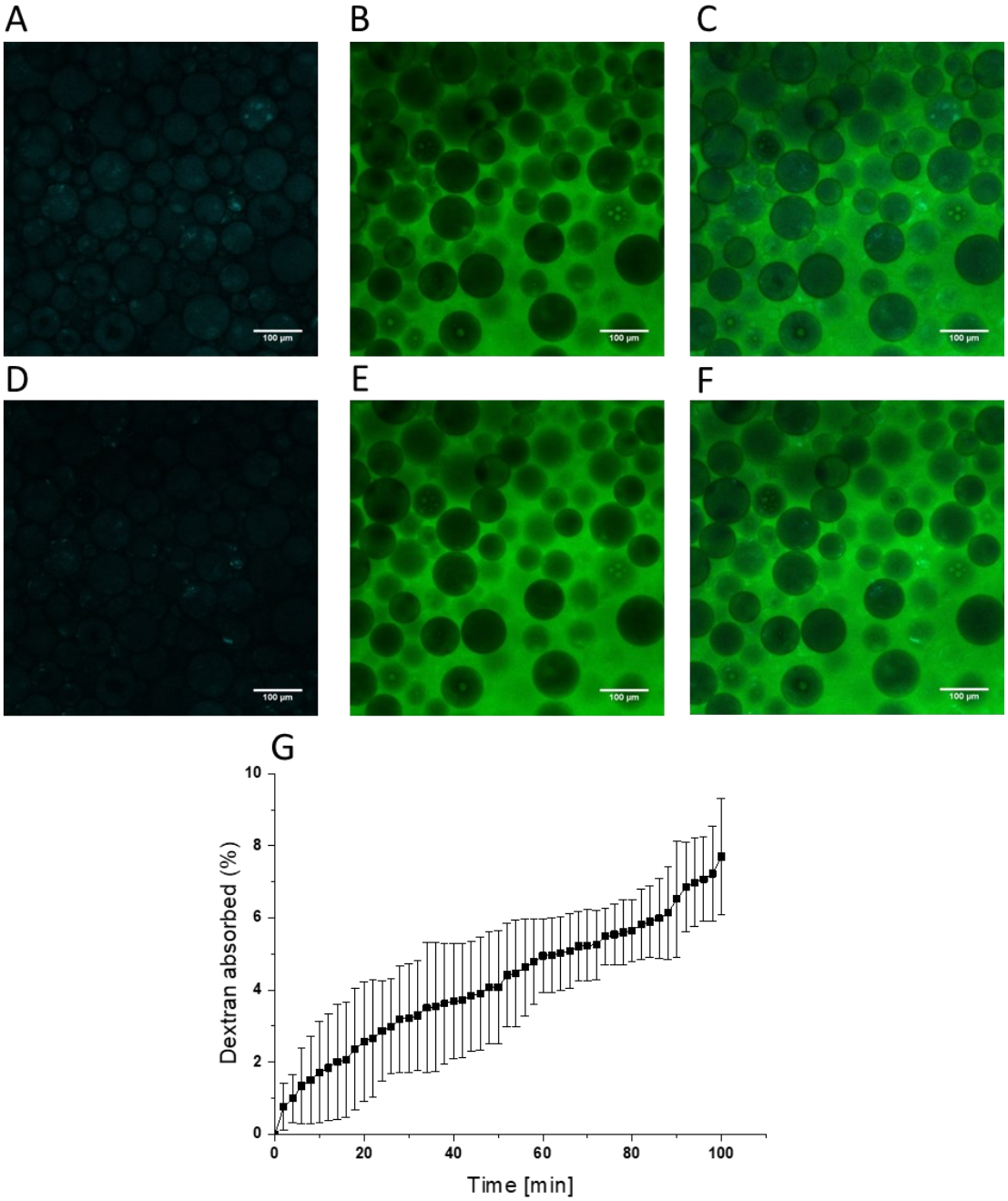


**Figure 4.3.** 3 kDa fluorescent dextran (green) permeability assay of Caco-2 cells cultured in the gut-on-chip in contact with the oil macroemulsion. Nuclei were stained with Hoechst (blue). Nuclei at 0 min (A) and 100 min (D). Dextran intensity at 0 min (B) and at 100 min I. Merge of the two channels at 0 min (C) and 100 min (F). Dextran absorbed in the collection chamber computed as difference in dextran fluorescence over time (G) (n = 3 microfluidic devices).

After the first wash with PBS, the absorption curve had an initial burst absorption, up to 20 min, then the absorption rate decreased (**Fig. 4.4**). The overall absorption at 100 min was equal to ca. 13.6%.

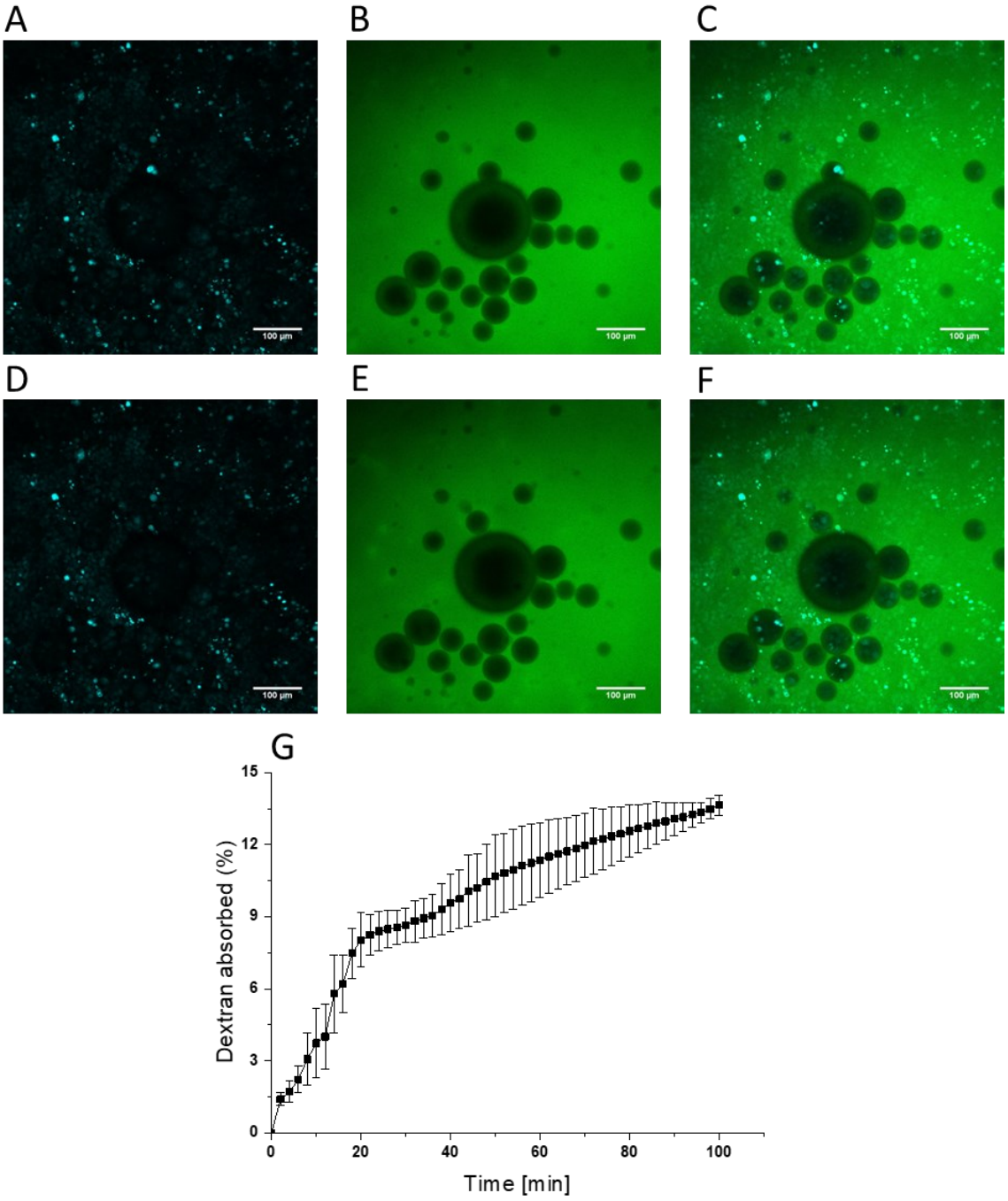


**Figure 4.4.** 3 kDa fluorescent dextran (green) permeability assay of Caco-2 cells cultured in the gut-on-chip in contact with the oil macroemulsion after 1 PBS wash. Nuclei were stained with Hoechst (blue). Nuclei at 0 min (A) and 100 min (D). Dextran intensity at 0 min (B) and at 100 min I. Merge of the two channels at 0 min (C) and 100 min (F). Dextran absorbed in the collection chamber computed as difference in dextran fluorescence over time (G) (n = 3 microfluidic devices).

After two washes with PBS, the absorption curve showed an initial burst absorption up to 40 min, after which the slope of curve decreased, indicating a lower absorption (**Fig. 4.5**). The final absorption of dextran was 12.6%. However, this value was not statistically different from the previous one, indicating that a similar oil concentration was still present.

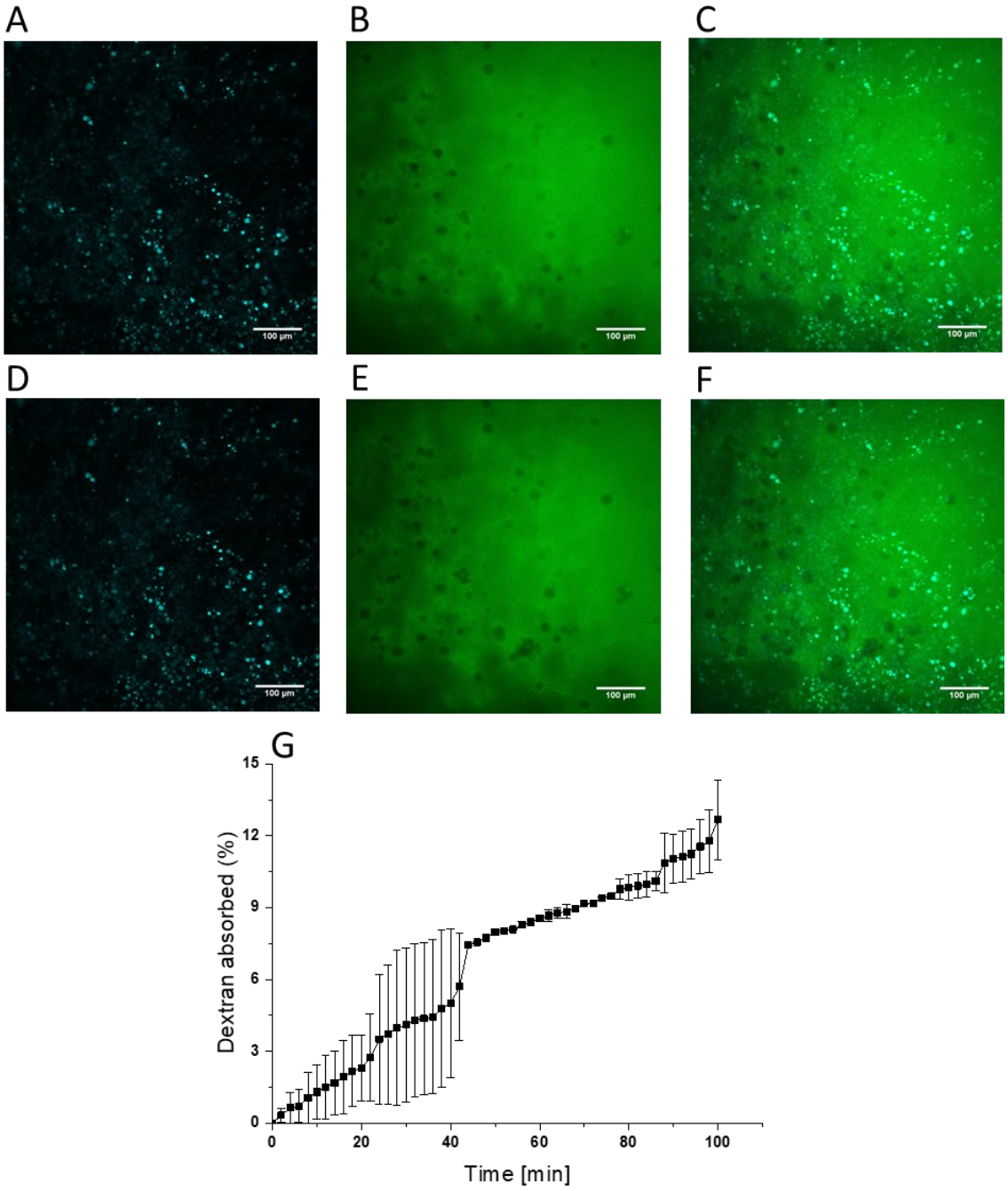


**Figure 4.5.** 3 kDa fluorescent dextran (green) permeability assay of Caco-2 cells cultured in the gut-on-chip in contact with the oil macroemulsion after 2 PBS washes. Nuclei were stained with Hoechst (blue). Nuclei at 0 min (A) and 100 min (D). Dextran intensity at 0 min (B) and at 100 min I. Merge of the two channels at 0 min (C) and 100 min (F). Dextran absorbed in the collection chamber computed as difference in dextran fluorescence over time (G) (n = 3 microfluidic devices).

The same devices were washed and subjected to dynamic conditions again for 2 days. Then, we repeated the dextran permeability assay (**Fig. 4.6**). The absorption curve showed an initial burst absorption up to about 40 min, after which the absorption was sustained until the end. This behavior resembled the control case discussed in the previous chapter. Unlike the control, the curve was less steep, aligning with the total concentration of dextran absorbed at 100 min, approximately 26.7%.

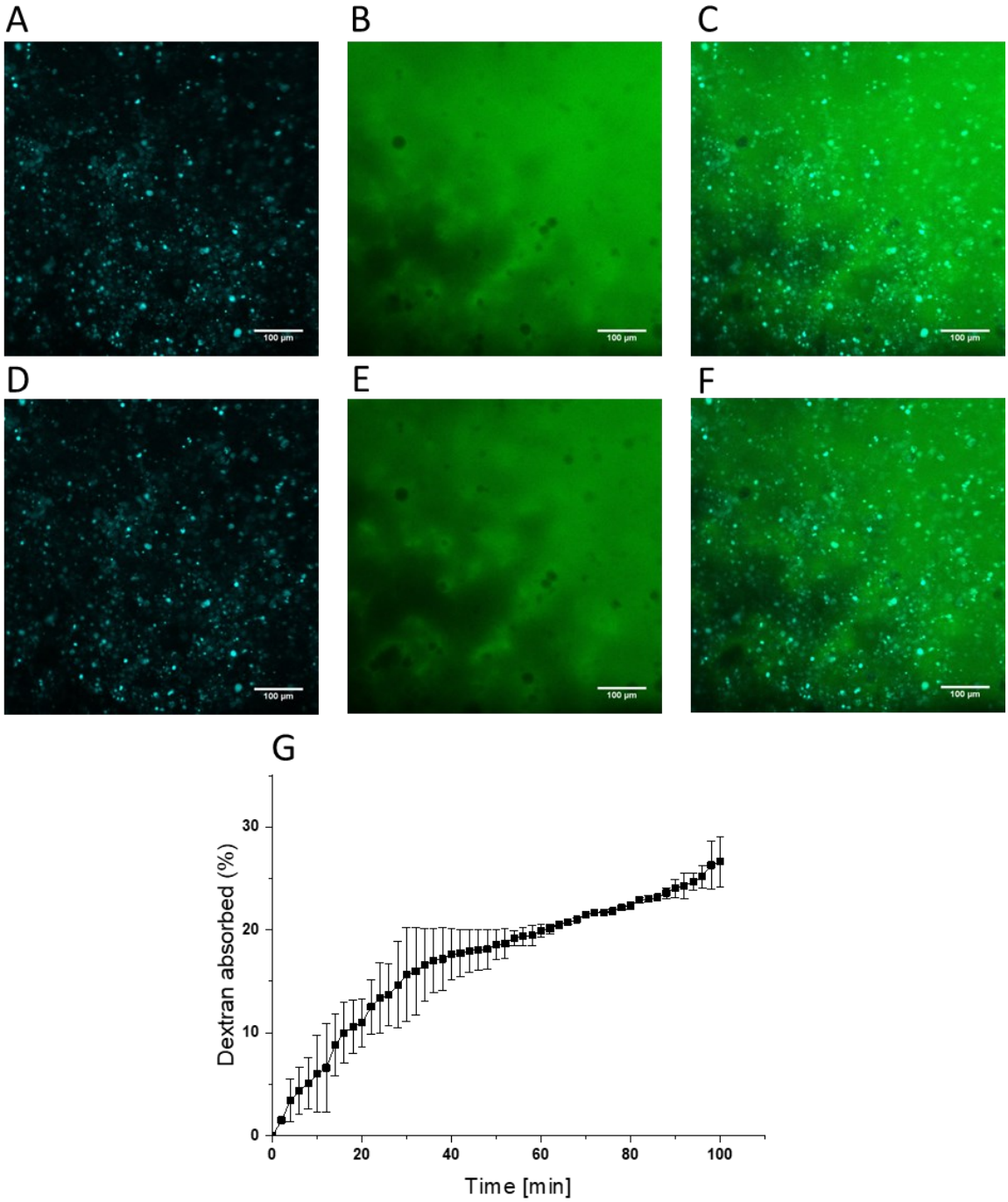


**Figure 4.6.** 3 kDa fluorescent dextran (green) permeability assay of Caco-2 cells cultured in the gut-on-chip in contact with the oil macroemulsion after 2 days of dynamic culture. Nuclei were stained with Hoechst (blue). Nuclei at 0 min (A) and 100 min (D). Dextran intensity at 0 min (B) and at 100 min I. Merge of the two channels at 0 min (C) and 100 min (F). Dextran absorbed in the collection chamber computed as difference in dextran fluorescence over time (G) (n = 3 microfluidic devices).

When considering the 100 min dextran absorption in each case (**Fig. 4.7**), a significant difference was observed between the control and the oil addition and after the washes ($p < 0.05$), whereas the difference between the control and the condition after two days of culture was not statistically significant. This demonstrated that, initially, oil was spread on the epithelium, diminishing dextran permeability. Trough washing, part of the oil

was removed, while a part of it remained attached to the epithelium, possibly due to hydrophobic interactions with the mucus layer. Then, after 2 days of dynamic culture, dextran permeability was nearly restored. This indicates that our idea is feasible and time-dependent, meaning that it is not a permanent solution and it will not adversely affect the normal conditions of intestinal epithelium over an extended period.

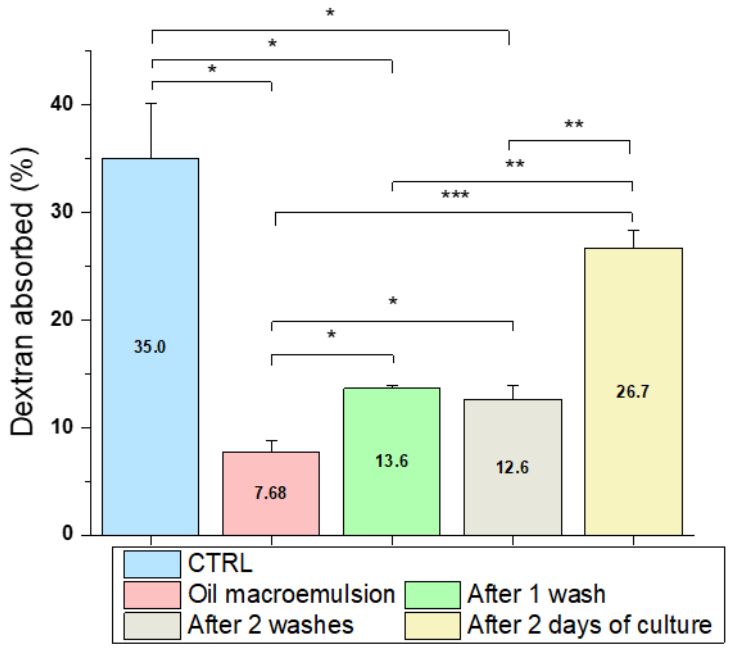


**Figure 4.7.** Difference in dextran absorption at 100 min after the contact with the oil macroemulsion. ( * $p < 0.05$; ** $p < 0.01$; *** $p < 0.001$; $n = 3$ microfluidic devices for each experiment).

After confirming the beneficial effect of oil addition in thickening the intestinal barrier, our next step was to assess the action of the starch emulsion. Before proceeding, we conducted a vitality assay using MTT powder to evaluate Caco-2 cell interaction with empty and cur-loaded starch emulsions at two different concentrations. After 24 hours from the contact, all conditions showed a high vitality, with no significant differences among conditions (**Fig. 4.8 A**). After 48 hours from the contact, the more concentrated conditions appeared to show lower vitality compared to their respective lower dosages (**Fig. 4.8 B**). However, these differences were not significant. Overall, the starch emulsion did not significantly affect cell viability.

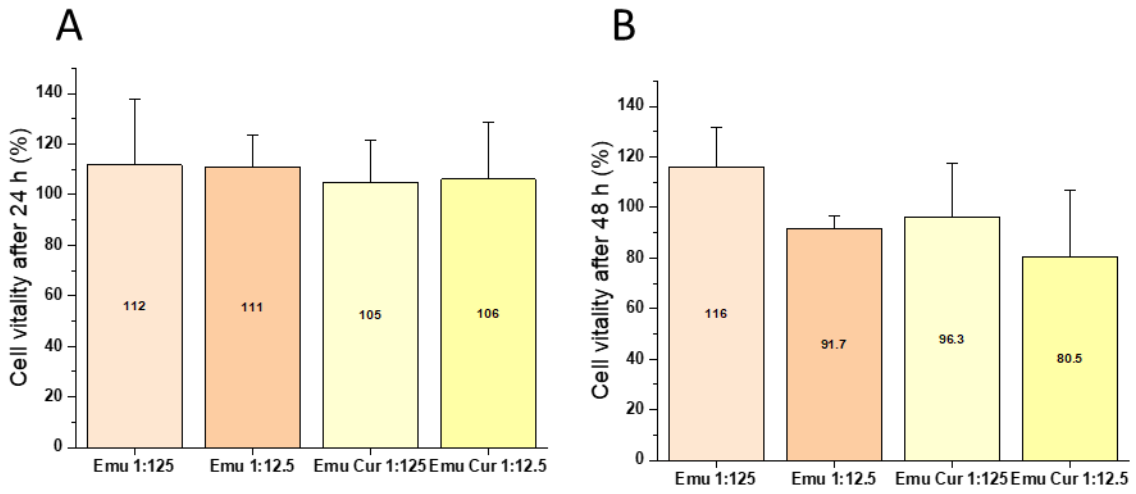


**Figure 4.8**. MTT vitality assay of Caco-2 cells in contact with the starch emulsion with and without cur at two different concentrations.

Once vitality was tested vitality, we proceeded to assess the effects of starch emulsion inside the gut-on-chip. Firstly, we tested them in the presence of *R. Bromii* to evaluate dextran permeability. We added the starch emulsion for 2 hours inside the microfluid device, then washed with PBS, added the dextran solution and started imaging (**Fig. 4.9**). In this case the absorption curve appeared to be almost linear, with a final absorption of approximately 7.84%, a value and a curve shape resembling that observed for O/W macroemulsion addition (**Fig. 4.3**).

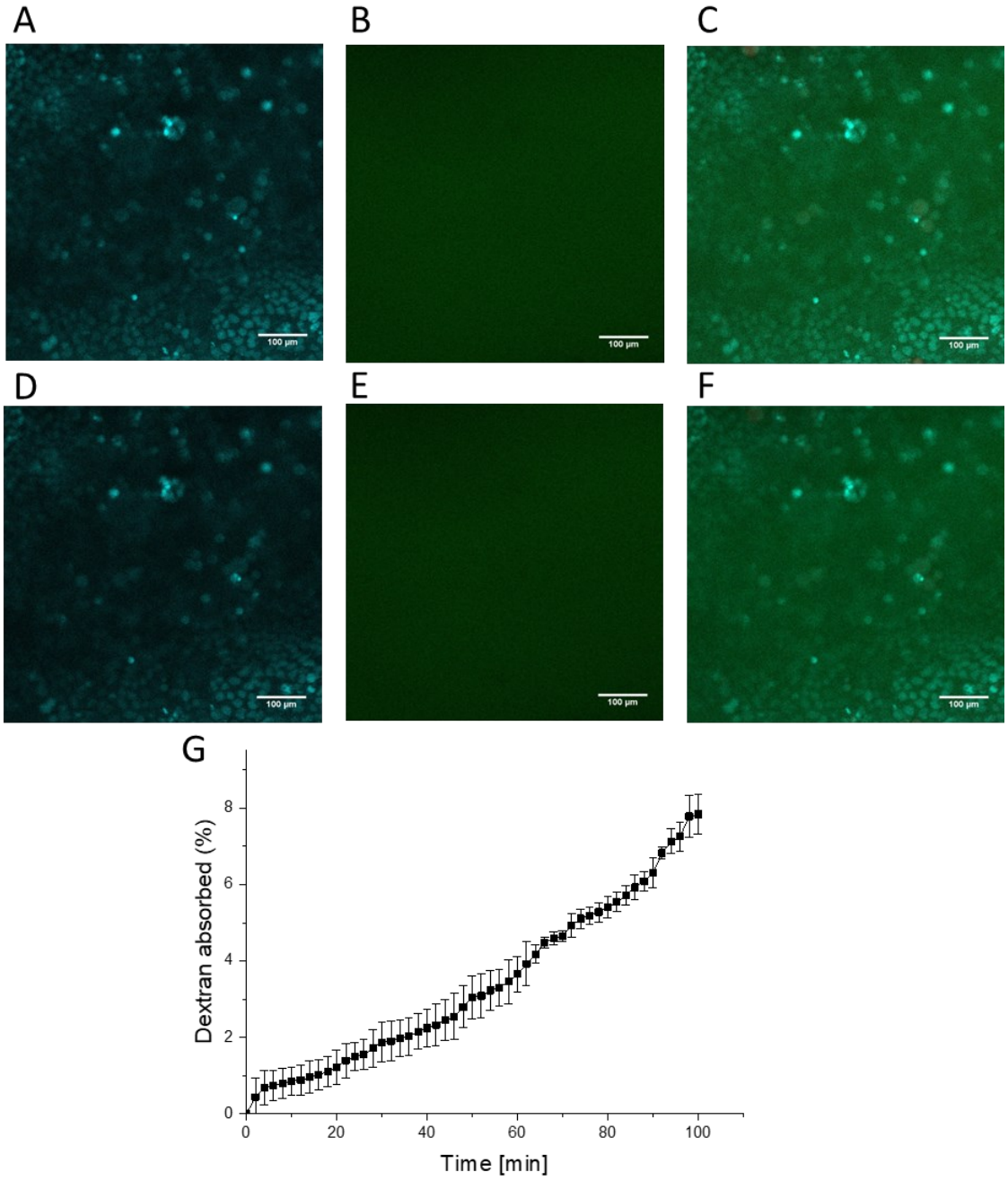


**Figure 4.9**. 3 kDa fluorescent dextran (green) permeability assay of Caco-2 cells cultured in the gut-on-chip in contact with the starch emulsion after 1 PBS wash. Nuclei were stained with Hoechst (blue). Nuclei at 0 min (A) and 100 min (D). Dextran intensity at 0 min (B) and at 100 min I. Merge of the two channels at 0 min (C) and 100 min (F). Dextran absorbed in the collection chamber computed as difference in dextran fluorescence over time (G) (n = 3 microfluidic devices).

After the second wash in PBS, the dextran absorption rate changed (**Fig. 4.10**). In details, in a first phase, up to 60 min, the absorption was slow. Then, the rate increased up to about 15.6% at 100 min.

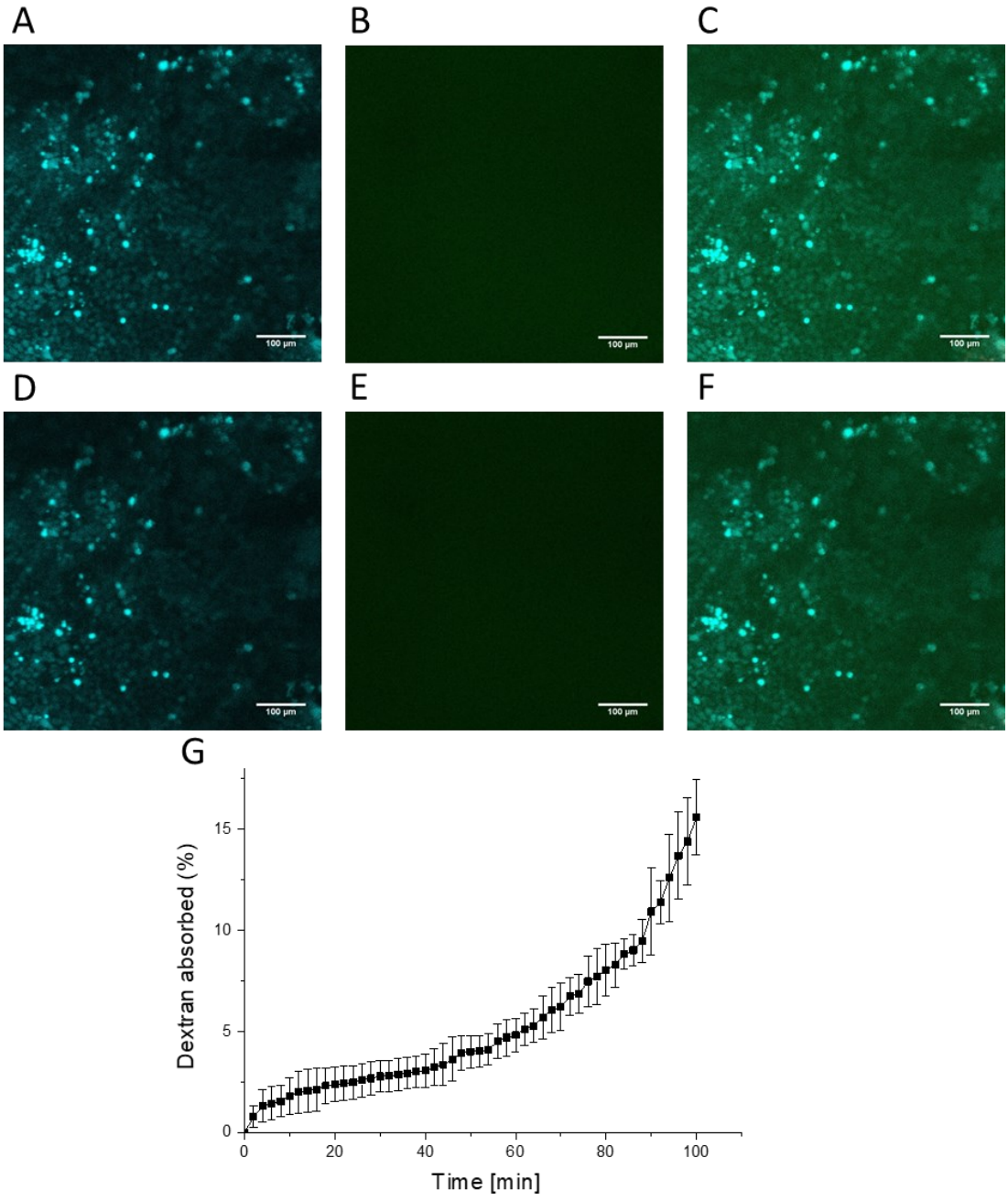


**Figure 4.10.** 3 kDa fluorescent dextran (green) permeability assay of Caco-2 cells cultured in the gut-on-chip in contact with the starch emulsion after 2 PBS washes. Nuclei were stained with Hoechst (blue). Nuclei at 0 min (A) and 100 min (D). Dextran intensity at 0 min (B) and at 100 min I. Merge of the two channels at 0 min (C) and 100 min (F). Dextran absorbed in the collection chamber computed as difference in dextran fluorescence over time (G) (n = 3 microfluidic devices).

Similarly to the case with the O/W macroemulsion, the use of starch emulsion revealed different permeability depending on the number of washes. In particular, we observed more than a halved absorption after adding the starch emulsion for 2 hours and subsequent PBS wash, with respect to the control ($p < 0.01$). Then, after

another PBS wash, the absorption was almost reestablished, transitioning from 7.84% to 15.6% at 100 minutes. However, the difference compared to the control was still significant ($p < 0.05$). This remarks the transient action of the oil on the epithelium membrane, as the normal situation is restored over time.

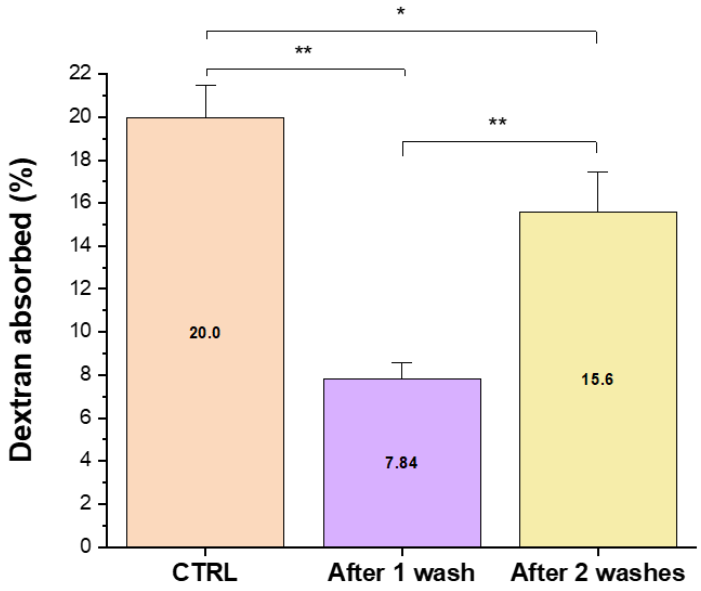


**Figure 4.11.** Difference in dextran absorption at 100 min after the contact with the starch emulsion. (* $p < 0.05$; ** $p < 0.01$; n = 3 microfluidic devices for each experiment).

As stated before, the oil core allowed for the loading of cur inside the starch emulsion. To test the carrier's anti-inflammatory action, we used a solution of LPS to induce inflammation in the gut-on-chip. We employed a ROS-detector kit to stain the ROS and computed their intensity in the gut-on-chip in different conditions (**Fig. 4.12**). In details, we tested the control, representing the gut-on-chip without the addition of LPS (**Fig. 4.12 A-B-C**); the addition of LPS for 4 hours (**Fig. 4.12 D-E-F**); the addition of LPS for 4 hours, followed by treatment with cur-loaded starch emulsion for 2 hours without *R. Bromii* (**Fig. 4.12 G-H-I**); the addition of LPS for 4 hours, followed by treatment with cur-loaded starch emulsion for 2 hours with *R. Bromii* in the device (**Fig. 4.12 J-K-L**). All results were significantly different from each other (**Fig. 4.12 M**) ($p < 0.0001$). Interestingly, the treatment with the cur-loaded starch emulsion differed depending on whether *R. Bromii* was present or not. In details, if *R. Bromii* was not present, the intensity of ROS was almost 1.5 times higher than in the case with *R. Bromii* co-culture. This indicates that the bacteria were effectively able to release cur from the oil core by degrading the starch shell, almost restoring a not-inflamed condition. On the other hand, the difference between the inflamed condition and the inflamed condition without bacteria but treated with cur-loaded starch emulsions, could be due to a small presence of free cur inside the water phase.

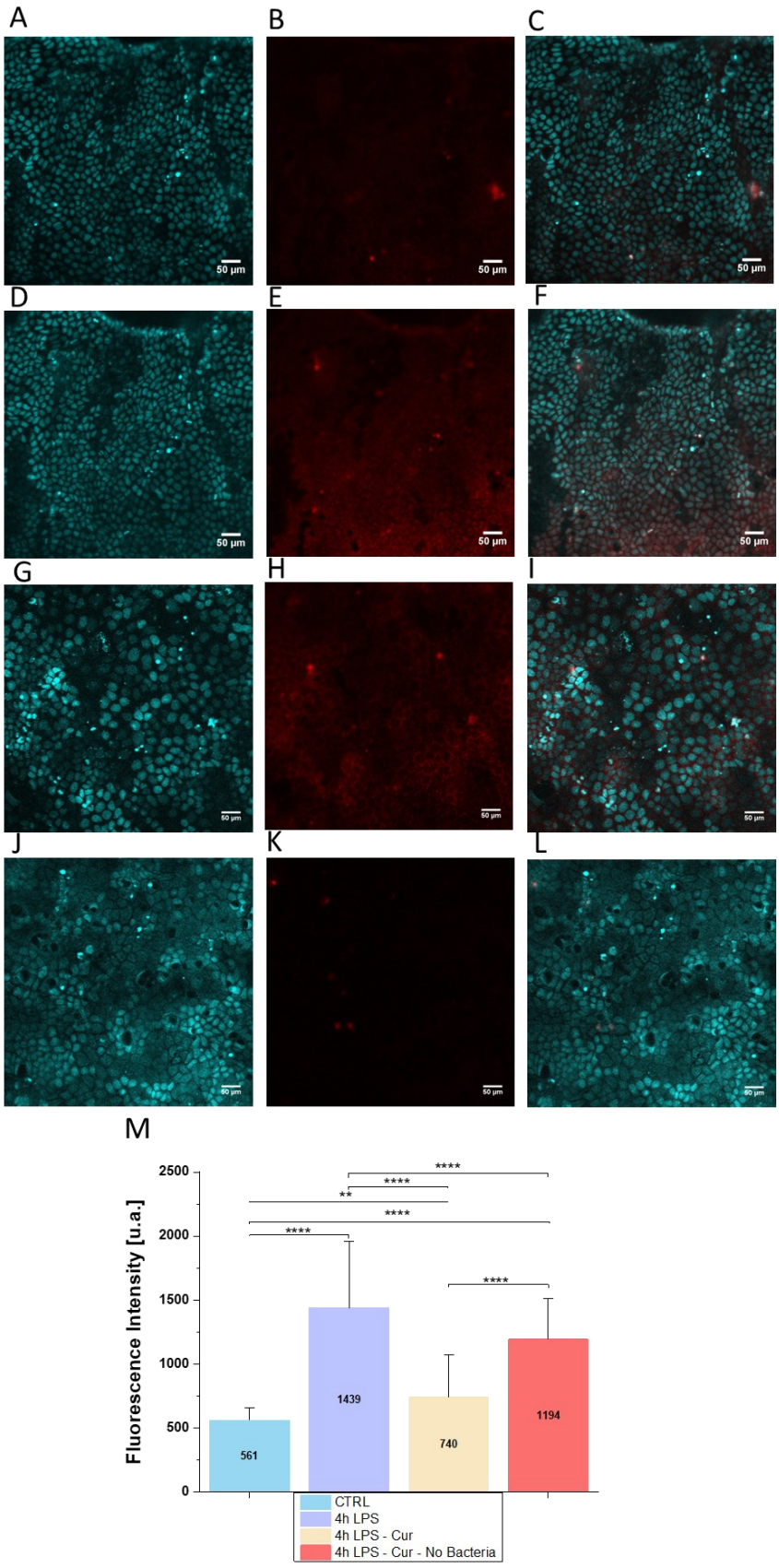


**Figure 4.12.** Confocal analysis of reactive oxidative species (red). Cell nuclei were stained with Hoechst (blue). Third column represents the merge of the two channels. The control was performed without LPS addition (A-B-C). ROS after the addition of LPS for 4h (D-E-F). ROS after the addition of LPS for 4h and 2h of contact with the cur-loaded starch emulsion (G-H-I). ROS after the

addition of LPS for 4h and 2h of contact with cur-loaded starch emulsion in presence of *Ruminococcus Bromii* (J-K-L). Fluorescence intensity of ROS for each condition (M) (** $p < 0.01$; **** $p < 0.0001$; n = 3 microfluidic devices, different regions analyzed for each device).

To further prove the action of cur-loaded starch emulsion, we stained tight junctions through immunofluorescence in two conditions: the treatment in presence of R. Bromii after inflammation (**Fig. 4.13 A-B-C-D**) and inflammation only (**Fig. 4.13 E-F-G-H**). Claudin-1, the main protein present in tight junctions, is almost absent in the case of the inflamed epithelium, demonstrating a reduction in barrier properties, with permeability being the main factor involved. This situation is consistent with corroborations from *in-vivo* studies[8,9]. On the other hand, the treatment with the emulsion appeared to have restored the typical web-like structure of tight junctions and cell-cell interaction, showing a significant difference from the inflamed case (**Fig. 4.13 I**) ($p < 0.0001$). This provides further evidence that our carrier, through cur release, could restore the initial situation of a non-inflamed epithelium.

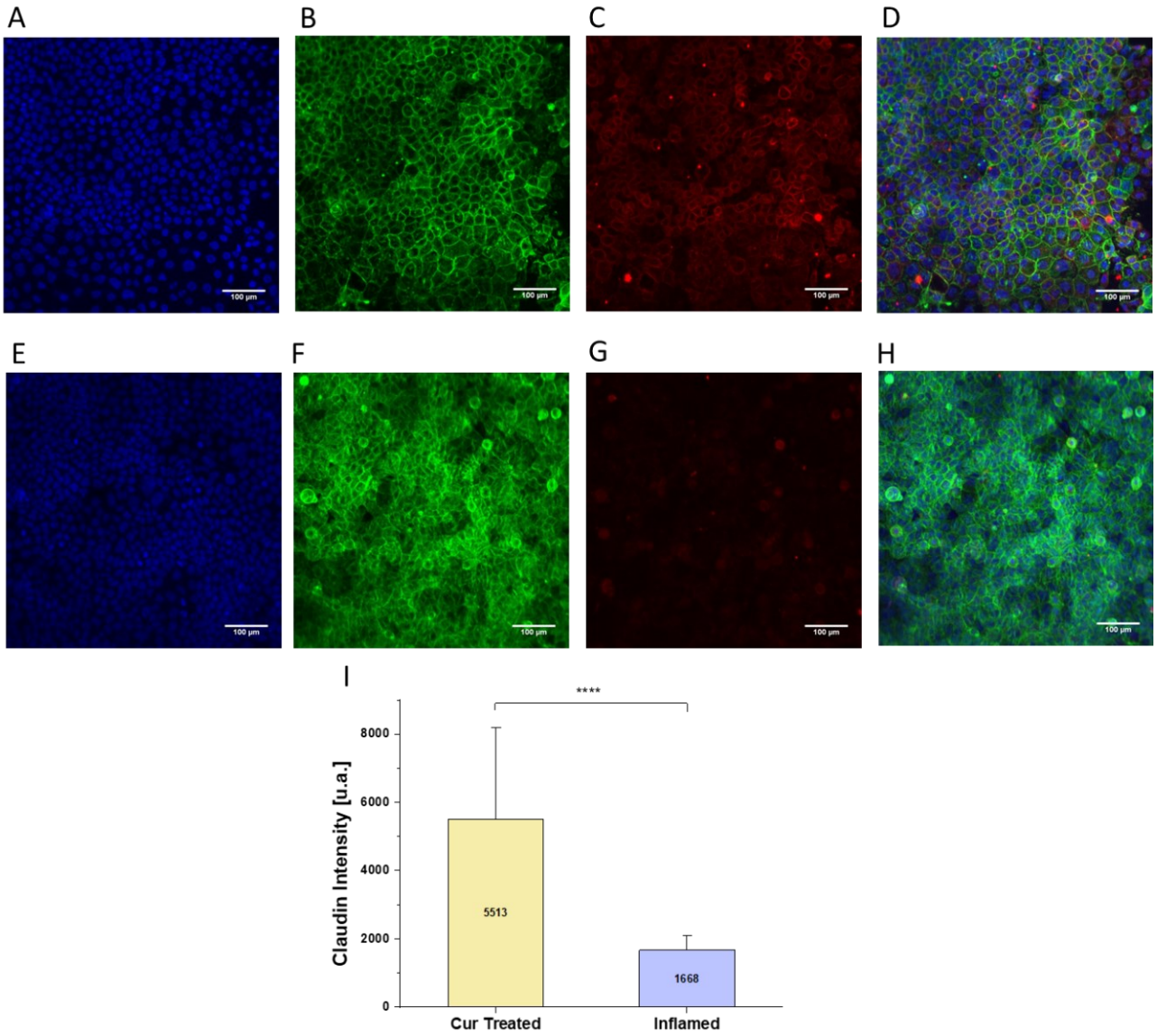


**Figure 4.13.** Tight junction analysis at the confocal microscope. Cell nuclei were stained with Hoechst (blue). Actin was stained with phalloidin (green). Tight junction were stained with claudin-1 antibody (red). The fourth column represent the merge of the three channels. Staining of inflamed epithelium in contact with cur-loaded starch emulsion for 2h in presence of *Ruminococcus Bromii* (A-B-C-D). Staining of inflamed epithelium without any treatment (E-F-G-H). Fluorescence intensity of claudin-1 for each condition (I). (**** $p < 0.0001$; n = 3 microfluidic devices, different regions analyzed for each device).

Finally, to once again confirm the efficacy of the proposed carrier, we imaged the two samples described above using SEM. As observed in **Fig. 4.14**, the villi structure is almost preserved for the treated sample, with a good distribution and density of villi (**Fig. 4.14 A-B**), while their presence is hindered and their density is much lower in the case of the inflamed samples (**Fig. 4.14 C-D**).

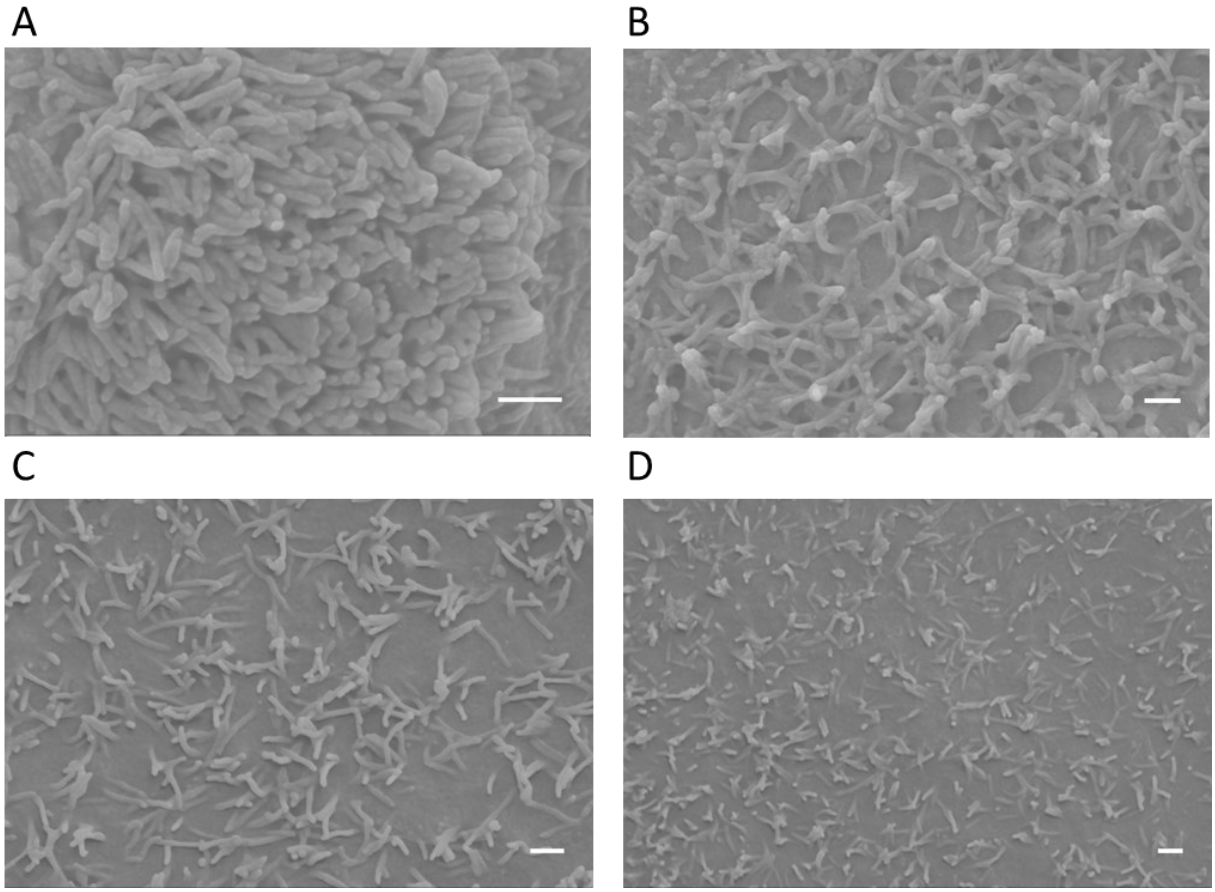


**Figure 4.14.** SEM images of Caco-2 cells cultured in the gut-on-chip when inflamed and treated with the cur-loaded starch emulsion for 2h in presence of *Ruminococcus Bromii* (A-B) and without any treatment (C-D). Scale bar is 500 nm.

## 4.4. Discussion

In this chapter, we demonstrated an application of the gut-on-chip as a drug screening platform with a diseased gut. Firstly, we used it to prove the concept of implementing oil as an absorption reducer, interacting with the intestinal barrier and with mucus through hydrophobic interactions. This strategy not only proved valid, but also temporary, meaning that the oil does not interfere with the physiological conditions of the intestine. In fact, after 2 days of dynamic culture, dextran absorption was not significantly different from the control, representing the device prior to macroemulsion addition. The oil could potentially act as a satiety inducer, particularly with unsaturated fatty acids present in soybean oil, which was used to produce the emulsion[10]. Furthermore, soy has been shown to have a beneficial effect in treating obesity by reducing fat mass and improving insulin resistance, a hallmark of obesity[11].

Subsequently, we proved the ability of the starch emulsion to reduce nutrient absorption by taking advantage of *R. Bromii* ability to degrade starch. After co-culturing the bacteria in the gut-on-chip, we introduced the starch emulsion for 2 hours, allowing bacteria to degrade the starch and release the oil onto the epithelium barrier. Here, the oil acted as an additional resistance layer to absorption. Similarly to the previous case, after washing with PBS, absorption increased, getting closer to the control case. This further proved the temporary

and reversible action of the oil on the epithelium membrane. The difference between the various cases could be ascribed to part of the oil that remained unwashed, interacting with the mucus layer and forming strong hydrophobic links.

The proposed microfluidic device can also serve as a pathological platform. As a matter of fact, thanks to the addition of LPS, it is possible to inflame the intestinal epithelium, prompting the release of molecules typical of an inflamed intestine, such as ROS. ROS levels in the inflamed case were consistently higher with respect to the control case. We focused on ROS detection to see whether the cur-loaded starch emulsion could release cur and, in turn, diminish ROS levels and the associated inflammation status. To observe its action, we imaged ROS in the presence or absence of *R. Bromii*. Interestingly, the presence of *R. Bromii* was associated with a consistent reduction in ROS levels, returning almost to the control value. In absence of bacteria, ROS levels were slightly but significantly lower than in the inflamed status, possibly due to a small portion of cur present in the aqueous phase. This indicates that the cur release is strictly associated with the starch degradation ability of *R. Bromii*, which, we recall, are over-represented in the gut flora of obese subjects. Our strategy was further confirmed by immunofluorescence analysis of tight junctions. As well-known, permeability is enhanced in an inflamed epithelium, linked to decreased tight junction formation and claudin expression. This is true for different diseases, such as IBD, both in humans[8] and in mouse models[12], malignant obstructive jaundice[13], type-2 diabetes[14] and, especially, in obesity[5]. In fact, in the inflamed case, claudin-1 was almost absent, whereas, after cur-loaded starch emulsion treatment, its expression was consistently higher. SEM analysis of the villi supported these findings, showing denser and more widely distributed villi for the cur-treated samples with respect to the non-treated ones.

Overall, these results together suggest the potential effects of our strategy in human colon. Specifically, our strategy is based on a triple action: i) acting at microflora level by entrapping the keystone species in degrading starch, *R. Bromii*¸ over-represented in the gut microflora of obese subjects; ii) recreating an oil film on the intestinal barrier, hindering higher nutrient absorption associated with higher levels of SCFAs in obesity; iii) releasing cur at the intestinal level, reducing the chronic inflammation typical of obese subjects. These properties are accompanied by resistance in GIT thanks to the starch shell and efficacy strictly connected to the presence of the starch-degrading bacterial species. Moreover, the presence of soybean oil could result in improved insulin resistance and a feeling of satiety.

## 4.5. Conclusion

In this chapter, we demonstrated the anti-inflammatory and absorption reduction capabilities of the proposed carrier, tested in a previously characterized gut-on-chip microfluidic platform. This not only demonstrated the potential implementation of such a strategy as a treatment for obesity but also highlighted the ability of the proposed gut-on-chip to serve as a drug screening platform, capable of representing both healthy and inflamed intestinal epithelium, with the flexibility of introducing anaerobic and aerobic gut microflora. However, it is

important to note that while we dissected obesity at the cellular and tissue level (focusing on inflammation, dysbiosis and increased nutrients intake), *in-vivo* studies are imperative to comprehensively understand the macroscopic implications of such strategy on body weight, gut microflora composition and metabolomics.

## 4.6. Bibliography


1. Meldrum, D. R., Morris, M. A. & Gambone, J. C. Obesity pandemic: causes, consequences, and solutions—but do we have the will? *Fertil. Steril.* **107**, 833–839 (2017).

2. Duranti, S., Ferrario, C., van Sinderen, D., Ventura, M. & Turroni, F. Obesity and microbiota: an example of an intricate relationship. *Genes Nutr.* **12**, 18 (2017).

3. Tarasiuk, A., Mosińska, P. & Fichna, J. The mechanisms linking obesity to colon cancer: An overview. *Obes. Res. Clin. Pract.* **12**, 251–259 (2018).

4. Spagnuolo, M. I. *et al.* Relationship between severe obesity and gut inflammation in children: what's next? *Ital. J. Pediatr.* **36**, 66 (2010).

5. Ahmad, R., Rah, B., Bastola, D., Dhawan, P. & Singh, A. B. Obesity-induces Organ and Tissue Specific Tight Junction Restructuring and Barrier Deregulation by Claudin Switching. *Sci. Rep.* **7**, 5125 (2017).

6. Dailey, M. J. Nutrient-induced intestinal adaption and its effect in obesity. *Physiol. Behav.* **136**, 74–78 (2014).

7. Cawthon, C. R. & De La Serre, C. B. The critical role of CCK in the regulation of food intake and diet-induced obesity. *Peptides* **138**, 170492 (2021).

8. Bertiaux-Vandaële, N. *et al.* The Expression and the Cellular Distribution of the Tight Junction Proteins Are Altered in Irritable Bowel Syndrome Patients With Differences According to the Disease Subtype. *Am. J. Gastroenterol.* **106**, 2165–2173 (2011).

9. Ivanov, A. I., Nusrat, A. & Parkos, C. A. The Epithelium in Inflammatory Bowel Disease: Potential Role of Endocytosis of Junctional Proteins in Barrier Disruption. in *Novartis Foundation Symposia* (eds. Chadwick, D. & Goode, J.) vol. 263 115–132 (Wiley, 2004).

10. Jurgoński, A., Juśkiewicz, J. & Zduńczyk, Z. A High-Fat Diet Differentially Affects the Gut Metabolism and Blood Lipids of Rats Depending on the Type of Dietary Fat and Carbohydrate. *Nutrients* **6**, 616–626 (2014).

11. Velasquez, M. T. & Bhathena, S. J. Role of Dietary Soy Protein in Obesity. *Int. J. Med. Sci.* 72–82 (2007) doi:10.7150/ijms.4.72.

12. Mennigen, R. *et al.* Probiotic mixture VSL#3 protects the epithelial barrier by maintaining tight junction protein expression and preventing apoptosis in a murine model of colitis. *Am. J. Physiol.-Gastrointest. Liver Physiol.* **296**, G1140–G1149 (2009).

13. Wang, N. *et al.* Evidence for tight junction protein disruption in intestinal mucosa of malignant obstructive jaundice patients. *Scand. J. Gastroenterol.* **45**, 191–199 (2010).

14. Nascimento, J. C., Matheus, V. A., Oliveira, R. B., Tada, S. F. S. & Collares-Buzato, C. B. High-Fat Diet Induces Disruption of the Tight Junction-Mediated Paracellular Barrier in the Proximal Small Intestine Before the Onset of Type 2 Diabetes and Endotoxemia. *Dig. Dis. Sci.* **66**, 3359–3374 (2021).

# 5. Final conclusions and future perspectives

Throughout this thesis, we aimed to address obesity by acting on the main differences between healthy and obese subjects, specifically: chronic inflammation, dysbiosis and enhanced intestinal permeability. Our approach involved a novel strategy taking advantage of the ability of the *R. Bromii*, a key species implicated in obesity and SCFAs production, to degrade starch. The strategy employed a starch shell and an oil core loaded with cur, a potent natural anti-inflammatory agent. The starch shell served to protect the drug from the harsh conditions of the GIT and deliver it at the site of interest, the colon, as only in the colon there are starch degrading species, especially *R. Bromii*, considered the keystone one. Here, the bacteria are able to open the particle, liberating the oil core. Part of the bacteria remain blocked in the oil, leading to a quenching of their metabolism. This is crucial as such bacteria are involved in energy homeostasis, which is strongly unbalanced in obese subjects. By quenching their activity, we aimed to restore gut microflora balance and simultaneously reduce calories production. Another part of the oil, freed from the starch shell, goes on the intestinal epithelium, acting as an additional resistance layer to the passage of molecules, temporarily thickening the barrier, often compromised in obesity. Furthermore, the proximity of the oil to the barrier facilitated localized release of curcumin from the oil core, contributing to the reduction of inflammatory status at the cellular level.

The proposed strategy was tested in a suitable gut-on-chip model that effectively expressed key functionalities of the intestine, including mucus and villi production, and co-culture of anaerobic and aerobic bacteria in the same channel of cells. Furthermore, it provided the flexibility to study drug screening not only in healthy conditions but also in an inflamed epithelium, making it suitable for disease-related tests.

While the proposed strategy and the presented gut-on-chip platform appear promising, further *in-vivo* studies are essential to investigate factors such body weight and metabolomics that are impossible to study *in-vitro*. Moreover, the *in-vivo* tests can also provide additional validation of the gut-on-chip as a reliable platform for studying drugs in both healthy and diseased conditions, aligning with the requirements for FDA approval.

Overall, this thesis aimed to bridge diverse fields of knowledge, spanning from microbiology to chemistry, and adopting an engineering approach to address and solve complex challenges.

# 6. Side Works

## 6.1. Polymeric soft micro-robots propelled into a microfluidic device for gut target delivery studies

### 6.1.1. Introduction

In recent years, microrobots have emerged as a promising tool for targeted drug delivery and minimally invasive medical procedures[1,2]. Typically ranging from a few micrometers to several millimeters in size, these microrobots can be engineered to respond to various stimuli, including magnetic fields, light, or chemical gradients[3,4].

Among the various types of microrobots, soft microrobots have garnered increasing attention due to their biocompatibility and their ability to navigate through complex and confined biological environments[5,6]. This adaptability allows soft microrobots to transport drugs to specific sites within the body, mitigating the side effects associated with systemic drug delivery.

For instance, Mair et al. designed magnetically activated alginate soft microrobots capable of delivering drugs to the central nervous system by tumbling and "walking" on the spinal cord[7]. Similarly, Lee et al. developed a spring-like soft microrobot for the precise release of doxorubicin, an anticancer drug, through swelling and deswelling in response to a near-infrared stimulus[8].

In the realm of disease diagnosis, soft microrobots can be employed to detect and target cancer cells, as demonstrated by Power et al. They engineered microrobots responsive to the lower pH typical of cancer cells, combining pH responsiveness with light responsiveness to modulate drug release[9].

Moreover, soft microrobots can harness chemical gradients for movement, utilizing bubble-based propulsion[10,11]. While this approach eliminates the need for external actuation, it is often associated with the use of metals and has a limited propulsion lifetime.

Our study focused on testing soft, biodegradable microrobots designed to target the gut epithelium simulated within our microfluidic device. However, it's noteworthy that microfluidic models can replicate the physiological behavior of various organs and tissues beyond the colon. Microfluidic models have been created to study the physiological environment of diverse organs, including the liver[12], heart[13], lungs[14], kidneys[15], and brain[16], among others.

For colon treatment, soft micro-robots could be encapsulated in a easily ingestible capsule that degrades in the intestine. This approach eliminates the need for intra-tissue injections, which are often painful and require specialized healthcare personnel, especially for other tissues or organs.

The versatility of microfluidics renders it a promising tool for studying a broad range of biological systems and developing innovative therapies for various diseases[17].

In our study, we developed soft microrobots using alginate MPs containing fluorescent nanoparticles and sodium bicarbonate. This composition facilitates detection and movement control, respectively.

Our biodegradable soft microrobots offer several advantages. Unlike other approaches, we require no external fields, whether magnetic[18,19] or acoustic[20]. Once ingested, our microrobots can function solely with the water naturally present in the intestine, although with less control over velocity.

Furthermore, our system is cost-effective, easily scalable, and high-throughput compared to other techniques such as 3D laser lithography[18,19] or bioprinting[21], without relying on other biological entities like bacteria[22,23] or microalgae[24].

While our biodegradable microrobots necessitate pre-loading with sodium bicarbonate before effective use, this is akin to other systems where magnetic nanoparticles must be included for magnetic properties[23,25].

For precise carrier control and detection, we embedded fluorescent nanoparticles, enabling real-time tracking in a microfluidic device. Sodium bicarbonate inside the microrobots acts as a self-propulsion mechanism by reacting with the acidic environment, facilitated by citric acid co-delivered in a commercial capsule to the small intestine.

Our approach avoids the use of metals, employing natural, biocompatible, and biodegradable alginate[26], ensuring prolonged propulsion lifetime. We investigated microparticle action using a concentration gradient microfluidic device[27], demonstrating their propulsion by changing the citric acid gradient direction.

In the main chamber, we cultured Caco-2 cells, a model for simulating the intestinal barrier, showcasing promising interactions between microparticles and the intestinal barrier, irrespective of the flow rate.

These microparticles can be loaded with drugs or gut bacteria, as demonstrated by our research group[28], offering the potential for localized delivery near the intestinal epithelium. Our results provide valuable insights into the behavior of soft microrobots in a physiologically relevant environment, holding implications for future biomedical applications in colon treatment.

## 6.1.2. Materials and Methods

### 6.1.2.1. Biodegradable microrobots preparation

Soft polymeric microrobots were obtained following a previously described method[28]. In details, a single water-in-oil emulsion was performed by using f $CaCO_3$ as a cross-linking agent. The water phase was composed of 10 ml of 2% (w/v) alginate comprising 0.5 ml of $CaCO_3$ 0.05 M. This was firstly homogenized

by Ultra-Turrax (IKA T25 Digital, India) for 2 min at 3000 rpm. Then, 33 µl of a solution of fluorescent nanoparticles (1%, latex beads, amine-modified polystyrene, fluorescent orange, Sigma-Aldrich, USA) were added to the alginate water phase. This latest was added dropwise to 50 ml of an oil phase (soybean oil, Sigma-Aldrich, USA) comprising 500 µl of Span®80. The whole solution was kept under stirring at 200 rpm for 15 min (Heidolph RZR 2102-BR 10, Germany). After that, a solution composed of 40 µl of glacial acetic acid (Sigma-Aldrich, USA) and 10 ml of soybean oil was added as to obtain a dissociation of $CaCO_3$ due to pH variation that would allow a first $Ca^{2+}$ mediated cross-linking. The second cross-linking was performed by adding a solution of $CaCl_2$ (0.2 M) and kept under stirring at 200 rpm for 30 min. Finally, to collect MPs to the emulsion was added a solution of 20% (v/v) TWEEN® 20, to promote the phase separation. The so collected particles were washed three times with TWEEN® 20 by centrifugation at 2500 rpm for 5 min at 4°C (SL16R Centrifuge; Thermo Scientific, United States) as to remove the excess of oil and as to avoid particle aggregation. The particles were then filtered and lyophilized (−50°C, 0.73 hPa, Heto PowerDry PL6000 Freeze Dryer; Thermo Electron Corp., United States).

When particles were fully lyophilized, sodium bicarbonate was post-encapsulated in the MPs by putting in contact a solution of 5 mg/ml of particles in water with a solution of sodium bicarbonate (0.1 M) overnight on a magnetic stirrer (500 rpm). After this passage, three washes in MilliQ water were performed as to avoid a retaining of sodium bicarbonate in the water solution and particles were lyophilized again.

#### 6.1.2.2. Dimensional and Morphological Characterization of microrobots

The optical characterization of alginate microrobots involved both morphological and dimensional analyses. Morphological assessments were conducted using an Inverted Microscope (OLYMPUS IX73, 10× air objective, Japan). Additionally, the precise size of the microrobots was determined using static light scattering with a Mastersizer 2000 (Malvern Instruments, Malvern, UK). This involved analyzing a 0.4 mg/ml alginate-MP suspension in TWEEN® 20. The characterization included determining the average diameter (d50) as well as calculating the SPAN value, a measure of distribution width given by the formula:

$$\text{SPAN} = \left(\frac{\text{d90} - \text{d10}}{d50}\right)$$

Here, d90 represents the particle diameter at which 90% of the particles are smaller, d10 is the diameter at which 10% of the particles are smaller, and d50 is the average diameter.

#### 6.1.2.3. Cell culture

Human Caco-2 intestinal epithelial cells were obtained from American Type Culture Collection ((ATCC), HTB-37, Germany). The Caco-2 cells were cultured routinely in Dulbecco's Modified Eagle Medium (DMEM; Sigma, Denmark) supplemented with 10% (v/v) fetal bovine serum (FBS; Sigma, Denmark), 1% (v/v) L-

glutamine (Microgem, Italy) and 1% (v/v) penicillin-streptomycin (P/S; Gibco, Denmark). The cells were used at passages between 5 and 20.

#### 6.1.2.4. Microfluidic device fabrication

The microfluidic device was designed by AutoCAD. A PMMA layer was carved using micro-milling machine to obtain the mold. Then, a replica molding was performed by using PDMS (10:1 w/w with the curing agent). The device consisted of two inlets that led to an array of serpentine-shaped microchannels (300 µm width x 300 µm height), ending with five channels collapsing to one culture chamber (3.5 mm width x 15 mm length x 300 µm height). An additional inlet was added separately to the serpentine microchannels to deliver the MPs directly inside the culture chamber.

The replica molding consisted of pouring PDMS on the PMMA mold, degassing under vacuum in order to eliminate air bubbles and an incubation at 80°C for 60 min in an oven. After this time, the PDMS was fully cured and was detached from the mold. A scalpel was used to fine the edges, whereas the inlets and outlets were punched using a biopsy punch of 1.5 mm.

A slab of 0.5 mm of PMMA was used to close the channels by irreversible bonding.

In details, a solution of 60% ethanol, 20% tetraethyl-orthosilicate (TEOS, Sigma, Denmark), 10% HCl (0.1 M) and 10% chloroform (Sigma, Denmark) was prepared and let rest overnight. The PMMA was wet with 1 ml of this solution and then spun at 2000 rpm for 60 s using a spin coater.

The whole microfluidic system was assembled by irreversible bonding between PDMS and PMMA slab (0.5 mm, Laurell, WS-650MZ-23NPPB, USA). Then, an oxygen plasma treatment was performed on both PMMA and PDMS (1 min, 50% of power, 50% of oxygen) and bonded together by putting them in the oven for 2h at 80°C.

A solution of ethanol at 70% was used to sterilize the microfluidic device, tubes and connectors by flowing it in the device and let rest for 1 h. Then, a solution at 2% of P/S in PBS was used to do several washes, it was then washed away and the whole device was put under UV lights for 1 h. After the sterilization passage, a rat tail collagen solution (30 µg/ml) was flown in order to promote cell adhesion to the PMMA and incubated for 1 h at 37°C. Caco-2 cells were flown inside the device in a concentration equal to 700000 cells/ml and incubated in a humidified incubator at 37°C and 5% of $CO_2$ overnight to let them adhere. Then, the day after the culture, the cells were put in dynamic conditions by using a syringe pump (Harvard Apparatus, United States) with a flow rate equal to 5 µl/min.

For the experimental part, syringe pumps were used with a flow rate equal to 12.5 µl/min in order to recreate a linear gradient of citric acid inside the gradient chamber and to deliver the MPs inside it. Food dye was used in the preliminary experiment to evaluate the gradient formation according with the experimental parameters.

#### 6.1.2.5. Computational Fluid Dynamic (CFD) simulation

o assess the generation of gradients within the gradient chamber, a Computational Fluid Dynamics (CFD) simulation study was conducted using COMSOL Multiphysics® (version 5.0, COMSOL AB, Stockholm, Sweden). Laminar flow and Transport of Diluted Species physics were employed to model fluid flow and concentration profiles in the microfluidic device, respectively. Water was assumed as the fluid in this simulation.

The fluid flow in the microfluidic device was described by the Navier-Stokes equation.

The imposed flow rates at the inlets were set at 12.5 µl/min.

#### 6.1.2.6. Analysis of self-propelled microrobots in the gradient microfluidic device

To evaluate the propulsive characteristics of alginate microrobots, initial experiments were conducted within the microfluidic device in the absence of cells. In this setup, the microfluidic gradient chip was connected to syringe pumps to introduce polymeric microrobots diluted in PBS (first inlet). The second and third inlets of the chip received infusions of a 7 mol/l citric acid solution and PBS, respectively. Within a few minutes, a linear citric acid gradient was established.

Upon contact between the polymeric microrobots and the citric acid solution, the release of $CO_2$ induced the microrobots to move towards the opposite wall of the chamber. A sequence of fluorescent images was captured using a confocal microscope (Leica TCS SP5 coupled with a 25X/1.25 NA objective), to analyze these movements.

#### 6.1.2.7. Viability assay

To evaluate the microrobots' accumulation within the simulated mucus layer of gut tissue in the microfluidic device, and to assess the viability of the cells seeded within the same device, a Live-Dead assay was conducted. We employed a live/dead® Cell Imaging Kit (Life Technologies Corporation, UK) which included Calcein AM for staining live cells (excitation/emission 488 nm/515 nm) and Ethidium Bromide for staining dead cells (excitation/emission 570 nm/602 nm). After 5 days of cultivating Caco-2 cells within the chip's culture chamber, a mixture of 2 µM Calcein AM and 4 µM Ethidium Bromide was injected, and the cells were stained with the Live-Dead assay at 37°C for 30 minutes. Fluorescent images of the cells were captured using an inverted confocal microscope (Leica TCS SP5 coupled with a 25X/1.25 NA objective, Germany).

### 6.1.3. Results and discussion

#### 6.1.3.1. Polymeric soft microrobots production and characterization

Polymeric soft microrobots were generated using the single emulsion method, as detailed in the Materials and Methods section. The size of microparticles (MPs) was assessed using the Mastersizer, revealing a size distribution of 98.15 µm with a corresponding Span value of 1.69 (**Fig. 6.1.1 A**). Additionally, the incorporation of fluorescent nanoparticles facilitated visualization using a confocal microscope (**Fig. 6.1.1 B**).

The size distribution analysis of MPs demonstrated the efficacy of the single emulsion method in achieving a narrow and uniform particle size distribution. Moreover, the Span value, being less than 2.0, indicates that the d90 and d10 values are closely situated, confirming the narrow distribution of particles.

As illustrated in **Fig. 6.1.1 B**, the encapsulation of fluorescent nanoparticles enables the visualization and detection of alginate particles that would otherwise be transparent.

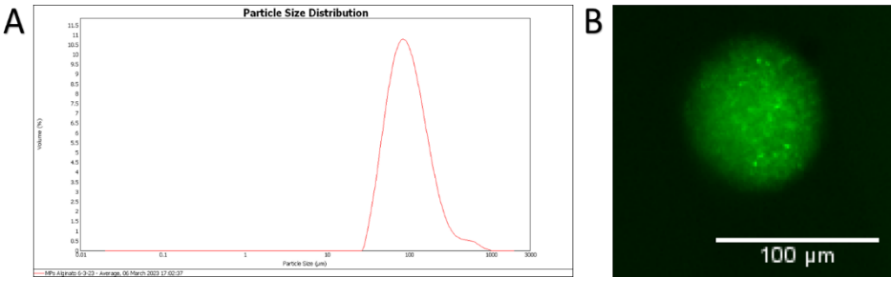


**Figure 6.1.1.** Size distribution of the alginate microparticles (A). Alginate microparticles with encapsulated fluorescent nanoparticles (green) (B).

#### 6.1.3.2. Chip propulsion studies of soft microrobots

We designed and developed a microchip based on PDMS-PMMA, featuring a gradient mixing module and a culture chamber for seeding Caco-2 cells. PDMS and PMMA were selected for their biocompatibility, high optical transparency, and low autofluorescence, making them ideal for research and rapid prototyping[29,30]. The detailed geometry and design of the chip, including a branched network of microchannels upstream of the culture gradient chamber, are depicted in **Fig. 6.1.2**.

The branched microchannel array facilitates fluid stream mixing as it flows into the microfluidic channels. The branching allows repeated splitting of streams at nodes, combining them with neighboring streams, and enabling mixing through diffusion in the serpentine channels. At the end of the network, streams with different fluid concentrations converge in the culture chamber. As diffusion is slower compared to the time required to traverse the channels, a concentration gradient perpendicular to the flow direction is maintained. CFD simulations using COMSOL® Multiphysics software correlated flow rates with the formation of a linear citric

acid gradient in the chip's culture chamber. The software, known for its versatility in simulating various physical phenomena, provided a user-friendly interface for concentration profile studies.

**Fig. 6.1.2 A** displays the CFD simulation of citric acid concentration distribution under a flow rate of 12.5 µl/min, showcasing a stepwise gradient profile. **Fig. 6.1.2 D** presents experimental analysis using Rhodamine isocyanate fluorescent dye, validating the formation of a linear gradient inside the culture chamber. Fluorescence images were captured using a confocal microscope.

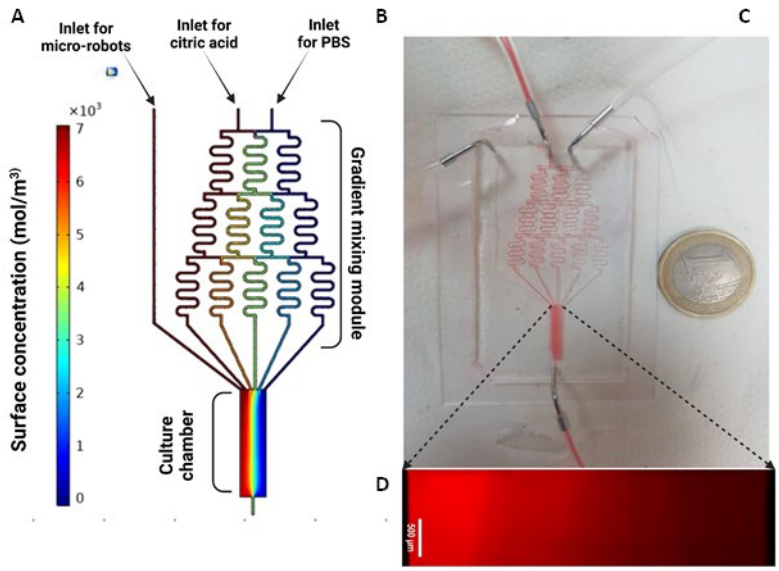


**Figure 6.1.2.** CFD simulation of citric acid concentration gradient (A). Final PDMS device and gradient formation by using food dye (B-C). Gradient formation into the channel observed at the confocal microscope by using Rhodamine B fluorescent dye.

### 6.1.3.3. Propulsion of microrobots inside the microfluidic device

To validate microrobot propulsion, a preliminary test infused microrobots into the gradient chip after achieving the citric acid gradient. Loaded with sodium bicarbonate, the microrobots, upon contact with the citric acid solution, moved chemically to the opposite chip wall. Confocal images documented the microrobot trajectory (**Fig. 6.1.3**).

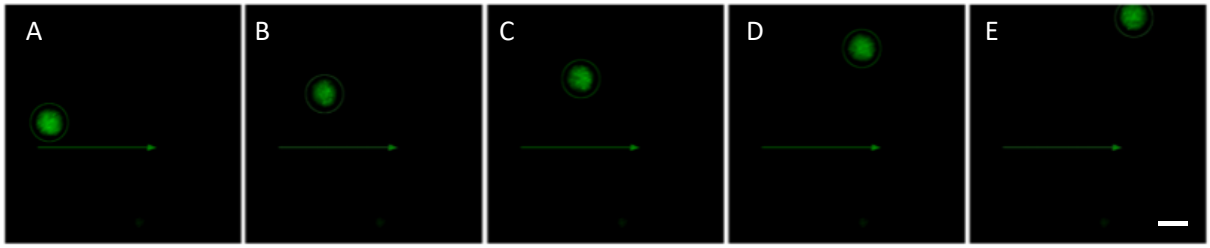


**Figure 6.1.3.** Confocal images of alginate microparticles (green) trajectory in the microfluidic device when a linear gradient of citric acid was present. Scale bar is 100 µm.

### 6.1.3.4. Microrobots targeting Caco-2 cells in the gradient microfluidic device

Caco-2 cells underwent dynamic cultivation inside the culture chamber of the gradient mixing microfluidic device for a period of 5 days. The selected volumetric flow rate was 5 µl/min, corresponding to a shear stress of $1.5 * 10^4$ dyne/cm$^2$. This choice closely mirrors the physiological levels of intestinal epithelial shear stress, falling within the range of approximately 0.002 dyne/cm$^2$ to 0.08 dyne/cm$^2$[65]. The dynamic environment experienced by Caco-2 cells within the microfluidic chip is known to influence their differentiation and maturation[31]. Consequently, we allowed the cells to proliferate and differentiate within the chip.

Following the 5-day period, Hoechst staining was employed to assess cell confluence and distribution inside the culture chamber. Despite the absence of transepithelial electrical resistance integration for gut barrier integrity, **Fig. 6.1.4 A** illustrates the cells densely packed together, forming a confluent monolayer with cells occupying different focal planes.

After confirming the uniform distribution of cells, we proceeded to assess cell viability. Live/dead cell membrane staining (**Fig. 6.1.4 B-C**) revealed that the majority of cells were alive. This indicates correct cell adhesion to PMMA facilitated by collagen treatment, coupled with the dynamic conditions that fostered faster cellular growth compared to static and conventional platforms such as Petri dishes or Transwell®.

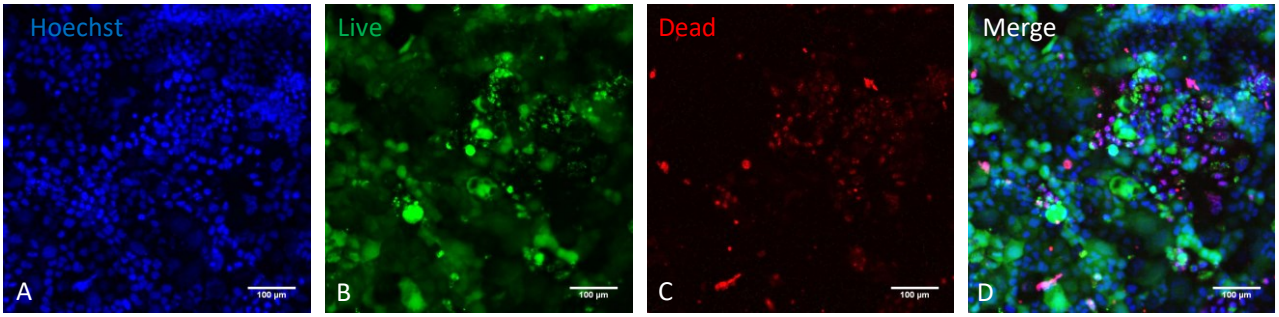


**Figure 6.1.4.** Fluorescent images of Caco-2 monolayer formed in the culture chamber in the microfluidic device. Nuclei were stained in blue (A); live cells in green (B); dead cells in red (C). Composite image of the three channels (D). Scale bar is 100 µm.

To evaluate the accumulation of microrobots within the simulated gut tissue's mucus layer in the microfluidic device, we examined microrobot propulsion through confocal microscope analysis. The polymeric microrobots were introduced into the chip through the appropriate inlet. Simultaneously, a linear citric acid gradient was established in the culture chamber.

Upon contact with citric acid, the microrobots exhibited a propulsion effect, utilizing $CO_2$ released from the reaction between citric acid and sodium bicarbonate. This propelled the microrobots towards the Caco-2 cells, forming a bond with them (**Fig. 6.1.5**).

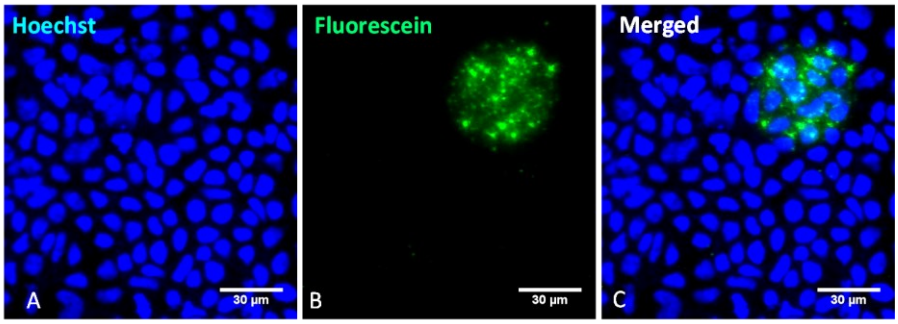


**Figure 6.1.5.** Fluorescent image of Caco-2 monolayer formed in the culture chamber in the microfluidic device. Nuclei were stained in blue (A); alginate microparticles were stained in green (B). Composite image of the two channels showing the interaction between cells and particles. Scale bar is 30 µm.

### 6.1.4. Conclusion

This article introduces a promising strategy in the realm of drug delivery utilizing soft micro-robots composed of natural and biodegradable materials, specifically alginate. The incorporation of sodium bicarbonate enables precise propulsion towards the gut mucosa, achieved through bubble formation due to the citric acid gradient established upon the degradation of a commercial capsule containing the comprehensive formulation of microrobots and citric acid powders. These microrobots have the potential to carry various drugs or probiotics, combined with sodium bicarbonate, allowing for a gradual release in proximity to the cell layer. This approach holds promise in overcoming the constraints associated with traditional drug delivery methods.

While these findings were obtained in a microfluidic platform designed to emulate the in-vivo intestinal microenvironment, additional investigations, such as *in-vivo* tests, are imperative to further evaluate the properties, capabilities, and safety of the microrobots.

## 6.2. Production and characterization of oil-in-water nanoemulsions for oral delivery of nutraceuticals

### 6.2.1. Introduction

Nutraceuticals are defined as substances that have a therapeutic effect on the health of human beings and provide protection against chronic diseases. They can be used for nutrition but also to prevent and treat pathological conditions by reducing, delaying or even avoiding the need of pharmaceuticals, due to their high nutritional values and optimal safety profile with just few side effects[32]. The term nutraceutical is often used improperly to indicate other categories of food products such as pre- and pro-biotics, functional foods and food supplements, although there are significant differences[33]. For instance, a dietary supplement is a derived food product that must be included as part of the diet to receive its beneficial health effects. These supplements, as well as functional foods, can compensate and/or have a beneficial effect in case of micro or macronutrient deficiencies and do not necessarily need to have a proven pharmacological effect[34]. On the other hand, nutraceuticals must have proven clinical efficacy beyond their nutritional value, therefore they can be effectively used to prevent and treat certain pathological conditions, as demonstrated by several clinical trials[35,36].

Nutraceuticals include a vast category of chemical compounds extracted from natural sources such as lipids, phenolic compounds, vitamins, and bioactive peptides. Some examples are ginseng, glucosamine, omega-3, lutein, folic acid, curcumin, resveratrol, quercitin and so on. Most nutraceuticals have multiple therapeutic properties: they improve cognitive health, regulate blood pressure and cholesterol levels, reduce inflammation, and prevent cardiovascular disorders and chronic diseases. In particular, they can influence pathological processes triggered by oxidative stress, a process typical of many pathologies such as Alzheimer's, cancer, diabetes, inflammatory diseases, Parkinson's, and obesity[32,37]. Nutraceuticals can be classified by their natural sources, pharmacological conditions, mechanism of action, or chemical nature[38]. Many nutraceuticals show often limited bioavailability, principally due to their chemical structures, determining an incomplete uptake which results in a large percentage of the compound not being absorbed and eliminated from the body untouched.

The oral bioavailability of a compound is defined as the quantity of the ingested compound over the fraction that reaches systemic circulation in an active form which is then distributed in the specific site of action. Any therapeutic agent, including nutraceuticals, is considered effective only if it reaches and distributes to tissues and organs where it can exert beneficial health effects. These effects may be influenced by limited bioaccessibility, poor absorption, chemical transformation within the GIT, or during first-pass metabolism.

For a compound to be absorbed at the intestinal level, it must pass the GIT, be solubilized at the level of the intestinal lumen, and possess a certain hydrophilic/lipophilic balance that allows it to cross the intestinal membrane. The intestinal absorption of a nutraceutical can take place through the trans-cellular or para-cellular

route and exploit passive or active transport mechanisms. Passive transport allows the compound to cross the cell membranes thanks to a concentration gradient, while active transport takes advantage of transmembrane transport systems which, consuming energy, allow the entry of the compounds into the cell.

Another aspect to be considered is first-pass metabolism since, through first and second-phase chemical reactions, the original compound can be transformed into a metabolite losing its biological activity. Biotransformations reduce the amount of bioactive compounds in the blood or limit their bioavailability. Furthermore, there can be alterations over time that might affect the shelf-life of the product. The entity of this alteration and the chemical reaction pathway undergone depend on the nature of the compound, the formulation, and the environmental conditions such as pH, temperature, and light[39,40]. Researches show that the bioavailability of many poorly water-soluble drugs can be improved through the use of nano-carrier-based delivery systems[41]. The high surface area of these systems allows for rapid drug dissolution in the GIT. The increase in bioavailability depends on particle composition, size, and interfacial properties. All of these properties should be taken into account and optimized to develop an efficient delivery system. As a consequence, there is great interest in developing nano-sized delivery systems for nutraceuticals and other bioactive components found in foods[41].

The mechanisms that lead to an increase in bioavailability are based on the improvement of critical issues, namely:

- Improvement of the solubility of the bioactive compound in gastrointestinal conditions;
- Protection of the bioactive compound from chemical conditions in the GIT;
- Controlled release within the GIT;
- Enhanced transfer across the intestinal wall.

The increase in bioavailability obtained through nano-carriers is not only due to their nanometric dimensions but also to their surface properties and the presence of crystalline structures[42].

Nanotechnologies are potentially able to revolutionize delivery systems for nutraceuticals by employing nano-carriers to deliver drugs and adapting to obtain food-grade nano-systems. During the last few years, numerous engineered nanometer-sized materials have been proposed to overcome solubility incompatibilities between bioactive compounds and the food matrices, to protect sensitive ingredients or nutritionally relevant compounds from degradation, to increase the bioavailability, and to modify the physical properties of food materials. Various structures can be produced such as microemulsions, liposomes, nanoemulsions, microgels and others[42].

Such systems can be prepared starting from food-grade materials (proteins, polysaccharides, lipids, minerals, and surfactants) using two different methods: "top-down" and "bottom-up".

In the top-down approach, nano-carriers are fabricated thanks to the fragmentation of larger structures into smaller ones usually by using mechanical and/or thermal energy. In bottom-up methods, nano-carriers are manufactured by assembling small molecules or particles. Homogenization is a classic example of the top-down method, while micellization and anti-solvent precipitation are examples of nano-carrier production by bottom-up procedures. The choice of a particular nano-encapsulation technology for a specific application is affected by many factors such as the type of nutraceutical to be delivered, safety, the size of the nano-carrier required, the chemical-physical properties of the materials that constitute the core and the coating, food matrix compatibility, release mechanism, robustness, performance, labeling requirements, process costs, and commercial viability[41]. The components used to construct a nanoscale delivery system are important to determine its functional properties, like antioxidant capacity, digestibility, density, and stability. The use of lipid and surfactant-based systems is currently the most pursued approach in the pharmaceutical and food industries. Lipid formulations can be easily produced using technologies already widely used such as high-pressure homogenization and micro-fluidization. These systems, to be usable and marketable, must be safe for food use, economically advantageous, and must not negatively influence the sensory properties of the product[41,43,44].

NEs are colloidal dispersions of small droplets, typically between 20 and 500 nm of one fluid dispersed in another immiscible fluid. Depending on the nature of the dispersing phase, NEs are divided into O/W and water-in-oil types. O/W NEs are made of small oil droplets dispersed within water, whereas W/O NEs consist of small water droplets dispersed in oil.

O/W NEs are widely used as delivery systems for encapsulation and delivery purposes due to the numerous advantages they offer[45–47]:

- They can be prepared from generally recognized as safe raw materials and using simple processes compared to multiple emulsions and solid lipid nanoparticles;
- They are of particular interest to the food industry as food-grade oils and emulsifiers are easily available;
- They can increase the bioavailability of lipophilic bioactive compounds thanks to the oil core and the small size of the nano-carrier;
- They can protect the compounds encapsulated during the preparation procedures, preserving the physio-chemical stability of the product and its organoleptic properties;
- They are much more stable to separation (creaming/sedimentation) or droplet aggregation (coalescence/ flocculation);
- They can be used for different routes of administration.

There are always three basic elements in an emulsion: oily phase, aqueous phase, and emulsifier. The emulsifying agent represents a fundamental element for the preparation of an emulsion since it is able to place

itself at the interface between the two phases by decreasing the surface tension. Emulsifying agents can be classified according to their chemical composition, synthetic or natural, or the type of film they form. The type of emulsion is determined by the kind of emulsifying agent used, by the ratio between volumes of the phases (the most abundant component constitutes the dispersing phase), by the viscosity of the phases, and by the method of preparation[48]. The NEs can be prepared using high-energy procedures. They consist in the use of mechanical tools capable of generating intense destructive forces, breaking the oil phase and the water phase and leading to the formation of small globules. Among these tools, the most used are high-pressure homogenizers, microfluidizers and sonicators[46,49–52]. Regarding the problems encountered in the formation of NEs, the most crucial one is the ability to obtain a mono-disperse emulsion with small globules. This is influenced by the type of homogenizer used, the operating conditions (temperature, pressure, time), the composition of the sample (type of oil and emulsifier used and relative concentrations of use), and the physio-chemical properties of the components (interfacial tension, viscosity). The concentration of the emulsifier is one of the factors that influence the most the size of the globules and the dimensional homogeneity. In general, the higher the concentration of the emulsifier used, the smaller the size of the globules obtained and the greater the dimensional homogeneity[51]. The stability of NEs depends on its composition and structure and on environmental conditions like pH, ionic strength, temperature, light, oxygen concentration, and mechanical forces[53]. The stability of a liquid-liquid interface can be increased through the formation of a layer around the lipid globules of the dispersed phase. This laminar coating can be formed from different substances such as liquids or solid particles, and polymers. An example of this type of approach is the layer-by-layer strategy which permits the stabilization of emulsions through the sequential deposition of oppositely charged polyelectrolytes[54–56].

An emulsion made up of small globules covered by a thin layer of emulsifier is indicated with the term primary emulsion, the addition of a subsequent layer of polyelectrolyte, provides a SNE, which can be indicated with the term “monolayer”[57]. The formation of SNEs can be done by different procedures. The saturation method is one of the most implemented. It consists of adding a quantity of polyelectrolyte to minimize the free fraction in the dispersed phase, while completely coating the particles. The stability of these systems is achieved when the magnitude of the electric charge densities of both types of particles is high enough to generate a strong electrostatic repulsion between the particles. However, when the electric charge density is not sufficient, the systems thus constituted tend to aggregate[58].

The stability of SNEs can be enhanced by re-dispersion using high-pressure homogenization. It allows to destroy aggregates, thicken the polyelectrolyte coating around the dispersed phase and obtain very stable emulsions over time, provided they are associated with a suitable coating concentration[54]. Polymeric compounds are the most used substances for the formation of a coating around the lipid globules as, in addition to electrostatic interactions, they can be functionalized allowing to add further characteristics to the carrier. Polymers with mucoadhesive properties are widely used for the coating of nano-carriers as they adhere to the mucous membranes, increasing the residence time and consequently the absorption of the drug[59]. Among

polymers, polysaccharides are widely used to obtain a stable coating. A polysaccharide is a carbohydrate containing a large number of monosaccharide units joined together by glycosidic bonds. Their use is very advantageous as they are non-toxic, biocompatible, biodegradable and easily modified by functionalization reaCtions[60,61]. Ct is a polycationic polysaccharide consisting of D-glucosamine (pKa ≈ 6.5-7.0) and N-acetyl-D-glucosamine (neutral) subunits, joined by β- (1,4') linkages–glycosides.

Ct is obtained by deacetylation of chitin, a polysaccharide contained in the exoskeleton of crustaceans and insects and in some types of fungi. Chitin is less used in the pharmaceutical field due to its poor solubility in aqueous solvents. Ct is known to act as a permeation enhancer by opening the tight junctions of the epithelium, facilitating both bioactive compounds' paracellular and transcellular transport. In fact, being positively charged, it interacts with the negatively charged mucus to form a complex by ionic or hydrogen bonding, as well as through hydrophobic interaCtions[62,63]. All these properties make Ct an ideal polymer for the preparation of new delivery systems[64].

One of the most important applications of NEs within the food industry has been to increase the bioavailability of beneficial bioactive substances, such as oil-soluble vitamins and phytochemicals. Different events that occur in the human GIT and body influence the bioavailability, in particular the bioaccessibility, absorption, distribution, metabolism, and excretion of the bioactive substance over time.

Bioaccessibility represents the percentage of the substance inside the GIT fluids that can be absorbed. For hydrophobic substances, this is usually the fraction solubilized within the mixed micelle phase.

Absorption constitutes the fraction of the bioaccessible substance in the gut that passes through the cell epithelium and enters the systemic circulation.

Distribution expresses the portion of the bioactive substance present at the site of action, which considers that the absorbed substance is distributed to various tissues and organs around the human body.

Metabolism is the portion of a substance remaining within a biologically active form at the site of action, taking into account any chemical or metabolic changes that have occurred inside the gut and body.

Excretion is the fraction of a substance remaining at the site of action after the normal excretion processes operating in the body, i.e., urine, feces, breath, or sweat, have occurred.

In case of NEs, bioaccessibility can be calculated as the fraction taken up by the mixed micelles in the small intestine:

$$B^* = 100 \times \frac{c_M}{c_T}$$

here, $c_M$ and $c_T$ are the concentrations of the bioactive substance present in the mixed micelle phase and in the total digest, respectively. In fact, hydrophobic bioactives are solubilized within the hydrophobic interiors of the mixed micelles and then carried to the epithelium cells where they can be absorbed.

One of the advantages of using NEs to increase the bioavailability of hydrophobic substances is that they are rapidly and completely digested in the small intestine. Moreover, they rapidly form mixed micelles that can solubilize the released hydrophobic substances. The hydrophobic domains inside the mixed micelles must be sufficiently large to accommodate the bioactive substances otherwise they will remain in the aqueous phase and may crystallize or form a separate oily phase, which reduces their bioaccessibility. In general, the size, composition, and physical state of the lipid droplets in NEs have to be optimized to increase their bioaccessibility.

## 6.2.2. Materials and Methods

### 6.2.2.1. O/W nanoemulsions preparation

O/W NEs were prepared according to a process protocol previously reported with some modifications. In details, the oil phase was prepared by adding a 5.76g of Lipoid E 80 (Lipoid, Germany), previously weighed on a high-precision scale, to a 24ml of soybean oil (Sigma-Aldrich, USA). The oil phase was mixed, at a temperature of 60°C and a speed of 500 rpm, using a high-speed blender (RZR 2102 control, Heidolph, Germany) until lecithin was completely dissolved. Then, in the case of Cur (Sigma-Aldrich, USA), 100 mg of the drug were added to the oil phase and mixed at 60°C under gentle stirring for 15 minutes in dark conditions. In the case of CoQ10 (Faravelli, Italy), 4.08g of the drug were added to the oil phase and mixed at 60°C for 1 hour in dark conditions. Instead, in the case of tomato peel extracts (lycopene), the oil already contained the biomolecule due to a previous extraction and enrichment process (Tomates del Guadiana, Spain).

Then, the oil phase was added dropwise to a weighed amount of aqueous phase (Milli-Q water) and mixed using a turboemulsifier (Silverson L5T, USA) for 15 minutes at 7000 RPM. The obtained pre-emulsion was finally passed at 2000 bar through the high-pressure valve homogenizer (Microfluidics M110PS, USA). Three individual cycles were made to strongly reduce the initial size. Subsequently, the process continued by refilling the reservoir for 200 subsequent steps, thus recycling the product without any loss of volume. This method was used for the preparation of standard O/W NEs at 20 wt% of oil in water. Variations to this procedure in terms of oil concentration and number and kind of homogenization processes were also explored.

### 6.2.2.2 Ct-FITC Preparation

For the fluorescence analysis, chitosan (Ct, low molecular weight, Sigma-Aldrich, USA) was chemically labelled with Fluorescein 5(6)-isothiocyanate (FITC, Sigma-Aldrich, USA), as reported in a previous work[55]. Briefly, 100 mg of Ct (0.50 mmol) was dissolved in 10 ml of 0.1 M of acetic acid solution. After complete dissolution, a solution of FITC (5.0 mg in 500 μL of DMSO) was added dropwise. The reaction proceeded

overnight at room temperature. The resulting mixture was then precipitated by adjusting the pH to 10 using NaOH, and the precipitate was collected through centrifugation (Thermo-Scientific SL16R, USA, 9000 rpm, 15 min). The sample was washed with MilliQ water through several centrifugation steps. Finally, the purified product was freeze-dried (Freeze Dryer CHRIST Alpha 1–4 LSC, Martin Christ, Germany) for 48 hours.

#### 6.2.2.3. Secondary NEs preparation

To make SNEs, commonly referred to as monolayers, each NE, containing 20 wt% of oil phase, was quickly added to a Ct solution and kept under vigorous stirring for 15 min to ensure uniform Ct deposition. The final concentrations of oil and Ct were 10 and 0.1 wt%, respectively. These SNEs were passed through a high-pressure valve homogenizer at 700 bar for 108 continuous steps and re-processed after two days under the same conditions.

All the SNEs were stored at 4°C and monitored over time to evaluate their stability.

#### 6.2.2.4. Nanoemulsions characterization

The size and distribution of both primary NEs and SNEs were measured using a laser dynamic light scattering technique ($\lambda$ = 632.8nm) (Zetasizer Nanoseries, Malvern, UK). These parameters play a crucial role in characterizing and defining the type and stability of NEs. The PDI describes the uniformity of the globules in the dispersed phase. High PDI values indicate low dimensional globules uniformity, while low values suggest a monodisperse emulsion with high stability due to reduced Ostwald ripening. Dynamic light scattering instrument correlates the fluctuations of intensity I(t) of scattered light during the time with the Brownian motion of colloidal particles and then with the diffusion coefficient related to the hydrodynamic radius of the particles. All the samples were diluted up to a droplet concentration of 0.25 wt% by using Milli-Q water in the case of primary NEs and an acetic acid 20 mM solution in the case of Ct-based SNEs and were poured into disposable cells. Using the same dilutions, the $\zeta$-potential of the NEs was determined using a particle electrophoresis instrument (Zetasizer Nanoseries, Malvern, UK), by measuring the direction and velocity of droplet movements in a well-defined electric field. This parameter represents the electrical potential present at the shear plane, which is the distance from the droplet surface below which the counter-ions maintain a strong attachment to the droplet when it is subjected to an electrical field[48]. The $\zeta$-potential is calculated from the electrophoretic mobility based on Smoluchowski's equation:

$$\upsilon = (\varepsilon E / \eta) \cdot \zeta$$

Where $\upsilon$ is a measure of the electrophoretic velocity, $\eta$ is the viscosity, $\varepsilon$ is the electrical permittivity of the electrolyte solution, and E is the applied electric field.

The size and the $\zeta$-potential were determined at 25°C at least three times for each sample.

#### 6.2.2.5. Nanoemulsion oil concentrations optimization

To optimize the oil concentration, primary NEs at 30, 35, and 40 wt% of oil phase in water were prepared using the same protocol described before, changing the amount of oil and lecithin without inserting any nutraceutical:

- 35.4 ml of soybean oil were mixed with 8.48 g of Lipoid E 80 for the 30 wt% of oil phase;
- 41.3 ml of soybean oil were mixed with 9.91 g of Lipoid E 80 for the 35 wt% of oil phase;
- 47.23 ml of soybean oil were mixed with 11.36 g of Lipoid E 80 for the 40 wt% of oil phase.

Also, SNEs were prepared with the same procedure described before:

- Starting with the primary NEs containing 30 wt% of oil phase, a monolayer with 15 wt% of oil phase and 0.15 wt% of Ct was obtained. Similarly, using the same primary NEs, a monolayer with 20 wt% of oil phase and 0.2 wt% of Ct was prepared. This monolayer was subsequently diluted with water to a concentration of 10 wt% of oil phase and 0.1 wt% of Ct, and the mixture was re-processed for a second time;
- Starting from the primary NE at 35 wt% of oil phase, a monolayer at 20 wt% of oil phase and 0.2 wt% of Ct was obtained;
- Starting from the primary NE at 40 wt% of oil phase, a monolayer at 25 wt% of oil phase and 0.25 wt% of Ct was obtained.

For what concerns NEs with nutraceuticals, a cur NE at 30 wt% of oil phase was prepared, and from this, a SNE at 15 wt% of oil phase and 0,15 wt% of Ct was obtained. Cur to oil ratio was the same of previously discussed NEs.

All these NEs were stored at 4°C and characterized as previously discussed.

#### 6.2.2.6. Nanoemulsion scale-up

To start a scale-up process, 20% wt O/W NEs with no nutraceuticals were prepared as reported in a previous section, but with an overall volume three times larger (360 ml). In this case, the pre-emulsions were passed at 2000 bar through the high-pressure valve homogenizer for thirteen individual cycles. This approach corresponds to the usual 3 individual cycles and the 200 subsequent refilling steps but it was preferred as it appeared to be a more scalable procedure.

#### 6.2.2.7. Nanoemulsion digestion with INFOGEST protocol

A simulated GIT model comprising the mouth, stomach, and intestine was used according to the INFOGEST network[65] to investigate how the Cur monolayer containing 10 wt% of oil and 0.1 wt% of Ct behaves during digestion. To simulate the mouth phase, 3 ml of SSF and 9 µl of 0.5 M $CaCl_2(H_2O)_2$ were mixed with 3 ml of

SNE. Then, the mixture was incubated in an incubator shaker for 1 minute at 37 °C to mimic agitation in the mouth. For the stomach stage, 6 mL of the bolus sample resulting from the mouth phase were mixed with 5.58 mL of SGF and 2.4 µl of $CaCl_2(H_2O)_2$. Then, 420 µl of porcine pepsin (14.37 mg/ml) were added, and the pH was adjusted to 3 with HCl. This mixture is incubated for 2 hours at 37 °C to mimic stomach conditions. To simulate the duodenal phase, 9 ml of chyme sample from the stomach phase were mixed with 8.99 ml of simulated intestinal fluid (SIF) and 11.25 µl of 0.5 M $CaCl_2(H_2O)_2$. Then, 104.79 mg of bile bovine and 248.4 mg of porcine pancreatin were added, and the pH was adjusted to 7 with NaOH. This mixture was incubated for 2 hours at 37 °C. Samples were collected at the end of the gastric phase and every thirteen minutes during the duodenal phase. To stop the enzymatic activity, samples were treated with a Pefabloc solution (24mg/ml).

After *in-vitro* digestion, an aliquot of the total digest sample was centrifuged at 12500 rpm at 4°C for 30 min. The resulting supernatant was collected as the mixed micelle fraction of the samples.

The average particle diameter and particle size distribution of the samples were determined utilizing the dynamic light scattering technique, as mentioned previously, while the ζ-potential was measured using the electrophoresis technique. Samples were diluted with a buffer solution before analysis. This dilution step was implemented to ensure accurate measurements and mitigate any potential interference caused by multiple scattering.

Cur concentration in the initial SNEs, mixed micelle fraction, and total digest fraction were measured using UV-visible spectroscopy (Varian Cary 100 Spectrophotometer, Australia), which measures the absorbance of light. UV-visible spectrophotometers direct a light source through a sample, and a detector on the opposite side records transmitted light. The light intensity, I, is measured considering a reference, $I_0$. Light absorbance, A, is proportional to the path length through the sample, b, concentration, C, and a molar absorptivity, ε, that is characteristic for every compound—the Beer-Lambert law:

$$A = \log_{10}\frac{I_0}{I} = \varepsilon \cdot b \cdot C$$

Rearranging this equation, we find the concentration as a function of the known parameters after calibration:

$$C = \frac{1}{\varepsilon \cdot b} \cdot A$$

To determine the Cur concentration, 2 mL of sample were mixed with 2 mL ethanol, vortexed, and centrifuged at 4000 rpm for 10 min at 4°C. The top layer with the solubilized cur was collected, while the bottom layer was mixed with 2 mL of ethanol, and the same procedure was repeated a second time. The top ethanol layer was added to the previous one and the absorbance was measured at 425 nm. Pure ethanol was used as a reference (blank).

Bioaccessibility was defined as the proportion of cur solubilized within the digested sample expressed as a percentage, and was calculated both in respect of the mixed micelle phase and the total digest:

$$\text{Bioaccessibility}_{\text{micelle}}\ (\%) = \frac{C_{\text{micelle}}}{C_{\text{initial}}} \cdot 100$$

$$\text{Bioaccessibility}_{\text{digesta}}\ (\%) = \frac{C_{\text{digesta}}}{C_{\text{initial}}} \cdot 100$$

Where $C_{\text{micelle}}$ is the concentration of cur in the mixed micelle, $C_{\text{digesta}}$ is the concentration of CUR in the digested sample before centrifugation and $C_{\text{initial}}$ is the concentration of Cur in the initial sample before the digestion.

## 6.2.3. Results

### 6.2.3.1 Nanoemulsion stability over time

Delivery systems such as NEs should demonstrate the ability to maintain their physical stability, specifically minimal changes in size, throughout their shelf life. Temperature variations can lead to alterations in the chemical-physical properties of NEs. Therefore, we assessed the physical stability of O/W NEs and SNEs containing cur and lycopene over time by monitoring their size and PDI when stored at 4°C.

The stability of the cur NEs and SNEs was assessed for a duration of up to 120 days from the date of preparation (**Table 6.2.1** and **Fig. 6.2.1 6.2.2**).

**Table 6.2.1.** Time monitoring of size (nm) and PDI parameters for NEs and SNEs with cur

| **DAYS** | **O/W NE 20 WT% OIL** | | **SNE 10 WT% OIL, 0.1 WT% CT** | |
|---|---|---|---|---|
| | **Size [nm]** | **PDI** | **Size [nm]** | **PDI** |
| **0** | 106±1 | 0.09±0.01 | 103.5±0.6 | 0.06±0.005 |
| **2** | 107±0.8 | 0.08±0.02 | 104±0.3 | 0.08±0.009 |
| **20** | 107±2 | 0.09±0.01 | 108±0.2 | 0.08±0.04 |
| **70** | 108±1 | 0.09±0.02 | 112±0.6 | 0.09±0.04 |
| **120** | 109±2 | 0.1±0.03 | 116±1 | 0.1±0.01 |

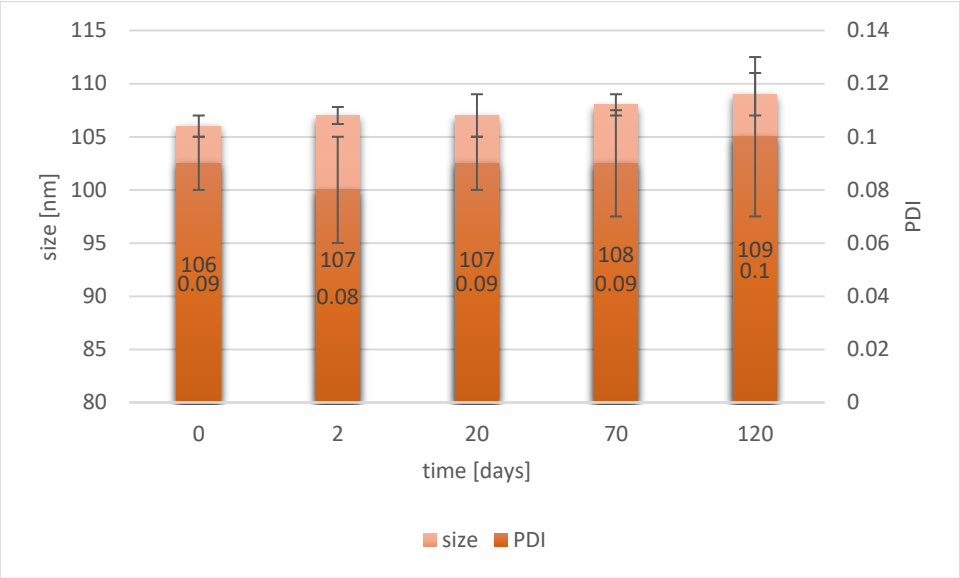


**Figure 6.2.1.** Time monitoring of size (nm) and PDI parameters for primary NEs with cur

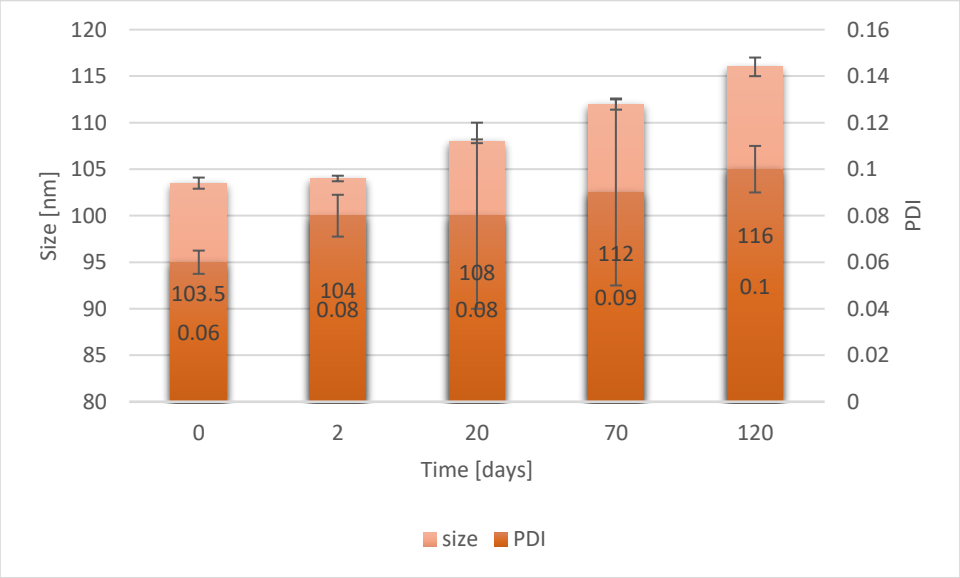


**Figure 6.2.2.** Time monitoring of size (nm) and PDI parameters for SNEs with cur

The dimensions were preserved over time, as the size was within the nanometric range and as the PDI was narrow (approximately 0.1) for both primary NEs and SNEs.

Similarly, the lycopene NEs and SNEs were monitored for 37 days from the date of preparation. Throughout the observation period, the nanometric dimensions remained almost unchanged. Furthermore, the small PDI values indicated a consistent and uniform particle size distribution within the NEs (**Table 6.2.2** and **Fig. 6.2.3 Fig. 6.2.4**).

**Table 6.2.2.** Time monitoring of Size (nm) and PDI parameters for NE and SNE with lycopene.

| DAYS | O/W NE 20 WT% OIL | | SNE 10 WT% OIL, 0.1 WT% CT | |
|---|---|---|---|---|
| | *Size [nm]* | *PDI* | *Size [nm]* | *PDI* |
| **0** | 125±0.1 | 0.06±0.01 | 117±0.3 | 0.08±0.01 |
| **1** | 126±0.7 | 0.09±0.01 | 119±1 | 0.09± 0.01 |
| **8** | 126±0.4 | 0.09±0.004 | 121±1 | 0.09±0.01 |
| **16** | 127±1 | 0.09±0.02 | 122±0.8 | 0.10±0.02 |
| **23** | 131±2 | 0.09±0.01 | 125±2 | 0.09±0.01 |
| **30** | 131±2 | 0.09±0.01 | 130±0.6 | 0.11±0.01 |
| **37** | 133±2 | 0.09±0.01 | 130±2 | 0.11±0.03 |

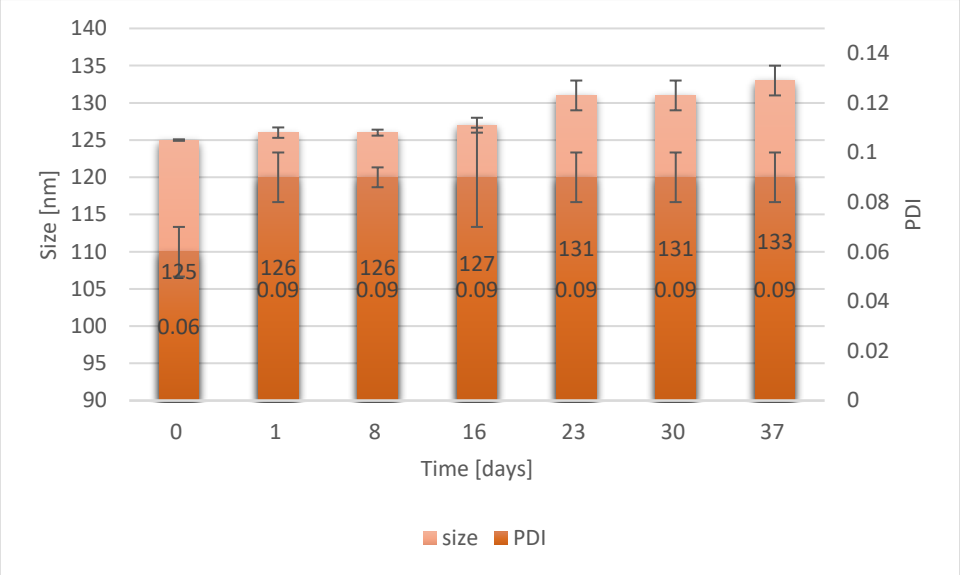


**Figure 6.2.3.** Time monitoring of Size (nm) and PDI parameters for primary NE with lycopene

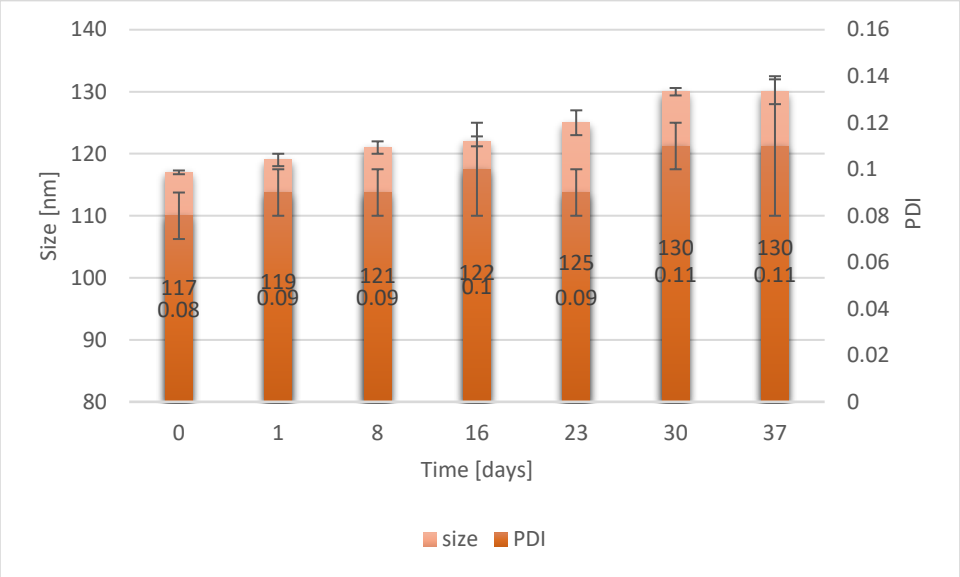


**Figure 6.2.4.** Time monitoring of Size (nm) and PDI parameters for primary SNE with lycopene

### 6.2.3.2 Oil concentration assessment

To explore the possibility to increase the amount of oil in the emulsion which would be advantageous in terms of industrial scale up, primary NEs were prepared at 30, 35, and 40 wt% of the oil phase in water, without nutraceuticals. They were monitored over time using the dynamic light scattering technique to verify and compare their stability.

It was observed that both 30 wt% and 35 wt% NEs exhibited stability for a duration of 120 days starting from the date of preparation (**Table 6.2.3** and **Fig. 6.2.5 Fig. 6.2.6**). However, in the case of the 40 wt% oil NEs, significant changes in size and PDI were noted within 10 days, indicating a pronounced level of instability.

**Table 6.2.3.** Time monitoring of Size (nm) and PDI parameters for O/W NEa with 30 and 35 wt% of oil

| **DAYS** | **O/W NE 30 WT% OIL** | | **O/W NE 35 WT% OIL** | |
|---|---|---|---|---|
| | **Size [nm]** | **PDI** | **Size [nm]** | **PDI** |
| **0** | 94±0.6 | 0.08±0.01 | 99±0.6 | 0.08±0.02 |
| **2** | 97±0.6 | 0.09±0.004 | 100±1 | 0.08±0.01 |
| **20** | 97±0.7 | 0.07±0.03 | 110±1 | 0.1±0.01 |
| **50** | 100±0.5 | 0.09±0.01 | 105±2 | 0.07±0.01 |
| **70** | 98±1 | 0.1±0.01 | 109±1 | 0.11±0.02 |

| | | | | |
|---|---|---|---|---|
| **90** | 101±1 | 0.1±0.02 | 107±2 | 0.09±0.01 |
| **120** | 98±0.2 | 0.08±0.02 | 105±1 | 0.07±0.02 |

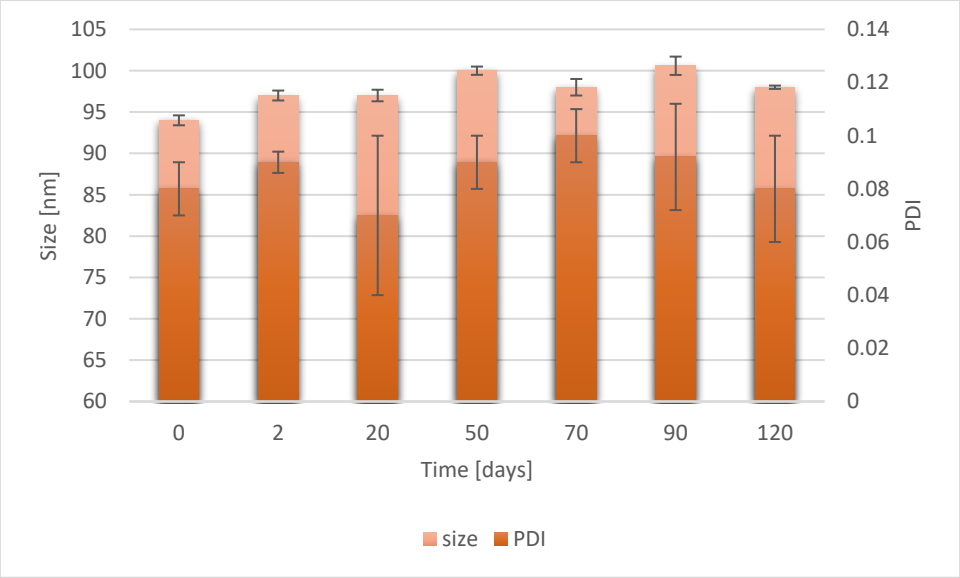


**Figure 6.2.5.** Time monitoring of size (nm) and PDI parameters for O/W NE with 30 wt% oil

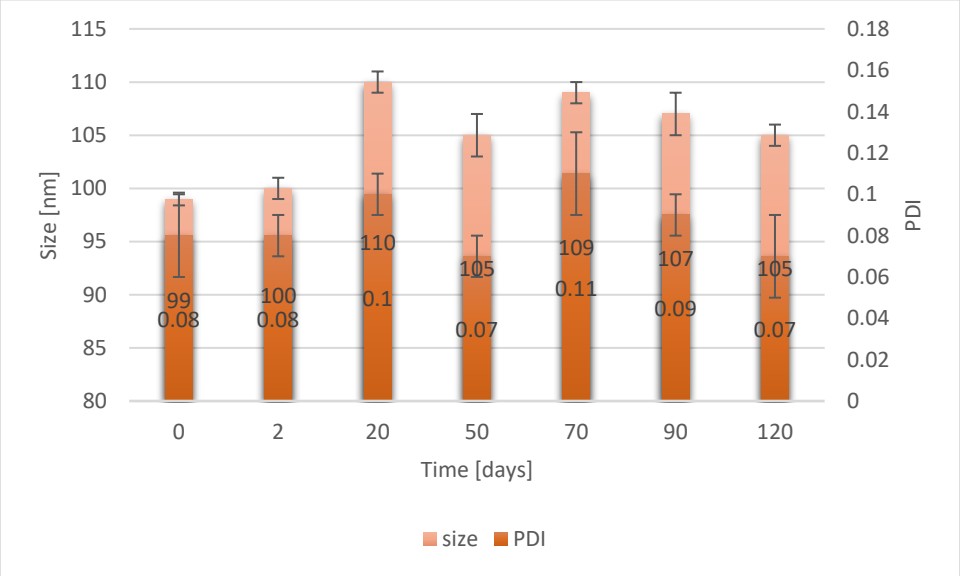


**Figure 6.2.6.** Time monitoring of size (nm) and PDI parameters for O/W NE with 35 wt% oil

These NEs were utilized as substrates to prepare monolayers at different concentrations of oil and Ct, and their stability over time was assessed.

In particular, the monolayer at 10 wt% of oil phase and 0.1 wt% of Ct, obtained from the NEs at 30 wt% of oil, had a better stability over time with respect to the one containing 15 wt% of oil and 0.15 wt% of Ct,

prepared from the same NEs (**Table 6.2.4**). The former remained stable for up to 70 days (**Fig. 6.2.8**), while the latter experienced an initial increase in size and PDI after one week, followed by stable parameters for the next 60 days (**Fig. 6.2.7**).

**Table 6.2.4.** Time monitoring of size (nm) and PDI parameters for SNE at 10 and 15 wt% oil, 0.1 and 0.15 wt% Ct

| DAYS | SNE 15 WT% OIL, 0.15 WT% CT | | SNE 10 WT% OIL, 0.1 WT% CT | |
|---|---|---|---|---|
| | Size [nm] | PDI | Size [nm] | PDI |
| 0 | 98±0.8 | 0.07±0.004 | 97±0.2 | 0.08±0.01 |
| 1 | 98±0.5 | 0.1±0.01 | 99±1 | 0.09±0.02 |
| 7 | 103±0.7 | 0.15±0.002 | 105±3 | 0.1±0.02 |
| 14 | 108±1 | 0.15±0.01 | 108±2 | 0.1±0.02 |
| 21 | 117±2 | 0.15±0.02 | 110±1 | 0.1±0.01 |
| 35 | 123±0.6 | 0.16±0.004 | 116±2 | 0.1±0.03 |
| 70 | 131±1 | 0.16±0.01 | 120±1 | 0.12±0.01 |

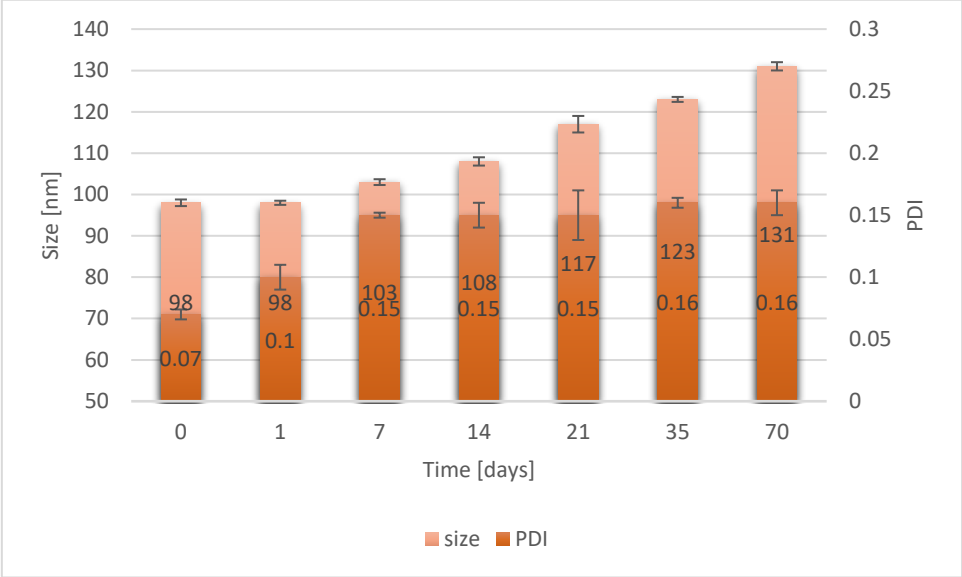


**Figure 6.2.7.** Time monitoring of size (nm) and PDI parameters for SNEs at 15 wt% oil and 0.15 wt% Ct

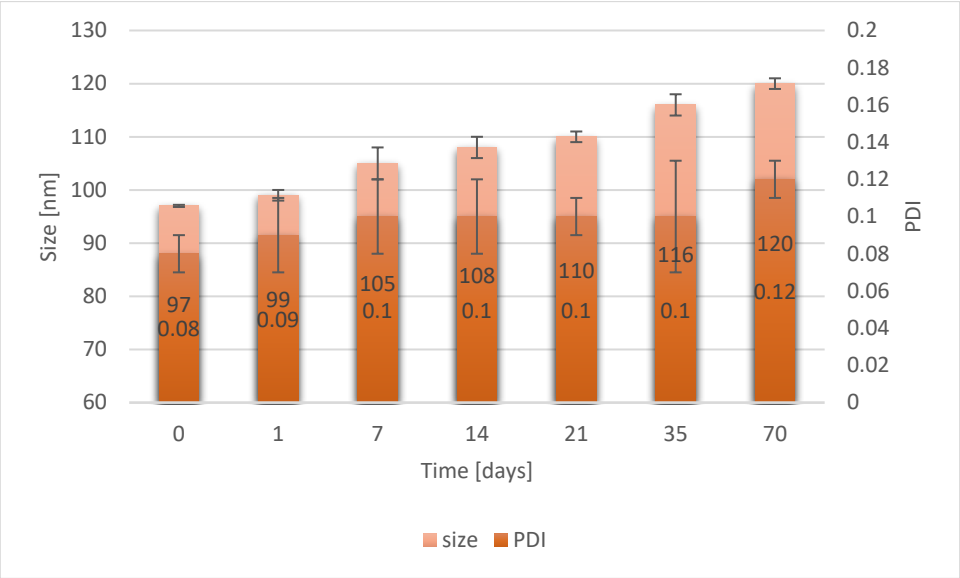


**Figure 6.2.8.** Time monitoring of size (nm) and PDI parameters for SNEs at 10 wt% oil and 0.1 wt% Ct

Diversely, the monolayers derived from NEs with 35 and 40 wt% of oil demonstrated a clear trend of destabilization within the first 10 days (not reported).

Regarding nutraceutical-loaded NEs, the cur NEs at 30 wt% of oil and the SNEs at 15 wt% and 0.15 wt% Ct were monitored for 50 days. From the data obtained, it emerged that these nanosystems were stable for the whole period of observation (**Table 6.2.5** and **Fig. 6.2.9 Fig. 6.2.10**).

**Table 6.2.5.** Time monitoring of Size (nm) and PDI parameters for Cur NE at 30 wt% oil and Cur SNE at 15 wt% oil and 0.15 wt% of Ct.

| **DAYS** | **CUR NE 30 WT% OIL** | | **CUR SNE 15 WT% OIL, 0.15 WT% CT** | |
|---|---|---|---|---|
| | **Size [nm]** | **PDI** | **Size [nm]** | **PDI** |
| **0** | 100±0.2 | 0.08±0.01 | 103±2 | 0.09±0.02 |
| **1** | 102±0.4 | 0.08±0.02 | 103±0.8 | 0.1±0.01 |
| **7** | 101±1 | 0.09±0.004 | 102±1 | 0.1±0.01 |
| **22** | 103±1 | 0.08±0.01 | 104±1 | 0.12±0.01 |
| **50** | 104±0.5 | 0.09±0.01 | 107±2 | 0.11±0.004 |

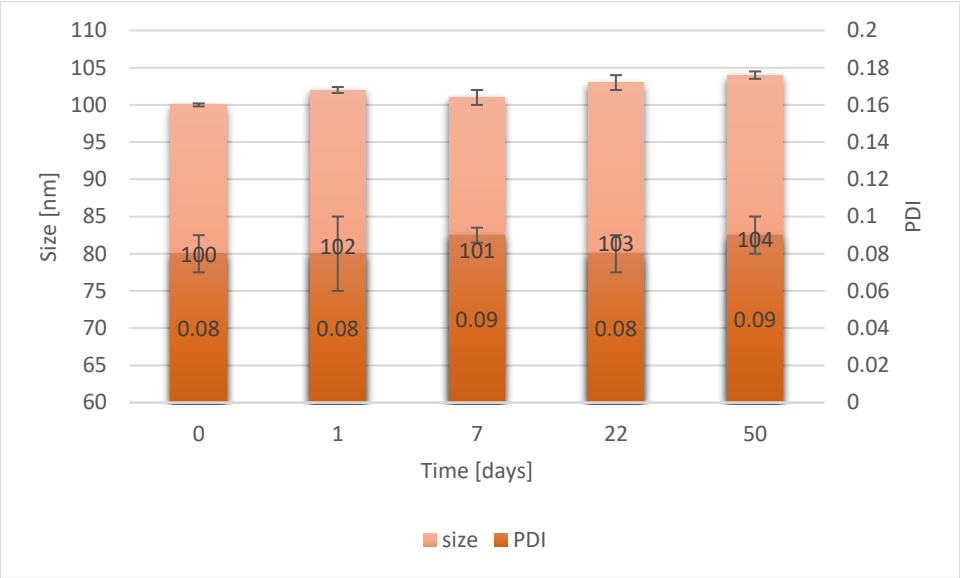


**Figure 6.2.9.** Time monitoring of size (nm) and PDI parameters for cur NEs at 30 wt% oil.

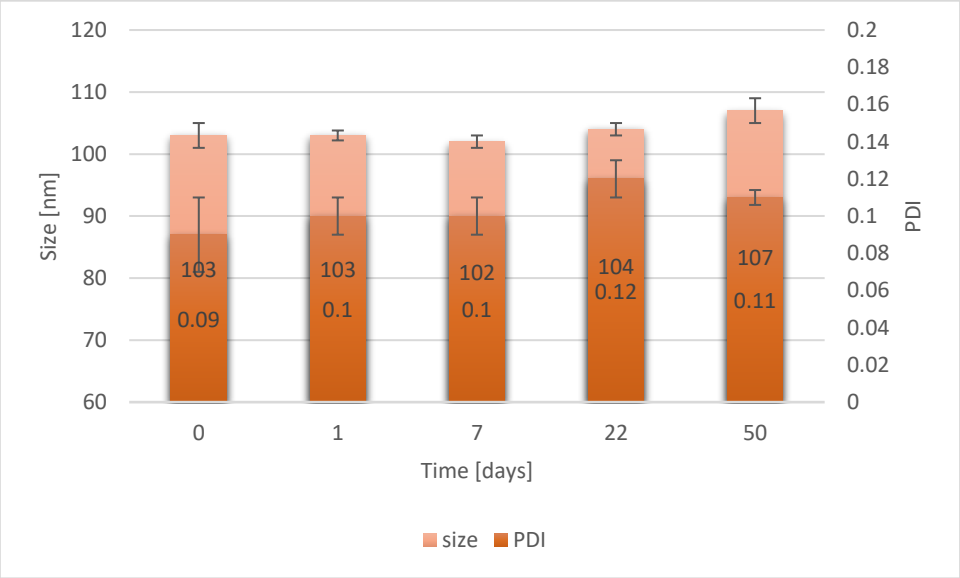


**Figure 6.2.10.** Time monitoring of size (nm) and PDI parameters for cur SNE at 15 wt% oil and 0.15 wt% Ct.

### 6.2.3.3. Scale-up

To understand if and how the protocol used for the preparation of O/W NEs could be rendered scalable, an O/W NE was prepared by triplicating its final volume without adding any nutraceutical. In this case, the pre-emulsion was subjected to thirteen individual cycles of high-pressure valve homogenization at 2000 bar, and an aliquot was collected at the end of each cycle. All samples were analyzed using dynamic light scattering technique.

The results (**Fig. 6.2.11**) revealed an initial decrease in both size and PDI as the number of cycles increased, reaching a plateau thereafter. However, it is noteworthy that the attained size of approximately 120 nm was

slightly higher than the typical size achieved with NEs at standard volumes. Despite this, the PDI successfully reached the desirable value of 0.1, indicating a high level of uniformity and monodispersity. Although the size deviated slightly from the expected norm, the optimized PDI compensated for it, suggesting a favorable overall quality and stability of the NEs. Further experiments are needed to optimize the protocol scale-up.

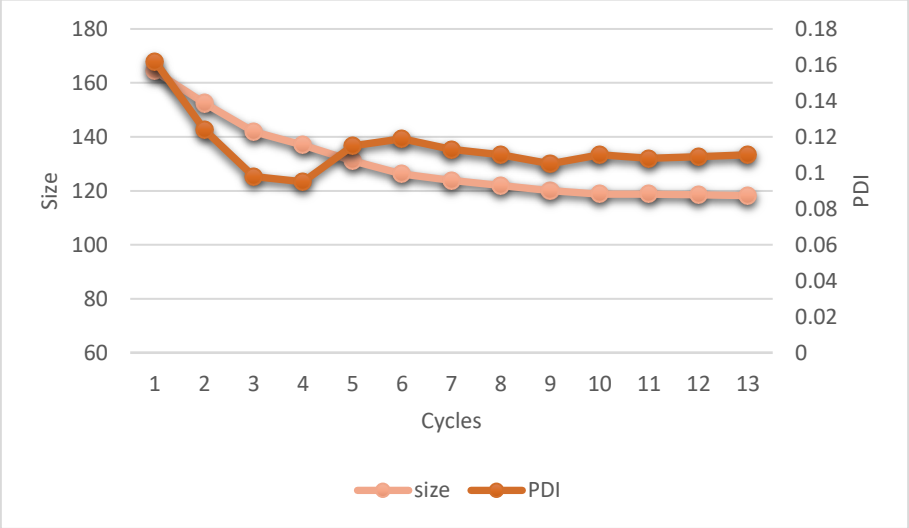


**Figure 6.2.11.** O/W NEs trend for each cycle.

### 6.2.3.4. Nanoemulsion gastrointestinal behavior

To study the behavior of cur SNEs during the digestion process, a simulated GIT model was employed, following the methodology outlined by the INFOGEST protocol and samples were collected at different time points. In order to conduct a comparative analysis, a portion of the digested samples was subjected to centrifugation at 12500 rpm, at a temperature of 4°C, for 30 minutes. Subsequently, the resulting supernatants were collected and, together with the total digest samples, were analyzed.

Following the stomach phase, the size of the SNEs remained quite similar to the measurements obtained in the initial system, both in the centrifuged sample and the uncentrifuged, with a range of approximately 0.129 to 0.143 nm (**Table 4.2.6** and **Fig. 4.2.12**). This indicated that the oil droplets exhibited relative stability against aggregation under the simulated gastric conditions. However, the surface potential experienced a significant decrease after exposure to the stomach phase. In fact, the value became negative, and this might have occurred due to an interaction between the SNEs and the salts present in the SGF.

**Table 6.2.6.** DLS analysis of samples before and after centrifugation

| | Before centrifugation | | | After centrifugation | | |
|---|---|---|---|---|---|---|
| **Digestion phases** | **Size [nm]** | **PDI** | **ζ-potential [mV]** | **Size [nm]** | **PDI** | **ζ-potential [mV]** |
| **Gastric 120** | 143±2 | 0.100±0.003 | -18±2 | 129±0.5 | 0.08±0.02 | -16±1 |
| **Duodenal 05** | 329±13 | 0.6±0.1 | -31±2 | 256±2.3 | 0.40±0.02 | -43±2 |
| **Duodenal 30min** | 378±17 | 0.5±0.1 | -30±2 | 489±9 | 0.49±0.04 | -43±2 |
| **Duodenal 60min** | 576±108 | 0.6±0.04 | -36±1 | 179±2 | 0.34±0.01 | -40±2 |
| **Duodenal 90min** | 374±13 | 0.5±0.03 | -38±0.4 | 157±4 | 0.33±0.04 | -50±2 |
| **Duodenal 120min** | 368±7 | 0.5±0.01 | -38±0.6 | 159±4 | 0.25±0.004 | -43±1 |

Following incubation in simulated small intestinal fluids, the mean particle size and the PDI of the SNEs experienced a significant increase (**Table 6.2.6** and **Fig. 6.2.12**), indicating that it underwent through droplet aggregation and exhibited instability under these conditions. Several physicochemical mechanisms were likely to have contributed to this change. Firstly, surfactant molecules initially present on the surface of the lipid droplets might have been displaced by other surface-active components such as phospholipids, bile salts, lipase, or free fatty acids and monoacylglycerols generated during triacylglycerol digestion. This displacement could have led to alterations in the composition, structure and properties of the interfacial layer surrounding the droplets, potentially reducing their stability against coalescence. Secondly, the emulsified digestible triacylglycerols in the NEs could have been converted to free fatty acids and monoacylglycerols due to the action of adsorbed lipases. This transformation could have caused changes in the internal composition, structure and properties of the lipid droplets, further compromising their coalescence stability. Additionally, complex colloids such as mixed micelles, vesicles and lamellar structures, can be formed during digestion due to interactions among lipid digestion products, bile salts, phospholipids, and calcium. These interactions contribute to the overall behavior and transformations of the emulsion system throughout the digestion process[66]. Also, the ζ-potential of the samples was evaluated, showing a significant difference compared with

the initial NEs (**Table 6.2.6** and **Fig 6.2.13**). The high negative charge in the sample may be due to several reasons. As an example, during exposure to SIF, the presence of anionic bile salts can displace the original surfactant molecules from the surfaces of lipid droplets. This displacement can result in changes to the surface charge of the droplets. Additionally, the hydrolysis of triglycerides catalyzed by pancreatic lipase at the surface of lipid droplets leads to the release of anionic free-fatty acids. The presence of these free fatty acids further contributes to alterations in the surface charge of the droplets[67].

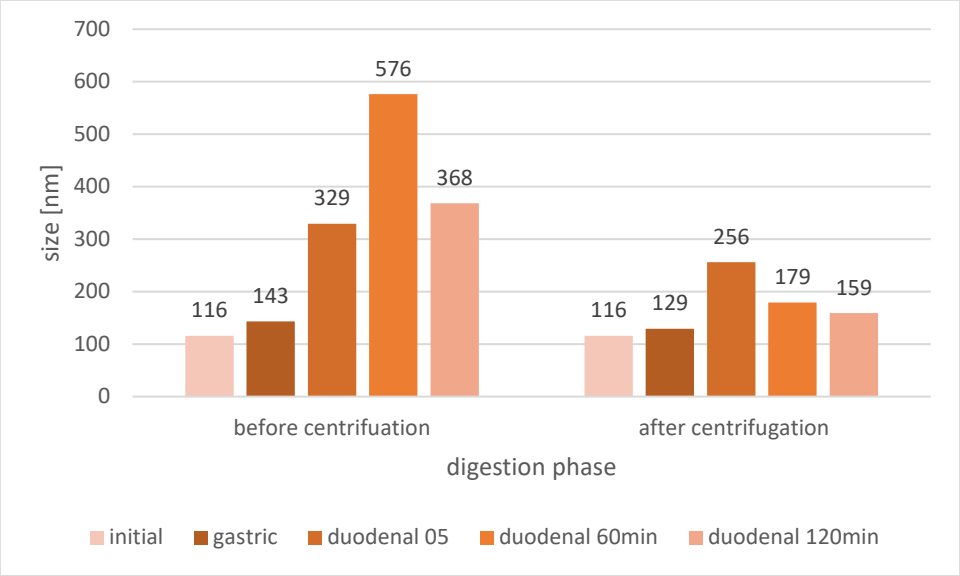


**Figure 6.2.12**. Size changes of cur SNEs during digestion

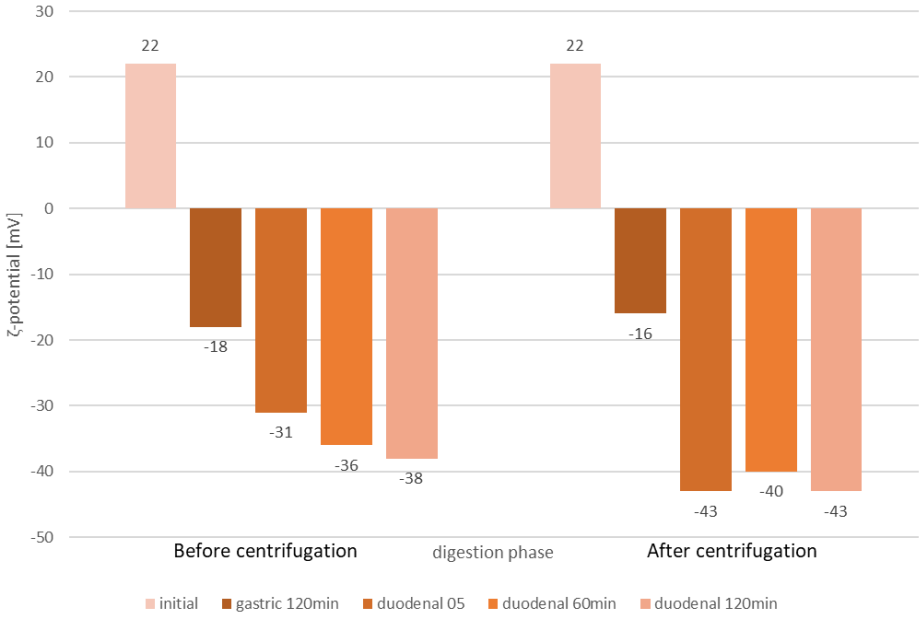


**Figure 6.2.13.** ζ-potential changes of cur SNEs during digestion

The concentration of the SNEs in the gastric samples, both in the centrifuged and uncentrifuged forms, exhibited remarkable similarity to the initial system (**Table 6.2.7** and **Fig. 6.2.14**). This indicated that the SNEs

remained stable within the gastric tract, with the oil droplets effectively protecting the cur from degradation or dilution. The findings suggested that the Ct-coating helped maintaining the concentration of cur in the gastric environment, providing enhanced stability and ensuring its potential therapeutic effects remain intact.

When the system undergoes the duodenal phase, there is a rapid decrement of the concentration and, in particular, the concentration between centrifuged and uncentrifuged samples halves (**Table 6.2.7** and **Fig. 6.2.14**). This observation suggested that the enzymes present in the duodenal tract exhibited rapid activity, leading to the degradation of the emulsion and subsequent release of Cur. Moreover, the significant decrease in concentration, evident in the centrifuged samples compared to the non-centrifuged ones, indicated that a portion of Cur went into the micelle phase while another portion may have remained in solution, forming aggregates and/or in solution still within emulsion but in an aggregated state. In either case, such aggregates were inevitably lost during the centrifugation process. This behavior persisted throughout the digestion process, with the concentration of Cur remaining relatively stable as time progresses. From the initial stages of digestion until the end, the Cur concentration showed minimal variation. Specifically, the quantified values at the end of digestion were found to be 0.07 mg/ml for the non-centrifuged sample and 0.05 mg/ml for the centrifuged one. This suggested that the release of Cur from the emulsion and subsequent migration into the micelle phase or aggregation reaches a relatively steady state during the digestion process.

**Table 6.2.7.** Cur quantification during digestion and bioaccessibility (BC) in duodenal phase

| | $C_{total}$ [mg/ml] | $C_{micelle}$ [mg/ml] | $BC_{total}$ (%) | $BC_{micelle}$ (%) |
|---|---|---|---|---|
| **Gastric 120min** | 0.2 | 0.2 | / | / |
| **Duodenal 05** | 0.08 | 0.04 | 30 | 15 |
| **Duodenal 30min** | 0.1 | 0.05 | 39 | 18 |
| **Duodenal 60min** | 0.1 | 0.05 | 40 | 18 |
| **Duodenal 90min** | 0.1 | 0.04 | 37 | 18 |
| **Duodenal120min** | 0.07 | 0.05 | 28 | 20 |

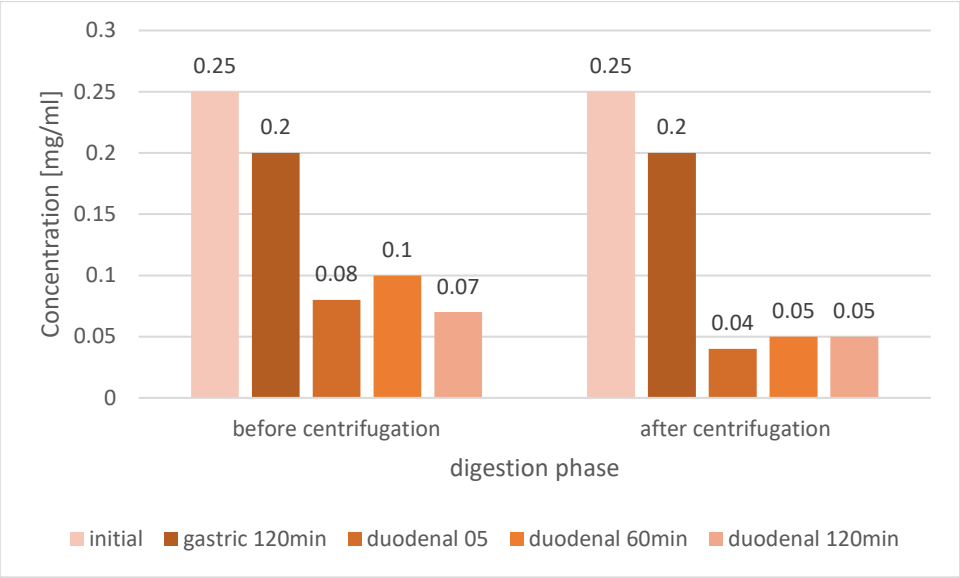


**Figure 6.2.14.** Cur concentration variation

To assess cur bioaccessibility, measurements were conducted before and after centrifugation of the sample. It was hypothesized that the centrifuged samples, which represent the mixed micelle phase, would provide a more accurate representation of the actual bioaccessibility of cur. This assumption was made since the centrifugation process removes larger particles that are less likely to be directly absorbed by epithelial cells.

Indeed, the results obtained (**Fig. 6.2.15**) indicate that the bioaccessibility calculated on the non-centrifuged sample, while higher overall, exhibits more heterogeneous values. On the other hand, the bioaccessibility calculated on the centrifuged sample showed a slight increase as time progresses during the digestion process. This suggests that micelles are forming in time, allowing for the accommodation of cur and, in turn, enhancing its bioavailability. This suggested that the digestion process promoted the formation of micelles, facilitating the incorporation and subsequent absorption of cur, potentially leading to improved absorption and bioavailability.

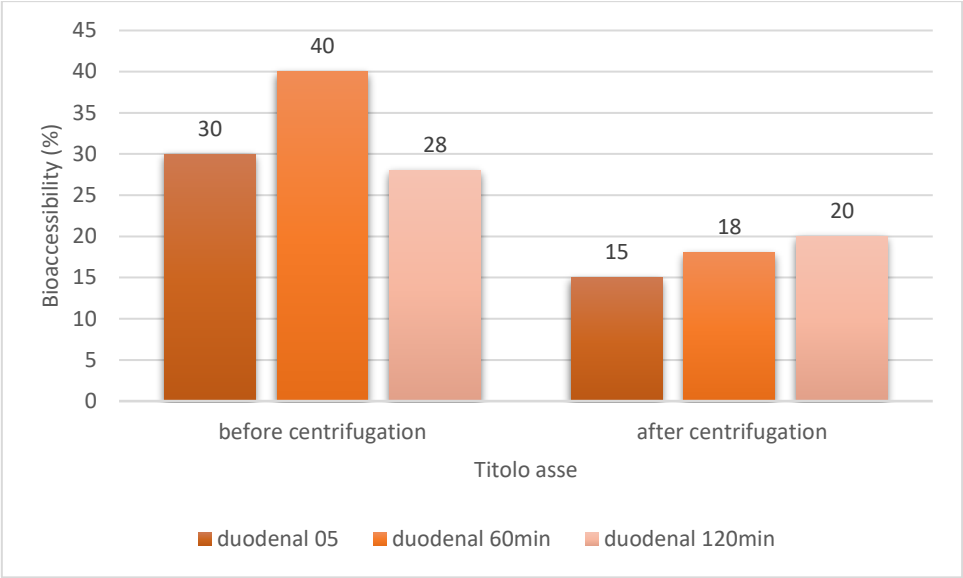


**Figure 6.2.15.** Cur bioaccessibility before and after centrifugation

Based on the quantification of Ct, it was observed that during the initial stages of the duodenal phase, the concentration of Ct remained relatively consistent with that measured in the undigested system. However, as time progresses, the concentration gradually decreased and reached the steady state. This indicated that, initially, the SNEs was not fully degraded, resulting in a difference between the centrifuged and non-centrifuged samples. Subsequently, as the digestion proceeded, the monolayer of the SNEs degrades, leading to the release of free Ct into the solution. This explained the reduction in concentration over time and the eventual equilibrium reached during digestion, where the measured Ct concentration represents the free Ct available in the solution.

**Table 6.2.8.** Ct-FITC quantification in duodenal phase

| | **Concentration before centrifugation [mg/ml]** | **Concentration after centrifugation [mg/ml]** |
|---|---|---|
| **Duodenal 0min** | 0.09 | 0.05 |
| **Duodenal 60min** | 0.07 | 0.07 |
| **Duodenal 120min** | 0.07 | 0.07 |

## 6.2.4. Conclusions and future perspectives

Nutraceuticals exhibit valuable pharmaceutical applications; nevertheless, their low oral bioavailability and unfavorable pharmacokinetic properties necessitate the development of optimized delivery systems. The outcomes obtained in this thesis work have effectively validated the stability of SNEs containing various nutraceuticals such as cur, CoQ10, and lycopene. These SNEs were prepared using well-established protocols

that underwent extensive validation. Furthermore, the study explored the potential application of these protocols to prepare NEs and SNEs at different concentrations of oil and Ct. This approach aimed to streamline preparation processes, reduce costs, and facilitate large-scale applications. Encouraging results were obtained, instilling confidence in the potential scale-up of such delivery systems.

To investigate potential applications in the food sector, the behavior of an SNE enriched with cur during simulated in vitro digestion was examined. The study revealed the stability of these SNEs within the gastric tract, coupled with favorable bioaccessibility values. These findings support the feasibility of utilizing these systems for the effective delivery of nutraceuticals in the context of food-based applications.

Future experiments will involve studying the in vitro digestion of systems with varying concentrations of oil to assess their impact on bioaccessibility. Additionally, there are plans to implement the INFOGEST protocol using a microfluidic device that mimics the intestinal tract. This will provide insights into the behavior of these delivery systems at cellular levels.

These areas of research will be the focal points of further studies in the near future, aimed at enhancing our understanding of these delivery systems and optimizing their efficacy for potential applications in the pharmaceutical and food sectors.

## 6.3 Bibliography


1. Nelson, B. J., Kaliakatsos, I. K. & Abbott, J. J. Microrobots for Minimally Invasive Medicine. *Annu. Rev. Biomed. Eng.* **12**, 55–85 (2010).

2. Huang, T.-Y. *et al.* 3D Printed Microtransporters: Compound Micromachines for Spatiotemporally Controlled Delivery of Therapeutic Agents. *Adv. Mater.* **27**, 6644–6650 (2015).

3. Ahmed, D., Dillinger, C., Hong, A. & Nelson, B. J. Artificial Acousto-Magnetic Soft Microswimmers. *Adv. Mater. Technol.* **2**, 1700050 (2017).

4. Palagi, S., Singh, D. P. & Fischer, P. Light-Controlled Micromotors and Soft Microrobots. *Adv. Opt. Mater.* **7**, 1900370 (2019).

5. Medina-Sánchez, M., Magdanz, V., Guix, M., Fomin, V. M. & Schmidt, O. G. Swimming Microrobots: Soft, Reconfigurable, and Smart. *Adv. Funct. Mater.* **28**, 1707228 (2018).

6. Nocentini, S., Parmeggiani, C., Martella, D. & Wiersma, D. S. Optically Driven Soft Micro Robotics. *Adv. Opt. Mater.* **6**, 1800207 (2018).

7. Mair, L. O. *et al.* Soft Capsule Magnetic Millirobots for Region-Specific Drug Delivery in the Central Nervous System. *Front. Robot. AI* **8**, 702566 (2021).

8. Lee, H., Choi, H., Lee, M. & Park, S. Preliminary study on alginate/NIPAM hydrogel-based soft microrobot for controlled drug delivery using electromagnetic actuation and near-infrared stimulus. *Biomed. Microdevices* **20**, 103 (2018).

9. Power, M., Anastasova, S., Shanel, S. & Yang, G.-Z. Towards hybrid microrobots using pH- and photo-responsive hydrogels for cancer targeting and drug delivery. in *2017 IEEE International Conference on Robotics and Automation (ICRA)* 6002–6007 (IEEE, Singapore, Singapore, 2017). doi:10.1109/ICRA.2017.7989709.

10. Baylis, J. R. *et al.* Self-propelled particles that transport cargo through flowing blood and halt hemorrhage. *Sci. Adv.* **1**, e1500379 (2015).

11. Li, T. *et al.* Self-Propelled Multilayered Microrockets for Pollutants Purification. *ECS J. Solid State Sci. Technol.* **4**, S3016–S3019 (2015).

12. Beckwitt, C. H. *et al.* Liver ‘organ on a chip’. *Exp. Cell Res.* **363**, 15–25 (2018).

13. Zhang, Y. S. *et al.* From cardiac tissue engineering to heart-on-a-chip: beating challenges. *Biomed. Mater.* **10**, 034006 (2015).

14. Mazio, C. *et al.* Easy-to-Build and Reusable Microfluidic Device for the Dynamic Culture of Human Bronchial Cystic Fibrosis Epithelia. *ACS Biomater. Sci. Eng.* **9**, 2780–2792 (2023).

15. Ashammakhi, N., Wesseling-Perry, K., Hasan, A., Elkhammas, E. & Zhang, Y. S. Kidney-on-a-chip: untapped opportunities. *Kidney Int.* **94**, 1073–1086 (2018).

16. Griep, L. M. *et al.* BBB ON CHIP: microfluidic platform to mechanically and biochemically modulate blood-brain barrier function. *Biomed. Microdevices* **15**, 145–150 (2013).

17. Xu, J., Wu, T. & Zhang, Y. Soft Microrobots in Microfluidic Applications. *Biomed. Mater. Devices* **1**, 1028–1034 (2023).

18. Sun, H. C. M., Liao, P., Wei, T., Zhang, L. & Sun, D. Magnetically Powered Biodegradable Microswimmers. *Micromachines* **11**, 404 (2020).

19. Wang, X. *et al.* 3D Printed Enzymatically Biodegradable Soft Helical Microswimmers. *Adv. Funct. Mater.* **28**, 1804107 (2018).

20. Park, J., Kim, J., Pané, S., Nelson, B. J. & Choi, H. Acoustically Mediated Controlled Drug Release and Targeted Therapy with Degradable 3D Porous Magnetic Microrobots. *Adv. Healthc. Mater.* **10**, 2001096 (2021).

21. Louis, F. *et al.* Bioprinted Vascularized Mature Adipose Tissue with Collagen Microfibers for Soft Tissue Regeneration. *Cyborg Bionic Syst.* **2021**, 2021/1412542 (2021).

22. Zhong, D. *et al.* Orally deliverable strategy based on microalgal biomass for intestinal disease treatment. *Sci. Adv.* **7**, eabi9265 (2021).

23. Quashie, D. *et al.* Magnetic bio-hybrid micro actuators. *Nanoscale* **14**, 4364–4379 (2022).

24. Yasa, O., Erkoc, P., Alapan, Y. & Sitti, M. Microalga-Powered Microswimmers toward Active Cargo Delivery. *Adv. Mater.* **30**, 1804130 (2018).

25. Dong, M. *et al.* 3D-Printed Soft Magnetoelectric Microswimmers for Delivery and Differentiation of Neuron-Like Cells. *Adv. Funct. Mater.* **30**, 1910323 (2020).

26. Lee, K. Y. & Mooney, D. J. Alginate: Properties and biomedical applications. *Prog. Polym. Sci.* **37**, 106–126 (2012).

27. Yin, B.-S., Li, M., Liu, B.-M., Wang, S.-Y. & Zhang, W.-G. An integrated microfluidic device for screening the effective concentration of locally applied tacrolimus for peripheral nerve regeneration. *Exp. Ther. Med.* **9**, 154–158 (2015).

28. Di Natale, C. *et al.* Morphological and Rheological Guided Design for the Microencapsulation Process of Lactobacillus paracasei CBA L74 in Calcium Alginate Microspheres. *Front. Bioeng. Biotechnol.* **9**, 660691 (2021).

29. Fujii, T. PDMS-based microfluidic devices for biomedical applications. *Microelectron. Eng.* **61–62**, 907–914 (2002).

30. Liga, A., Morton, J. A. S. & Kersaudy-Kerhoas, M. Safe and cost-effective rapid-prototyping of multilayer PMMA microfluidic devices. *Microfluid. Nanofluidics* **20**, 164 (2016).

31. De Gregorio, V. *et al.* Intestine-on-chip device increases ECM remodeling inducing faster epithelial cell differentiation. *Biotechnol. Bioeng.* **117**, 556–566 (2020).

32. Nasri, H., Baradaran, A., Shirzad, H. & Rafieian-Kopaei, M. New concepts in nutraceuticals as alternative for pharmaceuticals. *Int. J. Prev. Med.* **5**, 1487–1499 (2014).

33. Santini, A. *et al.* Nutraceuticals: opening the debate for a regulatory framework. *Br. J. Clin. Pharmacol.* **84**, 659–672 (2018).

34. Rautiainen, S., Manson, J. E., Lichtenstein, A. H. & Sesso, H. D. Dietary supplements and disease prevention — a global overview. *Nat. Rev. Endocrinol.* **12**, 407–420 (2016).

35. Santini, A., Tenore, G. C. & Novellino, E. Nutraceuticals: A paradigm of proactive medicine. *Eur. J. Pharm. Sci.* **96**, 53–61 (2017).

36. Santini, A. & Novellino, E. Nutraceuticals: Beyond the Diet Before the Drugs. *Curr. Bioact. Compd.* **10**, 1–12 (2014).

37. Frisardi, V. *et al.* Nutraceutical Properties of Mediterranean Diet and Cognitive Decline: Possible Underlying Mechanisms. *J. Alzheimers Dis.* **22**, 715–740 (2010).

38. Ansari, S., Chauhan, B., Kalam, N. & Kumar, G. Current concepts and prospects of herbal nutraceutical: A review. *J. Adv. Pharm. Technol. Res.* **4**, 4 (2013).

39. Davidov-Pardo, G. & McClements, D. J. Resveratrol encapsulation: Designing delivery systems to overcome solubility, stability and bioavailability issues. *Trends Food Sci. Technol.* **38**, 88–103 (2014).

40. McClements, D. J. Nanoscale Nutrient Delivery Systems for Food Applications: Improving Bioactive Dispersibility, Stability, and Bioavailability. *J. Food Sci.* **80**, (2015).

41. Jafari, S. M. & McClements, D. J. Nanotechnology Approaches for Increasing Nutrient Bioavailability. in *Advances in Food and Nutrition Research* vol. 81 1–30 (Elsevier, 2017).

42. Oehlke, K. *et al.* Potential bioavailability enhancement of bioactive compounds using food-grade engineered nanomaterials: a review of the existing evidence. *Food Funct.* **5**, 1341 (2014).

43. Atay, E. *et al.* Development and characterization of chitosan/gelatin electrosprayed microparticles as food grade delivery vehicles for anthocyanin extracts. *Food Hydrocoll.* **77**, 699–710 (2018).

44. Benshitrit, R. C., Levi, C. S., Tal, S. L., Shimoni, E. & Lesmes, U. Development of oral food-grade delivery systems: Current knowledge and future challenges. *Food Funct* **3**, 10–21 (2012).

45. Belhaj, N. *et al.* Formulation, characterization and pharmacokinetic studies of coenzyme Q10 PUFA's nanoemulsions. *Eur. J. Pharm. Sci.* **47**, 305–312 (2012).

46. Lovelyn, C. & Attama, A. A. Current State of Nanoemulsions in Drug Delivery. *J. Biomater. Nanobiotechnology* **02**, 626–639 (2011).

47. Pathak, K., Pattnaik, S. & Swain, K. Application of Nanoemulsions in Drug Delivery. in *Nanoemulsions* 415–433 (Elsevier, 2018). doi:10.1016/B978-0-12-811838-2.00013-8.

48. McClements, D. J. & Li, Y. Structured emulsion-based delivery systems: Controlling the digestion and release of lipophilic food components. *Adv. Colloid Interface Sci.* **159**, 213–228 (2010).

49. Gutiérrez, J. M. *et al.* Nano-emulsions: New applications and optimization of their preparation. *Curr. Opin. Colloid Interface Sci.* **13**, 245–251 (2008).

50. Leong, T. S. H., Wooster, T. J., Kentish, S. E. & Ashokkumar, M. Minimising oil droplet size using ultrasonic emulsification. *Ultrason. Sonochem.* **16**, 721–727 (2009).

51. McClements, D. J. Advances in fabrication of emulsions with enhanced functionality using structural design principles. *Curr. Opin. Colloid Interface Sci.* **17**, 235–245 (2012).

52. Wooster, T. J., Golding, M. & Sanguansri, P. Impact of Oil Type on Nanoemulsion Formation and Ostwald Ripening Stability. *Langmuir* **24**, 12758–12765 (2008).

53. McClements, D. J. Nanoemulsion-based oral delivery systems for lipophilic bioactive components: nutraceuticals and pharmaceuticals. *Ther. Deliv.* **4**, 841–857 (2013).

54. Vecchione, R. *et al.* Tunable stability of monodisperse secondary O/W nano-emulsions. *Nanoscale* **6**, 9300 (2014).

55. Vecchione, R. *et al.* Curcumin bioavailability from oil in water nano-emulsions: In vitro and in vivo study on the dimensional, compositional and interactional dependence. *J. Controlled Release* **233**, 88–100 (2016).

56. Johnston, A. P. R., Cortez, C., Angelatos, A. S. & Caruso, F. Layer-by-layer engineered capsules and their applications. *Curr. Opin. Colloid Interface Sci.* **11**, 203–209 (2006).

57. Ogawa, S., Decker, E. A. & McClements, D. J. Production and Characterization of O/W Emulsions Containing Droplets Stabilized by Lecithin−Chitosan−Pectin Mutilayered Membranes. *J. Agric. Food Chem.* **52**, 3595–3600 (2004).

58. McClements, D. J. Theoretical Analysis of Factors Affecting the Formation and Stability of Multilayered Colloidal Dispersions. *Langmuir* **21**, 9777–9785 (2005).

59. Lehr, C.-M., Bouwstra, J. A., Schacht, E. H. & Junginger, H. E. In vitro evaluation of mucoadhesive properties of chitosan and some other natural polymers. *Int. J. Pharm.* **78**, 43–48 (1992).

60. Dodane, V. & Vilivalam, V. D. Pharmaceutical applications of chitosan. *Pharm. Sci. Technol. Today* **1**, 246–253 (1998).

61. Jayakumar, R., Nwe, N., Tokura, S. & Tamura, H. Sulfated chitin and chitosan as novel biomaterials. *Int. J. Biol. Macromol.* **40**, 175–181 (2007).

62. Bernkop-Schnürch, A. & Dünnhaupt, S. Chitosan-based drug delivery systems. *Eur. J. Pharm. Biopharm.* **81**, 463–469 (2012).

63. Kumar, M. N. V. R., Muzzarelli, R. A. A., Muzzarelli, C., Sashiwa, H. & Domb, A. J. Chitosan Chemistry and Pharmaceutical Perspectives. *Chem. Rev.* **104**, 6017–6084 (2004).

64. Fini, A. & Orienti, I. The Role of Chitosan in Drug Delivery: Current and Potential Applications. *Am. J. Drug Deliv.* **1**, 43–59 (2003).

65. Brodkorb, A. *et al.* INFOGEST static in vitro simulation of gastrointestinal food digestion. *Nat. Protoc.* **14**, 991–1014 (2019).

66. Qian, C., Decker, E. A., Xiao, H. & McClements, D. J. Nanoemulsion delivery systems: Influence of carrier oil on β-carotene bioaccessibility. *Food Chem.* **135**, 1440–1447 (2012).

67. Salvia-Trujillo, L., Qian, C., Martín-Belloso, O. & McClements, D. J. Modulating β-carotene bioaccessibility by controlling oil composition and concentration in edible nanoemulsions. *Food Chem.* **139**, 878–884 (2013).